Electrical characterization and identification of deep levels in β-Ga_2O_3

Mads Eide Ingebrigtsen

Universitetet i Oslo
Mai 2019

© Mads Eide Ingebrigtsen, 2019

Series of dissertations submitted to the
Faculty of Mathematics and Natural Sciences, University of Oslo
No. 2119

ISSN 1501-7710

All rights reserved. No part of this publication may be
reproduced or transmitted, in any form or by any means, without permission.

Cover: Hanne Baadsgaard Utigard.
Print production: Reprosentralen, University of Oslo.

Abstract

This thesis brings together fundamental studies presented in five papers with the focus on the investigation of defects in the wide bandgap semiconductor β-Ga_2O_3. A broad range of methods was applied; in particular the characterization of electrically active defects was done using capacitance spectroscopic techniques along with chemical characterization, x-ray absorption, and theoretical modelling.

In Paper I we compare different metals for use as Schottky contacts on (010) and (2;¯01) oriented samples, and measure a new E4 deep level in bulk material for the first time. In Paper II we present strong arguments for attributing the dominating E2 level to Fe impurities. This assignment was reasoned by systematic correlations across a set of several samples, theoretical modelling of Fe on Ga sites, and irradiation experiments excluding the intrinsic origin of E2. Concurrently, we discovered a new level labeled E2* in close proximity to E2 and attributed its origin to intrinsic defects in β-Ga_2O_3. The irradiation studies were continued in Paper III, providing a systematic picture of the irradiation induced charge carrier removal and deep level generation in β-Ga_2O_3. In particular, we describe the kinetics of charge carrier recovery during annealing, based on a combination of experimental and theoretical work. We suggest that the origin of the carrier removal is in pinning of the Fermi level from the V_{Ga} acceptors as well as Ga_i and Ga_O donors. In its turn the carrier recovery is mediated by complex formation and passivation via H- or V_O-related defects. A discussion on the generation of the deep levels E2* and E4* is also given, with the focus on their concentrations being influenced by high temperature treatments. Similar temperature effects were also observed in epitaxial material, where generation of three new deep levels, E3*, E5, and E6, occurred under reverse bias conditions and heating up to 625 K, as described in Paper IV. In Paper V we made an attempt to record the electrical and structural signatures of the defects in β-Ga_2O_3 simultaneously detecting capacitance and fluorescence signals upon the x-ray absorption. Altogether, this thesis may be seen as a step forward better understanding of defects in β-Ga_2O_3, which is currently a hot topic in semiconductor physics.

Acknowledgements

There are a lot of people who contributed to the realization of the research work of this thesis. I would like to thank my main supervisor, Prof. Andrej Kuznetsov, for giving me the opportunity to take on this doctoral study and for contributing his experience throughout this work. I want to thank also Dr. Vishnukanthan Venkatachalapathy who, as co-supervisor was an invaluable partner in the preparation for and realization of the x-ray absorption measurements in Grenoble. Completion of this work would also not be possible without Prof. Lasse Vines on the team as co-supervisor. He initiated the work on gallium oxide, supervised it with an admirable passion for details of the subject and for developing his students to become good scientists. Further, I also owe Prof. Bengt Svensson, who unfortunately left us under very sad circumstances last summer, my acknowledgements for always caring for and contributing valuable insight to the research.

I would like to thank Joel Varley at the Lawrence Livermore National Laboratory (USA) for excellent simulations and co-authorship in papers II and III, Giovanni Alfieri and Andrei Mihaila at ABB (Switzerland) for fruitful collaboration on gallium oxide, and Herman Emerich for supervision through some memorable weeks at the Swiss-Norwegian Beam Line (France). In the home lab of MiNa I am grateful to Viktor, Micke, Halvor and Christoph’s tireless efforts to keep the lab running. And a special thank you to Viktor is in order for always smiling through overtime hours at the implanter.

To all my colleagues and friends at LENS and MiNaLab I am deeply thankful for providing such a great community both for professional development and social activities. To Heine, Nishant, Sigbjørn, and Vegard for more than a few table tennis breaks. To Bjørn, Edvard and Marianne for sharing some kilometers of paths in the forest. And to all of you for great cabin trips and Friday beers.

A special thanks to my family for their endless support and cheering me on. And last but not least, a solid thanks to my wife, Selene, for all the love, hearing out my frustrations, and her astonishing ability to keep me sane (enough) to finish this. I love you!

Thank you!

Contents

Chapter 1 Introduction 1

Chapter 2 Physics of Semiconductors 5

- 2.1 Structural and electronic properties 5
- 2.2 Deviations from an ideal structure 7
  - 2.2.1 Doping 8
  - 2.2.2 Electrically active defects 9
- 2.3 Schottky barrier diodes 10

Chapter 3 Methodology 13

- 3.1 Current- and Capacitance-Voltage 13
- 3.2 Deep Level Transient Spectroscopy 14
  - 3.2.1 From capacitance transient to spectra 15
  - 3.2.2 From spectra to electrical characteristics 16
  - 3.2.3 Field dependence and Poole-Frenkel effect 17
  - 3.2.4 Depth profiles of deep levels 17
- 3.3 Thermal Admittance Spectroscopy 18
- 3.4 Secondary Ion Mass Spectrometry 19
- 3.5 Altering the concentrations of intrinsic defects 20
  - 3.5.1 Annealing 20
  - 3.5.2 Ion implantation and irradiation 21
- 3.6 X-ray Absorption Spectroscopy and Fine Structure 22
- 3.7 Combining x-rays and capacitance 24

Chapter 4 Defects in Gallium Oxide 29

- 4.1 Introduction to Gallium Oxide 29
  - 4.1.1 Fundamental properties of β-Ga_2O_3 29
  - 4.1.2 Prospects for applications 31
  - 4.1.3 Synthesis 34

4.2 Shallow electronic states 35
4.2.1 Donor doping 35
4.2.2 Acceptor doping 37
4.3 Deep levels 38
4.3.1 Predictions for intrinsic defects 39
4.4 Irradiation damage 40
Chapter 5 Summary of results 43
5.1 Iron in β-Ga_2O_3 43
5.2 Donors in bulk and epitaxial material 45
5.3 Irradiation-induced charge carrier removal 46
5.4 Irradiation-induced deep levels 49
5.5 Meta-stability of deep levels in β-Ga_2O_3 50
5.6 Development of capacitance x-ray recording 52
5.7 CXAFS of epitaxial β-Ga_2O_3 54
Chapter 6 Conclusions and future work 57
Bibliography 61
Chapter 7 Appendices 69
7.1 Details of the CXAFS recording setup 69
7.2 Cryostats and sample holders for CXAFS 70
7.2.1 Version 1: Nitrogen cryostream 70
7.2.2 Version 2: Helium vacuum system 71
Papers 73
Paper I 75
Paper II 81
Paper III 89
Paper IV 101
Paper V 111

Chapter 1

Introduction

The study of defects in semiconductor material science is often concerned about zero dimensional defects, also known as point defects. In material science in general the dimensionality of defects refers to their physical extent, and a zero-dimensional defect extends no more than a couple of atomic sites in a material. As such it may be an impurity atom or intrinsic defect, or some cluster of a few of these. The limited size implies that the zero-dimensional defects contribute quantized discrete energy levels, and in a semiconductor, these may well be positioned within the bandgap that otherwise contains no allowed electron states. Indeed, the addition of impurity elements with electron levels close to the band edges is the foundation for controlled n- and p-type conductivity that all semiconductor technologies rely on. On the other hand, unwanted impurities from material synthesis or other sources may prove detrimental to device performance. In any case, the understanding of electronic energy levels and identification of their structural origin is among the most fundamental challenges of semiconductor material science.

The reason why we can often successfully limit our study to the zero-dimensional defects is that well-controlled synthesis methods allow production of close to ideal materials. For instance, silicon, the main staple of all modern information technology, is the purest material known, whether natural or synthesized. However, a challenge with these high purity materials is that the remaining low concentrations of point defects can be difficult to detect, while their influence on functional properties can still be considerable.

At present, the way of learning about point defects and their associated electronic properties is through a combination of experimental methodologies. Specifically, different measurements need to be done to observe electronic properties and the structural defects that cause these. For the electronic properties we rely largely on the capacitance-based methods, like capacitance-voltage, thermal admittance spectroscopy and not least deep level transient spectroscopy. But in order to know where the electronic states come from, correlations with other measurements or sample treatments are necessary. Secondary ion mass spectrometry is the go-to method for determining the content of impurity atoms in a sample, whereas the intrinsic defects must be correlated with provocations that cause generation, like irradiation or heat treatments, before we are able to discern their electron levels.

At the outset of this doctoral project one main objective was to investigate the prospects of a combination of methods to reveal simultaneous information about electronic and structural properties. Based on a few literature entries presenting ideas of combining capacitance-based measurements with high energy x-ray stimulation, our studies at the European Synchrotron Radiation Facility was aiming to verify and potentially develop these methods. If successful the new methodology could hold promise to greatly reduce the effort needed for characterization and identification of deep levels in semiconducting materials. Whereas we have been able to record x-ray absorption with capacitance signal, the conclusion of this signal's origin to be selectively reporting on defect related electron levels must be questioned. Herein, follows a discussion of our findings and the theoretical foundation for the interaction between electrical characteristics of semiconducting samples and x-ray stimulation.

In this thesis, work on the novel oxide semiconductor gallium oxide is presented. Gallium oxide was used both as a sample for the capacitance x-ray absorption experiments and as a research object on its own, using the traditional pathways for investigation. Over the last decade, gallium oxide has attracted increasing attention due to realization of high-quality material in bulk and epitaxial films. The appealing properties of gallium oxide include a very large bandgap, large breakdown field, and controllable n-type charge carrier concentration. The first of these, the large bandgap, means that the material is transparent to all visible light, and actually the whole solar spectrum. As such, gallium oxide is promising for solar-blind detectors of ultraviolet irradiation. Also, devices for ultraviolet emission can be envisioned. The second property, the large breakdown voltage, is especially interesting for devices in power electronics, where the ability of transistors to handle high power densities is sought after. To realize these devices, the control of charge carriers is of key importance. While p-type conductivity is not available at present, n-type conductivity can with relative ease be controlled in a large range, using donor dopants and compensating deep acceptors. This allows unipolar devices like Schottky diodes and different variations of field effect transistors, and well-behaved devices have already been presented in the literature. To bring gallium oxide devices towards their theoretically unparalleled performance numbers, improved understanding of defects and their electrical behavior is called for. In a recent review, Pearton et al. [1] lists what they consider the most important topics for future research, including; (i) “Identification of the dominant defects in bulk crystals and epitaxial films and the effect on device performance”, and (ii) “Better understanding of carrier removal rates, dominant defects created, and transient dose effects resulting from radiation damage […].”. This is in excellent agreement with our group’s understanding, and what the work presented here aims to contribute to.

Paper I presents our introductory work on gallium oxide, where sample preparation steps are outlined, importantly finding that nickel proves to be a good material for Schottky contacts for our characterization purposes. We further describe a new deep level in the bandgap of bulk material. In paper II, we look closer at several samples, also epitaxial films, and conclude that the common E2 deep level is related to iron impurities. Strengthening this conclusion are density functional calculations that are also presented in this paper. Paper III considers the influence of proton irradiation, and discusses potential candidates for intrinsic defect clusters that may cause compensation of charge carriers and generation of deep levels. Following, paper IV considers some peculiar deep level generation properties observed in epitaxial material caused by the electric field and high temperature imposed by the measurement conditions. And finally, in paper V, a summary of the results of the combined capacitance and x-ray absorption measurements on gallium oxide are presented.

Chapter 2

Physics of Semiconductors

To serve as background for the presentation of methods and results, this chapter will provide a concise review of the relevant topics of semiconductor physics. This will include considerations of electronic band structures, charge carriers and defects, and lead to an introduction to Schottky diode devices.

2.1 Structural and electronic properties

In an isolated atom, only certain discrete energy levels are allowed for the electrons. When atoms come together in large numbers these discrete energy levels split into energy bands that can be approximated as continuous due to the high density. This happens because the fermionic nature of electrons does not allow them to occupy the same quantum state. A quantum state includes quantum numbers that carry information on spin, energy, and momentum; where the two latter quantum numbers describes what we call an orbital. Forming a crystalline solid, both the composition and the periodic structure of the material influence the relationship between momentum and allowed energy levels, and produce complex band diagrams. Also depending on composition and structure, electrons fill up the bands differently in different materials. Metals are characterized by having partially filled bands where electrons can easily gain an infinitesimal energy and contribute to electrical conductivity. If, on the other hand, one band is filled and the next available electron level is separated by the bandgap, the material will be either a semiconductor or an insulator depending on the magnitude of the bandgap.

The band diagram for gallium oxide is presented in Figure 1, from theoretical calculations by Varley et al. [2]. Here the available energy levels are drawn as a function of reciprocal lattice vectors ($\boldsymbol{k}$) corresponding to different directions in the material. Although the continuous bands form, there will still be energy regions where electrons are not allowed; these are known as bandgaps, and the region between the

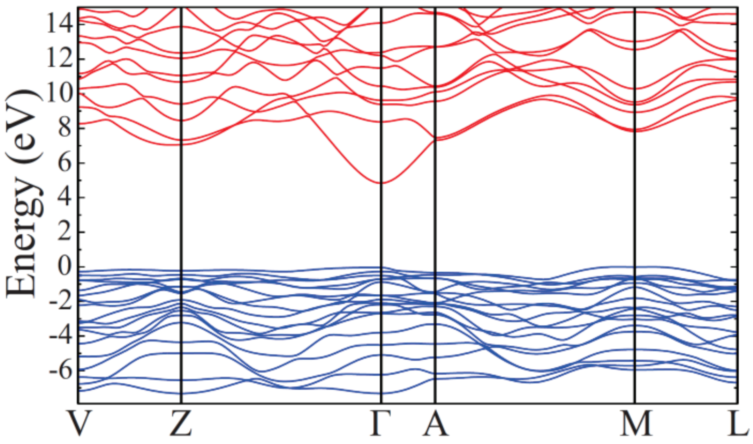

Figure 1 – Band structure of gallium oxide, more exactly β-Ga_2O_3, as calculated by Varley et al. Reprinted from [2], with the permission of AIP Publishing. The blue bands make up the filled valence band, while the red ones are empty conduction band states. The open area between the blue and red is the bandgap.

blue valence band and the red conduction band in Figure 1 provides an example. For many purposes, including also most of the discussion of this thesis, it is sufficient to simplify the information of Figure 1 to a single value for the bandgap. That is, the magnitude of the bandgap is given by $E_g = E_C - E_V$, where E_V denotes the maximum of the occupied valence band, and E_C is the minimum of the unoccupied conduction band. In the ground state, at zero temperature, there will be no electrical conduction in a semiconductor or insulator since there are no easily available electron states for the electrons in the valence band. However, when the temperature rises, thermal energy gives a non-zero probability to find electrons excited to the conduction band. These conduction electrons are free to move in the continuum of states that is available there, and the unoccupied electron state left behind in the valence band can be imagined as a mobile positively charged hole, giving n-type and p-type conductivity, respectively. In an ideal intrinsic semiconductor, the thermal excitation gives an equal concentration of electrons in the conduction band (n) and holes in the valence band (p), where a steady state concentration depends on the magnitude of the bandgap as $n = p \propto \exp -E_g/2kT$.

Whereas the simplified idea of a single value for the bandgap is convenient in many cases, we do need to keep the complex form of Figure 1 in mind for some details. Firstly, when considering the movement of electrons and holes in semiconductors in response to external forces. Conduction electrons and holes in the material are quasi-particles where it is customary to take all influences of the lattice structure and collect into a term known as effective mass, m^*. With this modification to the actual rest mass of the electrons, the quasi-particles can be treated as free electrons in calculations. The effective mass relates to the band structure through an inverse dependence to the curvature of the bands. For instance, the strongly curved conduction band minima at the Γ-point in Figure 1 implies a much lower effective mass for conduction electrons, than for holes in the almost flat valence band. Secondly, we need to note the distinction of direct and indirect bandgaps; for a direct bandgap semiconductor E_V and E_C occur at the same $\boldsymbol{k}$, whereas for indirect there is a separation that among other things influence the mechanism needed for excitation across the gap. In gallium oxide the bandgap is indirect, but with only a very small energy difference to the direct transition it may be considered direct for most practical purposes.

2.2 Deviations from an ideal structure

The usability of semiconductors does not stop at the behavior of the ideal electronic structure from an uninterrupted physical crystal structure. The properties in practical use depend largely on deviations from this structure, whether intended or not. Doping is the process of intentional introduction of impurity atoms, to alter the properties of electrical conduction. On the other hand, impurity atoms or intrinsic defects can also be unwanted consequences of material synthesis or device fabrication, and lead to electronic states that are unfavorable. Some examples of point defects in a monoatomic lattice are shown in Figure 2. Here, vacancies and self-interstitials are examples of intrinsic defects, while substitutional or interstitials of impurity elements are known as extrinsic defects. In diatomic lattices like gallium oxide it is also possible to find so-called antisites, which is for instance a gallium atom

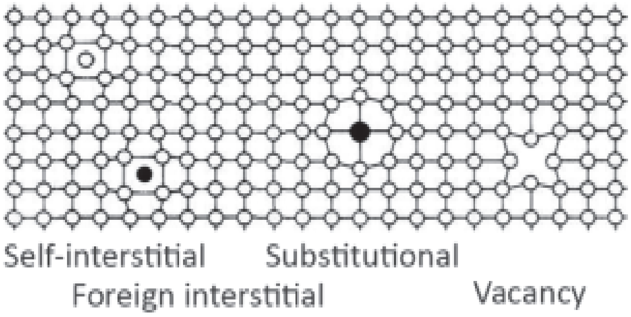

Figure 2 – Some examples of intrinsic and extrinsic defects in a monatomic lattice are shown. In more complex structures, like gallium oxide's monoclinic polymorph, β-Ga_2O_3, more variation is possible by having these defects on all available lattice sites.

on an oxygen site. When studying doping and defects, we are interested in knowing their electrical properties, and tying these to structural properties like physical origin, concentration, and distribution in the material. In the following subsections we look at some electrical properties, as a foundation for the discussion of the experimental methods. This section is based on the textbook by Blood & Orton [3].

2.2.1 Doping

Doping can be done with substitutional elements of either higher valence than the host atom, to donate electrons to the conduction band, or lower valence, to accept electrons from the valence band. Doing so, the electron chemical potential, known as the Fermi level (E_F), is shifted towards the conduction- or valence band, and the material towards having predominantly n-type or p-type conductivity, respectively. Knowing the Fermi level, it is possible to calculate the probability of an electron energy state (E) being occupied at a certain thermal energy (kT), where k is the Boltzmann constant and T is the absolute temperature:

$$f(E) = \frac{1}{1 + e^{\frac{E - E_F}{kT}}} . \tag{2.1}$$

By combining this Fermi distribution with the density of available states ($N(E)$), and integrating over the energies in the conduction band, the concentration of conduction electrons can be determined through:

$$n = \int_{E_C}^{\infty} N(E) f(E) dE . \tag{2.2}$$

A simplification for this expression can be made if; (i) n is small enough to only occupy the lowest part of the conduction band where $N(E)$ can be considered constant, and (ii) the conduction band edge E_C is more than a few kT from the Fermi level E_F so the Fermi distribution simplifies to a Maxwell-Boltzmann distribution:

$$n = N_C f(E_C) = N_C e^{-\frac{E_C - E_F}{kT}} . \tag{2.3}$$

Here the density of states at the conduction band edge is given by;

$$N_C = 2\left(\frac{2\pi m_n^* \, kT}{h^2}\right)^{\frac{3}{2}} , \tag{2.4}$$

assuming only one conduction band minimum, and taking m_n^* as the electron effective mass and h as the Planck constant. Similar calculations can be made for holes in the valence band.

For practical use of doping, a dopant with a shallow donor or acceptor level, i.e. with little energy separation from the respective band edge, is sought after. This yields efficient doping where, at ambient temperatures, the charge carrier concentration approximately equals the dopant concentration (N_D), and there is little temperature dependence.

2.2.2 Electrically active defects

Defects that introduce electronic states further from the band edges than typical dopant levels of about 0.05 eV are labeled deep levels. These are often more problematic for utilization of the materials as they can act as traps or recombination centers. A trap is a defect that takes and holds a charge carrier and thus reduces the doping concentration. Recombination centers have the ability to capture both electrons and holes, and as such assist recombination and by that limit the lifetime of charge carriers. Hence, the interaction between the deep level and the bands are important, and can be described by capture and emission processes. The capture rate of electrons per unoccupied state can be expressed as;

$$c_n = \sigma_n \langle v_n \rangle n \,, \tag{2.5}$$

where σ_n is the capture cross section for electrons on a deep level, and the product of average thermal velocity and electron concentration $\langle v_n \rangle n$ is the flux of electrons. This process competes with emission of electrons (e_n), and similar interaction with holes in the valence band ($c_p$and e_p). Since these are all the possible interactions, the change in occupancy of a deep level can be described as;

$$\frac{dn_t}{dt} = \left(c_n + e_p\right)(N_t - n_t) - \left(c_p + e_n\right)n_t \,, \tag{2.6}$$

where N_t is the total trap concentration and n_t is the concentration of occupied traps. At equilibrium there is no net change in the occupancy, and since a detailed balance must hold, meaning that there can be no transport of charge carriers from one band to the other, we have the two equations;

$$e_n n_t = c_n(N_t - n_t) \qquad\qquad e_p\,(N_t - n_t) = c_p n_t \,. \tag{2.7}$$

These enable making expressions for the relative deep level occupancy;

$$\frac{\hat{n}_t}{N_t} = \frac{c_n}{c_n + e_n} = \frac{e_p}{e_p + c_p} \,, \tag{2.8}$$

and by seeing that this can also be expressed by the Fermi distribution of Eq. (2.1) we can express the emission rate of electrons as a function of capture rate:

$$e_n = c_n\, e^{\frac{E_t - E_F}{kT}} . \quad \textbf{(2.9)}$$

The Fermi level dependence of the ratio of emission and capture processes comes from the dependence on charge carrier concentration from equation (2.3). To a first approximation levels below the Fermi level will be filled, while levels above the Fermi level emit more quickly than they fill, and tend to be unoccupied. Inserting the capture rate and n we get:

$$e_n = \sigma_n \langle v_n \rangle N_C e^{-\frac{E_C - E_t}{kT}} . \quad \textbf{(2.10)}$$

Here the Fermi level has been eliminated and the expression instead gives the energy with reference to E_C. The deep level position relative to E_C together with the capture cross section is called the trap signature, and can be anticipated from experimental procedures like deep level transient spectroscopy, to be described in section 3.2. For this purpose it is important to realize that the emission rate is temperature dependent, both in the exponential and through the thermal velocity and the conduction band density of states. Inserting for $\langle v_n \rangle = \sqrt{3kT/(m_n^*)}$ and N_C from equation (2.4) we get:

$$e_n(T) = \sigma_n \beta T^2 \exp\left(-\frac{E_C - E_t}{kT}\right), \quad \textbf{(2.11)}$$

where all the material properties are collected in the constant $\beta = 2\sqrt{3}\,(2\pi)^{\frac{3}{2}} k^2 m^* h^{-3}$, and the temperature dependence is more easily distinguished. Regarding measurements of the emission rate, the reaction of taking an electron from the trap level to the conduction band is actually a change in Gibbs free energy. Realizing this, we can pull out the temperature independent entropy term from the exponential, so that;

$$e_n(T) = e^{\frac{\Delta S}{k}} \sigma_n \beta T^2 e^{-\frac{\Delta H}{kT}} . \quad \textbf{(2.12)}$$

From this, it will be clear that what we observe experimentally is the apparent capture cross section $\sigma_{na} = e^{\Delta S/kT} \sigma_n$ and the enthalpy of the excitation process.

2.3 Schottky barrier diodes

The Schottky barrier diode (SBD) is a two-terminal rectifying device, fundamental to semiconductor technology. Contrary to pn-junctions where p-type and n-type semiconductor regions make up a rectifying junction, SBD's are unipolar, with only one type of semiconductor and a metallic contact.

Consider an n-type semiconductor with electron affinity $\chi_s = E_{vac} - E_C$ and a metal of work function $\phi_m = E_{vac} - E_F^m$, as illustrated in Figure 3 (a). If the materials are brought to contact and the metal work function is greater than the semiconductor electron affinity, electrons can move to lower energy states by going into the metal. In equilibrium, the Fermi levels align between the materials, the bands bend into the semiconductor, and an energy barrier $\phi_b = \phi_m - \chi_s$ occurs at the interface, as is illustrated in Figure 3 (b).

Poisson's equation relates a gradient in an electric field ($\mathcal{E}$) to the charge density at a point x:

$$\frac{d\mathcal{E}(x)}{dx} = \frac{q}{\epsilon}(p - n + N_d^+ - N_a^-)\,, \tag{2.13}$$

Where q is the elementary charge, ϵ the permittivity, and N_d^+ and N_a^- is the ionized donor and acceptor concentrations, respectively. In the n-type semiconductor in our example, there are no holes or acceptors. The diffusion of electrons into the metal leaves positive donor ions alone in a region close to the interface known as the depletion region or space charge region. Hence, an electric field is set up across the junction, counteracting the drift of charge carriers into the metal. This can be expressed;

$$\frac{d\mathcal{E}(x)}{dx} = \frac{qN_d^+}{\epsilon}\,, \tag{2.14}$$

where the electric field can also be expressed as a voltage by $\mathcal{E}(x) = dV_{bi}/dx$. V_{bi} is known as the built-in voltage, designating the potential difference between the

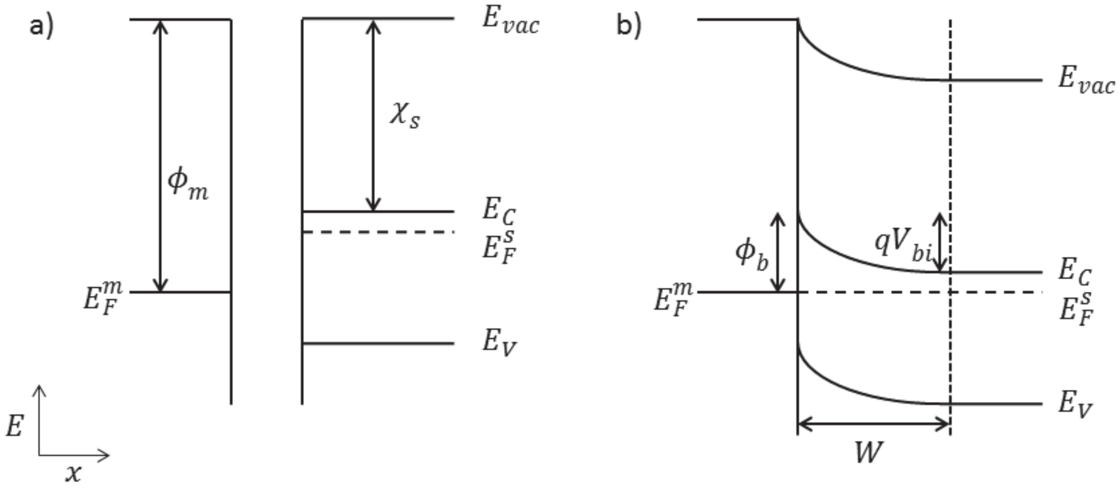

Figure 3 – Energy band diagram before and after bringing together a metal and a semiconductor to a Schottky barrier diode.

semiconductor outside the depletion region and the metal. Integrating to find this voltage, we can solve for the depth of the depletion region W;

$$W = \left(\frac{2\varepsilon}{q}\left(\frac{1}{N_d}\right)V\right)^{\frac{1}{2}}. \quad \textbf{(2.15)}$$

Here V can be equal to the built-in voltage, or if an external bias voltage is applied, $V = V_{bi} - V_{applied}$. The applied voltage on the SBD imposes a difference between the Fermi levels in the semiconductor and metal. Forward bias decreases the built-in voltage and electrons can flow through the junction. Conversely, a reverse bias increases the voltage and thereby the electric field and the depletion depth. Electrons face the barrier ϕ_b under reverse bias, effectively blocking conduction, and this unidirectional conductivity is what is known as rectification.

It can be shown that the depletion region can be described as a parallel plate capacitor with the area A of the metallic contact and plate separation equal to the depletion depth.

$$C = \frac{\epsilon A}{W}. \quad \textbf{(2.16)}$$

Chapter 3

Methodology

As mentioned in the introduction, methodology in this thesis serves both as the tool-kit for the gallium oxide studies, and a research topic on its own through the attempt to combine x-ray absorption spectroscopy with capacitance measurements. In this chapter, the relevant methods for conventional characterization will first be introduced. Then, in section 3.7 follows a review of the idea and literature of capacitance-based x-ray stimulated spectroscopy techniques.

3.1 Current- and Capacitance-Voltage

Rectifying contacts, as provided by Schottky barriers described in section 2.3, is a requirement for the capacitance spectroscopies introduced in the following sections. Initial evaluation of the Schottky contacts has been routinely done throughout this work by current-voltage (IV) and capacitance-voltage (CV) measurements. These techniques have also been used for studies of the performance of different metals as Schottky contacts on gallium oxide.

The current through a rectifying contact can be described by the diode equation,

$$I = I_0\left(\exp\left(-\frac{q\left(V_{eff}\right)}{\eta kT}\right) - 1\right) \tag{3.1}$$

where V_{eff} is the effective voltage, in other words, the applied voltage minus resistive loss $V_{eff} = V_{applied} - IR_S$. Further, η is the ideality factor of the diode, which is equal to one for ideal diodes and deviate to larger values if generation or recombination is substantial in the depletion region. The pre-factor I_0 is the reverse saturation current,

$$I_0 = A^* A T^2 \exp\left(-\frac{\phi_b}{kT}\right) \tag{3.2}$$

with A^* being the material specific Richardson constant that depends on the effective mass (m^*) through $A^* = 4\pi m^* k^2 q/h^3$. The primary quality measures of the diode is the barrier height and ideality factor, which can be derived from the low forward bias region of IV measurements, where resistive loss is not yet prominent. Further, the degree of rectification is an important figure that depends on the series resistance (R_S) under high forward bias conditions and the reverse saturation current under reverse bias.

Describing the capacitance of a Schottky contact as a parallel plate capacitor as in equation (2.16) and inserting for the depletion width in equation (2.15), we get:

$$C = \frac{\epsilon A}{W} = A\sqrt{\frac{\epsilon q}{2V} N_d} \quad \textbf{(3.3)}$$

Commonly, CV measurement data is plotted as $1/C^2$ as a function of V, giving a linear relationship that allows identification of the charge carrier concentration in the semiconductor and the built-in voltage. The built-in voltage can in turn be used to determine the barrier height from the Schottky-Mott rule, and comparison can be made to the IV-derived barrier height. The CV data can also be used to calculate the donor concentration as function of depth, which was used extensively in paper III, studying the recovery of donor dopants after irradiation.

3.2 Deep Level Transient Spectroscopy

Deep level transient spectroscopy (DLTS) is a powerful characterization tool to determine the electronic properties and concentrations of deep level traps. Specifically, DLTS enables determination of the trap signature by isolating the emission of majority carriers. It is the depletion region of a rectifying diode that is used to isolate the emission process, where minority carrier band interactions are considered negligible, and the majority carrier capture is not happening due to the depletion of free carriers.

In DLTS – as proposed by Lang in 1974 [4] and thoroughly described by Blood and Orton [3] – the exponential recovery of depletion capacitance is observed in a reverse biased diode after pulsing the bias to fill the deep levels. This is possible because the deep levels also contribute to the capacitance, but responds to changes in the biasing slower than the charge carriers from doping. From a steady reverse bias, giving a large depletion region, the filling pulse shrinks the depletion region for a sufficiently long time for the traps to capture charge carriers. When the filling pulse is over and the reverse bias re-established, the capacitance from the shallow donors responds on a very short time scale. Meanwhile, the emission from the deep levels respond over a longer time, and it can be shown that this yields a capacitance change with an exponential time-dependence on the emission rate:

$$\frac{\Delta C(t)}{C} = \frac{N_t}{2N_d} e^{-e_n(T)t} \,. \tag{3.4}$$

Here $\Delta C(t)$ is the change in capacitance from the deep level, as function of time (t), and $C(\infty)$ is the steady state capacitance from both donors and deep levels given by:

$$C = A\sqrt{\frac{\epsilon q(N_d + N_t)}{2V}} \,. \tag{3.5}$$

This is the same expression as in equation (3.3), while also accounting for the concentration of a single donor-like trap. Other traps would again alter the expression accordingly. A schematic of the biasing conditions in DLTS is shown in Figure 4 (a), and the resulting exponential capacitance recovery in Figure 4 (b).

3.2.1 From capacitance transient to spectra

To interpret recorded capacitance transients, a DLTS signal is created by evaluating the emission rate against a rate-window using a weighting function. For illustration, a simplistic box-car weighting function is shown in Figure 4 (c), where a peak is produced when the emission rate is so that a maximal capacitance change occurs within the window between time t_1 and t_2. To be able to discern different deep levels, several rate windows are used, typically six or eight in this work. The signal for the i-th window as function of temperature can be formalized as:

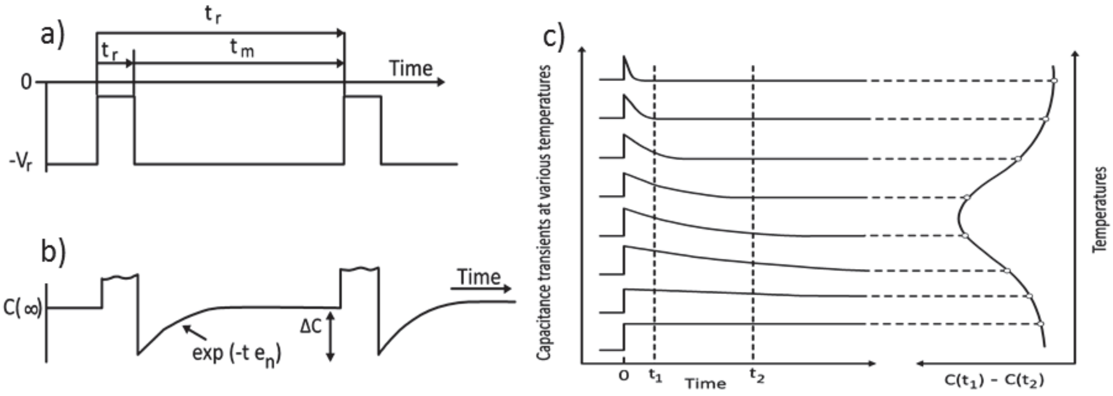

Figure 4 – The biasing during DLTS includes pulsing to remove the depletion region and thus fill the deep levels (a). This gives an exponential capacitance transient response depending on the emission rate (b). Analysis of transients as function of temperature gives a temperature-dependent signal.

$$S_i(T) = \frac{1}{n_i} \sum_{t_j=t_d}^{t_d+t_i} \Delta C(T, t_j) \omega(t_j). \tag{3.6}$$

Here n_i and t_i represent the number of measurements in the rate window and the duration of it, respectively. The delay time t_d is the time between the end of the filling pulse and start of the measurement, added to avoid problems with the measurement setup where the capacitance meter may saturate during the filling pulse. A more sophisticated weighting function ($\omega(t)$) than the box-car is necessary to achieve good signal; high signal to noise ratio is best achieved with a lock-in weighting function, whereas better separation of closely spaced peaks can be reached using a GS4 weighting function. Further details of the weighting functions are well described in Ref. [5].

3.2.2 From spectra to electrical characteristics

Having recorded the DLTS signal in agreement with equation (3.6) we can see that the temperature derivative must be zero at the peaks:

$$\frac{dS(T)}{dT} = \frac{dS}{d(e_n t_i)} \frac{d(e_n t_i)}{dT} = 0\,. \tag{3.7}$$

Here, the variable change allows us to evaluate only the first factor, as the second is zero only for zero temperature. Hence, the zero point must originate from a specific $e_n t_i$ combination, and indeed this can be found by numerically solving equation (3.6) for a given rate window and weighting function. From this, we now have sets of both the temperature of the peak and the associated value for the emission rate for each window. Looking back at equation (2.12), which can be rearranged to:

$$\ln \frac{e_n}{T^2} = \ln \sigma_{na} \beta - \frac{\Delta H}{kT}, \tag{3.8}$$

we can make an Arrhenius plot to extract the enthalpy and apparent capture cross section discussed in section 2.2.2. In addition to this, the concentration can be evaluated at the peak temperatures by combining equations (3.4) and (3.6), and solving for N_t:

$$N_t = 2N_d \frac{\Delta C}{C}\,. \tag{3.9}$$

3.2.3 Field dependence and Poole-Frenkel effect

For some deep levels, the energy positions observed from DLTS may vary, depending on the biasing conditions. The Poole-Frenkel effect describes barrier lowering, and thus enhanced emission caused by an electric field [3, 6], as illustrated in Figure 5. A trap with a coulombic potential will cause this effect, and thus neutral traps cannot cause it. Hence, it can be used to identify donor-like traps in n-type material and acceptor-like traps in p-type. The magnitude of the barrier lowering can be expressed as [3]:

$$\Delta E_t = \left(\frac{q^3 \mathcal{E}}{4\epsilon}\right)^{\frac{1}{2}}. \tag{3.10}$$

3.2.4 Depth profiles of deep levels

For a more accurate determination of the concentration of deep levels one must account for the λ-region of the depletion region and the possibility of non-uniform distribution. The λ-region is the volume at the far end of the depletion region where the deep level is below the Fermi level despite the reverse bias. In this volume the deep level does not emit charge carriers, and thus does not contribute to the capacitance despite being inside the depletion region. The extent of this transition zone is defined as $\lambda = \sqrt{\epsilon\,(E_F - E_t)/qN_d}$ [3].

Depth profiling of a deep level can be done by choosing a rate window and measuring DLTS while holding the temperature constant at the peak temperature. By keeping the reverse bias constant and increasing the pulsing bias to come gradually closer to the interface of the diode, the concentration versus depth can be determined.

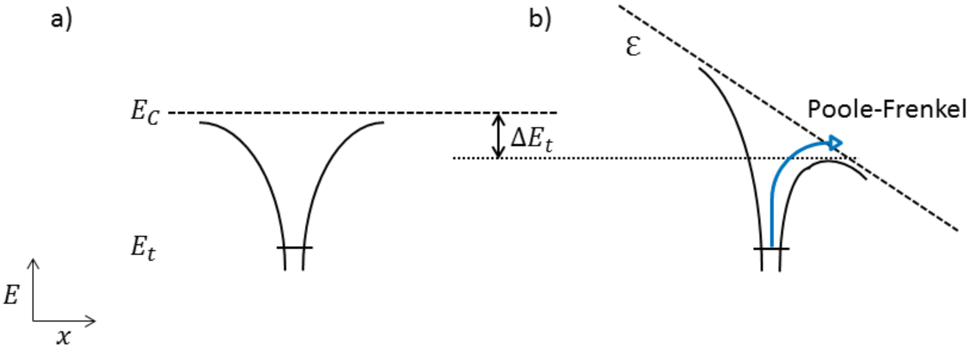

Figure 5 – The potential barrier of a deep level is skewed when in an electric field, giving rise to increased emission, and a lower observed energy position in DLTS.

Modifying expression (3.9) for the influence of the λ-region, and differentiating with respect to the depletion depth at the pulse voltage, the local trap concentration can be found as:

$$N_t(W_p - \lambda) = -\frac{qW_r^2}{\epsilon}\left(\frac{W_p}{W_p - \lambda}\right)N_d^+(W_r)N_d^+(W_p)\,\frac{\delta\left(\frac{\Delta C}{C}\right)}{\delta V_p}. \qquad \textbf{(3.11)}$$

Here the subscript p denotes values at the pulsing voltage, while *r* refers to the fixed reverse bias. In this expression variation in the ionized donor concentration (N_d^+) is also allowed, and further details on the derivation can be found in Ref. [3].

3.3 Thermal Admittance Spectroscopy

Thermal admittance spectroscopy (TAS) [3, 7, 8] , like DLTS, also uses the depletion region of a reverse biased Schottky contact to probe electronic states. However, complimentary to DLTS, TAS primarily probes the shallower dopant levels closer to the band edges.

In addition to the description above, capacitance can also be viewed as the ability of a material to hold charge (Q), i.e. as $C = dQ/dV$. The capacitance is not measured directly, but through the voltage changes that occur in response to an applied alternating current (AC). Like for DLTS, it is the emission rate of the electronic state that is of interest in TAS. In the case of TAS, it is the relation between emission rate and the probing frequency of the AC that allows separation of different levels. If the frequency is sufficiently large, or the temperature is low, a relatively low emission rate will not be able to exchange charge carriers with the bands fast enough to give a measurable contribution to the capacitance. In this situation we say that the level is frozen out. TAS records capacitance, and simultaneously conductance (G), for different frequencies as function of temperature. For a given deep level the freeze-out shows as a step in capacitance and a peak in conductance at different temperatures for different frequencies, as illustrated in Figure 6. This example is from an n-type epitaxial gallium oxide sample, and as relevant here, the rest of the discussion uses terminology for n-type materials.

The peak in conductance is at the same temperature (T_{peak}) as the half of the capacitance step. Pairing data of the peak temperature T_{peak} with the frequency, here represented as angular frequency $\omega = 2\pi f$, an Arrhenius plot can be made as function of T^{-1} of the expression:

$$\ln\left(\frac{\omega}{T_{peak}^{x}}\right) \propto -\frac{E_C - E_t}{kT}. \qquad \textbf{(3.12)}$$

Here the exponent x is equal to 2 in most cases, while it reduces to 1.5 in the case of studying the shallowest dopant, where the freeze-out leads to increasing series resistance [3, 7, 9].

3.4 Secondary Ion Mass Spectrometry

Secondary ion mass spectrometry (SIMS) is a technique that allows detection of impurity elements in a material, with an unprecedented sensitivity. The principle of operation involves an accelerated ion beam incident on the sample that sputters off atoms or small clusters from the surface of the material. Ionic species called secondary ions are ensured a long mean free path by operation in ultra-high vacuum, and can then be accelerated towards the analyzer. In the analyzer, a mass spectrometer uses electric and magnetic fields to separate the secondary ions according to their mass-to-charge ratio, before they are detected by an appropriate choice of detector. This gives very high sensitivity for most elements, typically in the range of ppm to ppb.

In operation, the primary ion beam can be scanned across the sample, typically covering areas with some hundreds of micrometers on each side. The raw data from the measurements is intensity of mass-to-charge ratios as function of time and position, and as time proceeds, the sputtering digs deeper into the material and depth

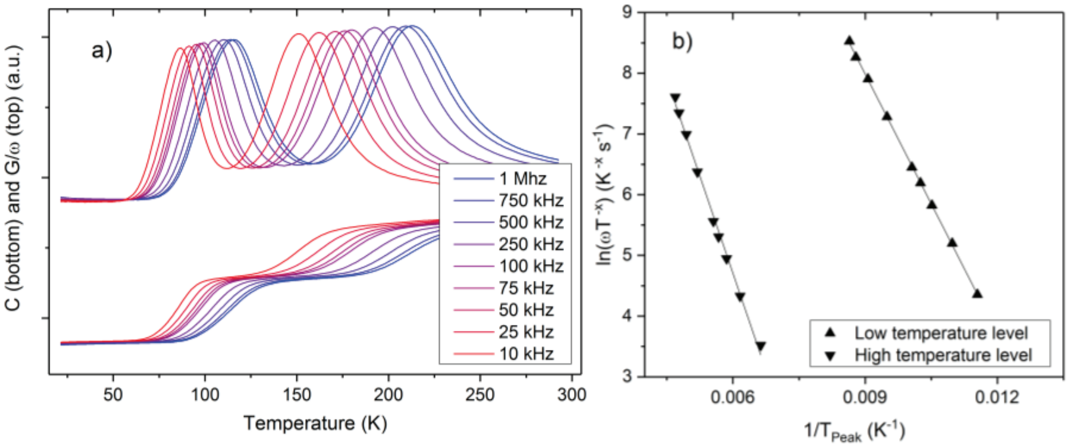

Figure 6 – (a) Capacitance and conductance signal from TAS, here exemplified by measurements on an epitaxial β-Ga_2O_3 sample with frequencies from 10 kHz to 1 MHz. The conductance is customarily normalized by the angular frequency. In (b) the Arrhenius plots for the two levels are shown.

profiles of the probed elements are achieved. By comparison to implanted reference samples, the intensity can be calibrated to give absolute concentration. Further, depth calibration is done by assuming constant erosion of the depth of the crater as determined by profilometry after the SIMS measurement. Hence, the output can be presented as absolute concentrations in lateral distribution maps, depth profiles or mass spectra; where the latter two are of particular importance here.

3.5 Altering the concentrations of intrinsic defects

Whereas the concentrations of impurity elements can be quantified with SIMS, the determination of intrinsic point defect concentrations is not possible in the same way. Instead we rely on altering their concentrations by external stimuli like annealing or irradiation.

3.5.1 Annealing

In this work, annealing has been done with tube furnaces, rapid thermal annealing (RTA) and in-situ with measurements requiring high temperature operation. This annealing has been done both in order to generate intrinsic defects, and to anneal out excessive damage from irradiation and implantation.

The tube furnaces allow annealing with the additional control of atmosphere by having a gas flow through the tube, and inert N_2 atmosphere have been used herein. While tube furnaces are resistively heated with limited heating and cooling rates, the easy access to insert and remove samples allows decent control over timing and quenching from high temperatures. However, shorter annealing and even faster rates, up to 50 °C/s, can be achieved in an RTA system when short annealing times and close control of re-equilibration is needed.

Reverse Bias Annealing (RBA) is, as the name indicates, to anneal under the simultaneous influence of a reverse bias voltage. RBA has been used, among other things, to switch between metastable states of Fe impurities in B doped Si [10], which was also attempted here. High temperature deep level transient spectroscopy measurements may be seen as a kind of RBA, as the sample is mostly biased in reverse; with outcome as is discussed in papers III and IV for gallium oxide. As we will see, the application of a reverse bias at high temperature may or may not provide extra stimuli for certain defect reactions.

3.5.2 Ion implantation and irradiation

Ion implantation and ion irradiation are two sides of the same coin, both involving shooting accelerated ions at a sample. With the former, the goal is to deposit the ions with a controlled depth profile, typically with closer control of distribution than can be achieved with diffusion and other methods. With the latter, the ions are of less importance, and the objective is to use the damage that the ions create in the sample when they collide with the host atomic structure.

In the interaction with the sample material, the incident ions collide, loose energy, and eventually stop. The energy loss leads to ionization and displacements of atoms in the sample, with the displacement being on the form of Frenkel pairs, which are pairs of self-interstitials and vacancies. Simulations of the collision processes from implantation, through the random sampling of Monte-Carlo methods, was done in this work using the code Stopping and Range of Ions in Matter (SRIM) by Ziegler [11, 12]. Material properties like composition, density, and threshold energies for displacement are inputs in the code, along with the implanted ion specie and acceleration energy. The output is projected range for the ions, the number of defects produced per incident ion, and distribution profiles of both ions and displacement events. The projected range denotes the depth in the material where the concentration of ions is at its peak, which also coincides with the peak in concentration of the displacement events. Meanwhile, whereas the concentration of ions is negligible in the region close to the material surface, the displacement events, in particular for lighter elements, takes place across the depth. For elements like H and He considerable defect concentrations can be generated in what we call the tail region between the surface and the peak. In this region the defect profile is approximately homogeneous, and without the influence of the ions themselves. This provides a good starting point for studies of the intrinsic defects that are generated.

Before choosing an irradiation dose to give a suitable concentration of defects, we also need to note that out of the generated defects, a large fraction of them immediately recombine and recreate the original structure. This is known as dynamic annealing, and typically amounts to ~99 % in Si and more than 90 % in SiC [13-15].

3.6 X-ray Absorption Spectroscopy and Fine Structure

In x-ray absorption spectroscopy, the absorption of x-ray irradiation is recorded as a function of the x-ray energy. Specifically, it is core-shell absorptions that are of interest, being distinctive to atomic species. But the abrupt absorption step is not only used for identification of species; on top of the atomic absorption edges there are modulations of the absorption coefficient that can be used to identify the local structure around the atom. This modulation is known under the abbreviation XAFS, for x-ray absorption fine structure, and may be further split into x-ray absorption near-edge structure (XANES) for the features close to the edge, and EXAFS for the extended XAFS at energies higher than the near-edge region.

The cause of the XAFS is the fact that the absorption probability from a core-shell excitation depends on the availability of other electronic states in the proximity. Quantum mechanically, the photo-electron can be seen as an outgoing spherical wave, and the back scattering from neighboring atoms gives interference that prompts oscillations in the absorption cross-section [16]. A mean free path determines how far the excited and backscattered electron can travel, and being on the order of 5 to 30 Å this gives XAFS the property of being a localized probe [17]. Hence, it is the immediate surroundings that are affecting the absorption, i.e. the neighboring atomic species, neighbor coordination number, the oxidation state, and interatomic distances.

Mathematically, the XAFS $(\chi(k))$ can be expressed as a sum over different neighbors [17]:

$$\chi(k) = \sum_j \frac{N_j f_j(k)}{kR_j^2} e^{-2k^2\sigma_j^2} \sin\left(2kR_j + \delta(k)\right), \tag{3.13}$$

where R_j is the distance to the neighboring atom, and σ_j the disorder in this distance. N_j is the number of equivalent neighbor sites, and $f_j(k)$ and $\delta(k)$ are scattering amplitude and scattering phase-shift from the neighbor, respectively.

Recording the XAFS signal can be done with several methods. One important and relatively simple method is to measure the transmitted x-rays and subtract from the incident beam flux. Such transmission measurements are well suited for samples where the element of interest is present as a major component, giving strong absorption. Meanwhile, since the XAFS is only a small portion of the total absorption, accurate measurements of the absorption coefficient with low noise is required, and for other sample types there are other more suitable detection methods. Most importantly, two recombination processes, Auger recombination and radiative recombination, compete to fill the core-shell hole and can be used to generate the XAFS signal. The filling of the core-hole takes place on a femtosecond time-scale [17]; where the Auger process dominates for lower energies compared to fluorescence from radiative recombination that is more dominant at higher x-ray energies [18]. Auger electrons, along with secondary electrons, can escape the surface of a material and be collected in a method known as total electron yield (TEY); and since these electrons originate from shallow depths the technique is suitable for recording surface specific properties. Secondary electrons are generated in large numbers, on the order of thousands per core-hole excitation, and some also with lower energy than needed to escape the sample, which can be detected by conductivity measurements [19, 20].

Fluorescence detection is the method that is most applicable to thick and dilute samples, and thus for samples where the atomic species of interest is present in trace amounts like an impurity element. For the fluorescence signal, well-known energy transitions like K_α are recorded, enabling separation from emission from other elements and scattered x-rays, and thus higher signal to noise ratio. To start with, the isotropically emitted fluorescence can also be selected over scattered x-rays, by consciously placing the detector, because the polarization of the source x-rays yields anisotropic scattering. Further, the detector should be placed as close to the sample as possible to collect as much as possible of the isotropic emission. With good control over the experimental setup such as the photon flux from the source and detector positioning and sensitivity, impurity concentrations on the order of 10^{18} cm^{-3} can be detected [19]. However, the ability to detect an atomic specie also depends on the contrast to the matrix elements, and in some very favorable cases the detection limit can be as low as 10^{14} cm^{-3} [21].

In order to have a source of x-rays with high enough intensity, a synchrotron is used. The XAFS measurements in this work were carried out at the Swiss-Norwegian beamline (SNBL) within the European Synchrotron radiation facility (ESRF). The SNBL is one of totally 40 beamlines that is taken out around the 844 meter circumference electron accelerator in Grenoble. From bending the 6 GeV high energy electron beam using magnetic fields, high intensity x-ray irradiation is emitted tangentially, and SNBL utilize a wide spectral range from 4 to 70 keV. Another requirement is high energy selectivity, and around 1 eV resolution at 10 keV can typically be achieved with Si monochromators [17]. At SNBL the Si (111) pair monochromator, is also supplemented by Cr and Au coated mirrors to remove harmonics. With this setup, at the relevant energies, we anticipate an x-ray photon-flux to the sample around 10^9 mm^{-2}s^{-1}. A schematic representation of a beamline setup is provided in Figure 7.

3.7 Combining x-rays and capacitance

A challenge with XAFS is the inherent inability to separate between different configurations of one element. If an element is present in the material in two or more different environments, the XAFS will provide a concentration-weighted average of these. Incidentally, this leads to information about atoms that are involved in defect complexes drowning in the main signal if the same atom is also a bulk element.

An intriguing idea to overcome this problem was proposed by Ishii et al. around the beginning of the 2000's [22-25]. The idea involves recording XAFS through a capacitance signal (CXAFS) that selectively reports on only the defect-related atom. This site-selectivity is reasoned to follow from the recombination mechanism of the core hole. When a core hole is filled, it is generally accepted that this is dominantly happening from the next higher energy; for example, an L-shell electron filling a K-shell hole. However, this leaves an L-shell hole, and the filling continues in a cascade of lower energy transitions. Ishii and his group proposed that this cascade ends with the emptying of an intra-bandgap deep level, if there is such a level related to the excited atom. Simplifying the cascade, this mechanism can be interpreted as is illustrated in Figure 8 (a). Further, if this atom is in the depletion region of a rectifying contact, where no free electrons are available, the deep level will remain in an altered

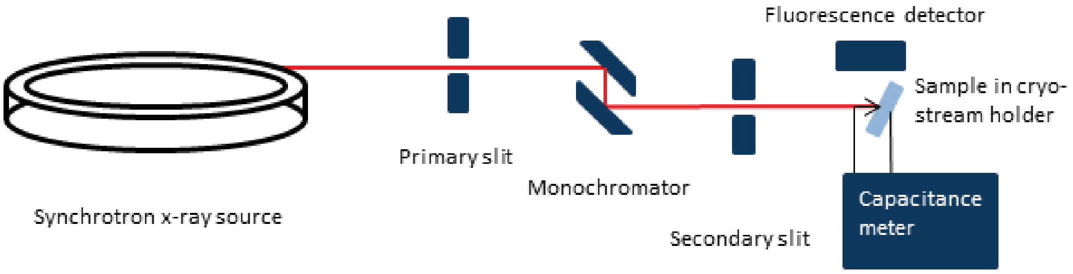

Figure 7 – Schematic of a synchrotron and the experimental setup to achieve XAFS measurements.

charge state. Actually, the deep level needs to not only be in the depletion region, but in the λ-region, since it is a requirement that it also needs to be filled initially [24]. If this is fulfilled, it is argued that the ionization from the x-ray excitation remains localized, and that there will be a change in the charge concentration and accordingly also in the capacitance of the device [22].

Ishii et al.'s material system was Se doped AlGaAs, where the DX-center, a deep level forming from a complex between the donor and an un-known intrinsic defect, was the objective of the study. Recording XAFS of the Ga K-edge from both capacitance and fluorescence, the authors argued that the difference between the signals is due to the capacitance signal's origin from only defect-related Ga. On the other hand, the fluorescence signal comes from all Ga atoms, where the defect related signal is negligible due to the low concentration. A sharper edge jump, and an edge-shift to slightly lower energy in the capacitance signal compared to fluorescence was interpreted as a sign of large lattice relaxation around the DX center [22]. The results were elaborated in Ref. [25] where the capacitance response is explained as a displacement current, different from the regular conduction current from photo-generated free carriers that is previously known to carry the same information as traditional XAFS [26, 27]. Furthermore, the same authors also suggested a scanning version of their measurements, in order to achieve spatial resolution of the sample surface like in atomic force microscopy [28].

Fujioka et al. [29] proposed a variation of the combination of capacitance and x-ray stimulation in 2004, with a method named Synchrotron-Radiation DLTS (SR-

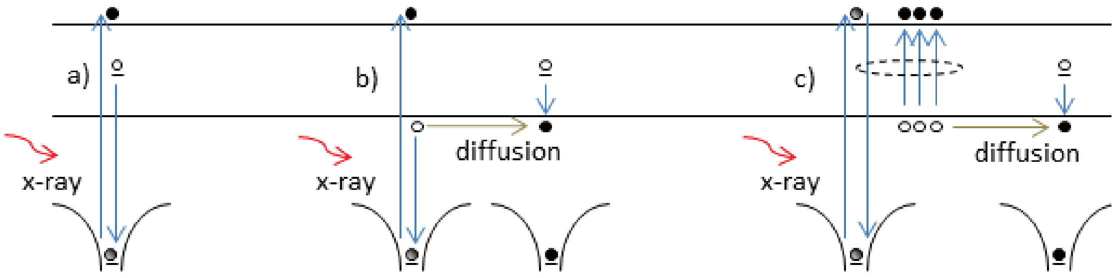

Figure 8 – Potential mechanisms in the later stages of the recombination of core-holes generated by x-ray excitation. (a) shows the mechanism suggested by Ishii et. al [22], (b) a mechanism that involves diffusion of a valence band hole after radiative recombination of a core-hole, and (c) auger recombination leading to generation of electron-hole pairs and subsequent diffusion and interaction with deep levels. Figure adapted from Ref. [20].

DLTS). This draws from optical DLTS variations, where the excitation of deep levels is stimulated by light. In SR-DLTS, the capacitance transients come from the interaction between the x-ray excited core electron and deep levels from a selected atomic component of the sample [29]. With x-ray energy related to a known impurity element, the DLTS response is reported to vary for certain signatures depending on the x-ray energy being above or below the absorption edge. Henceforth, the DLTS signature is attributed to that particular atomic specie. Specifically, Fujioka et al. were able to distinguish a level located in an AlN layer from another in the AlN/Si-interface of their Al/AlN/Si heterostructure [29].

The mechanism of interaction between valence electrons and the relaxation of core-hole excitation proposed by Ishii et al. has also met some resistance. Bollmann et al. goes far in stating that the capacitance signal cannot contain different information than the traditional methods [20, 30, 31]. These authors compare measurements of short-circuit photocurrent, steady-state impedance, and x-ray capacitance with traditional fluorescence measurements, and find no difference that can be attributed to site-selectivity. Further, a development of the capacitance method is suggested, by recording transients in capacitance following from applying x-ray irradiation at a constant energy. However, also this is found to not support the claimed site-selectivity, and it is concluded that capacitance can be used to carry the regular XAFS information, but with inferior signal-to-noise ratio compared to photocurrent measurements. Figure 8 (c) shows how Bollmann et al. interprets the capacitance signal as an interaction between diffusing secondary electrons from the Auger recombination and the deep levels, whereas (b) shows similar for radiative recombination. Here, the diffusion effectively removes the tie between the excited atom and the deep level. And since one can expect on the order of thousands of electron-hole pairs to be generated from a single hard x-ray absorption event, this process is deemed much more likely [20]. Bollmann et al. also argues that, from a theoretical point of view, the selective excitation of defect states will be negligible due to the small cross-sections for ionization, and further complicated by the fact that the method only considers the narrow λ-region.

Later Konovalov et al. [32] used L-edge absorption instead of K-edge, to take advantage of the larger ionization cross-sections. Whereas they acknowledge Bollmann et al.'s dismissal of the CXAFS, they establish the possibility of an alternative site-selectivity through the photoconductivity. Inspired by Fujioka et al. [29], Konovalov et al. reported time and temperature dependent conductivity depending on what core-electron was excited [33]. They elaborate on these results in Ref. [32], where comparison of modulated photoconductivity and thermally stimulated current measurements are interpreted in favor of site-selective excitation. Bazlov et al. [34] builds on the work on capacitance transients by Bollmann et al. and records what they call CapTXAS (from Capacitance Transient X-ray Absorption Spectroscopy), and find it more suited than photocurrent to handle samples with insulating top layers. Furthermore, they discuss the CapTXAS and photocurrent methods viability to collect XAFS from interface regions in their heterostructures, although other site-selectivity is not claimed.

Chapter 4

Defects in Gallium Oxide

4.1 Introduction to Gallium Oxide

Gallium oxide is a transparent semiconducting oxide that was first structurally characterized in the 1950's [35], while development of melt growth synthesis and characterization of optical properties continued in the 1960's [36, 37]. Towards the 1990's some development of thin film deposition routines took place, motivated among other things by applications in gas sensing detectors [38]. Then, from the early 2000's the material system has seen increasing research attention, based on several important factors. Firstly, the very rapid development of electronics has made silicon-based technologies approach their fundamental limits, especially considering the performance of RF- and power electronics. This has motivated search for, and development of new material systems, like SiC and GaN. While these materials have improved properties compared to Si, and now an established technological presence, gallium oxide has fundamental properties that hold promise for device performance going even further. Secondly, the availability of melt growth synthesis techniques has allowed fabrication of larger bulk wafers of gallium oxide, enabling both fundamental material studies and engineering of electronic devices. The synthesis techniques also pose an advantage of gallium oxide compared to SiC and GaN that both require more time-consuming and costly synthesis. Furthermore, a wide range of n-type conductivity can be controlled by doping, and promising prototype devices has already been presented.

4.1.1 Fundamental properties of β-Ga_2O_3

With the sesquioxide chemical formula Ga_2O_3, gallium oxide crystallizes in several polymorphs that are labelled α, β, γ, δ, and ε. Of these, β-Ga_2O_3 is the most stable at ambient conditions, and thus most technologically relevant, most studied,

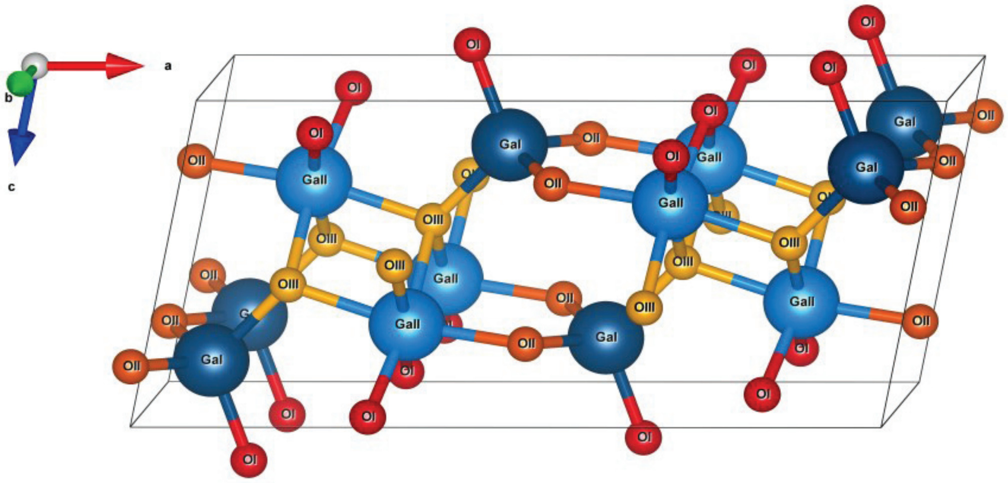

Figure 9 – Monoclinic structure of the β polymorph of Ga_2O_3. Two inequivalent Ga sites are colored in blue, and the three O sites in warmer colors. Labeling follows the notation of Refs. [2, 40], and the visualization was made with Vesta [41].

and the subject of the studies reported in this work. On the other hand, the other polymorphs may see increasing relevance with future development of thin-film deposition techniques. The monoclinic structure of β-Ga_2O_3 belongs to the space group c2/m, and has lattice parameters a=12.21 Å, b= 3.03 Å and c= 5.79 Å with an angle between the a and c axis of 103.83° [39]. In this structure the oxygen sub-lattice can be imagined as a distorted face-centered cubic structure, where the gallium resides in two inequivalent sites. Following the notation given in Ref. [40], Ga(I) is tetrahedrally coordinated and Ga(II) octahedrally coordinated. From this the oxygen sub-lattice has three different environments; where O(I) and O(II) are threefold coordinated, and O(III) has a fourfold coordination. The structure is illustrated in Figure 9, with the inequivalent sites represented by different colors. With this relatively complex structure, a complex defect situation may also be anticipated, particularly considering that vacancies can exist on all the different lattice sites and give different electronic signatures that affect the material and devices differently. Further discussion of these parameters will be given later, in section 4.3.1.

It is primarily the exceptionally wide bandgap, reported in the range 4.7-4.9 eV [37, 42], that has spurred the recent attention of researchers to β-Ga_2O_3. This bandgap is of indirect nature, as mentioned in section 2.1, but with only a few tens of meV separating the indirect transition from the direct it is effectively direct for practical purposes [43, 44]. In the conduction band, the effective mass of electrons in β-Ga_2O_3 have been calculated to be close to isotropic with values between 0.27 and 0.28 m_e for different directions [44], agreeing well with experimental observations [42, 45]. Combined with relatively high electron mobility – experimental values of 153 cm^2/Vs have already been reported [46] – this gives a good foundation for n-type material suited for device production. Theoretical studies have found an upper limit for electron mobility of more than 300 cm^2/Vs in material with donor concentration around 10^{19} cm^{-3} [47]. Meanwhile, low hole mobility and lack of acceptor dopants remains a challenge that will be further discussed in section 4.2.2.

Scaling with a close to square proportionality to the bandgap, the critical breakdown electric field is another important parameter for power electronic devices. Values have been predicted in the range 5 to 9 MV/cm for β-Ga_2O_3 [48, 49], using methods described by Ref. [50]. Also radiation hardness is a feature of wide bandgap semiconductors, attributed to strong binding [1], and together with the inherent stability of oxide semiconductors to oxidation, it makes β-Ga_2O_3 an attractive material for applications under harsh conditions and high temperature [51]. Meanwhile, measurements of the thermal conductivity reveal low values, and a strong anisotropicity, with the highest value seen along the b-axis of 29 W/mK, as opposed to 11 W/mK along the a-axis [52]. Due to this, efficient heat management in devices will be a crucial engineering challenge.

4.1.2 Prospects for applications

While power electronics might not be a topic as immediately appealing to the public eye as solar cells or battery technology, it too plays an important role in making the energy system more efficient and thus mitigating the global climate problems. In fact, in all conversion processes between different forms of electric power, power electronics are involved, also in the inverters that make grid compatible AC out of the DC from solar panels. In the existing power grid, the distribution system for electric energy requires multiple conversion processes, and losses during transmission and distribution amounts to a global average of more than 8 % of all produced electricity [53]. With increasing implementation of renewable sources and storage, the smart grid development will depend even more on efficient and high-performance power electronics in the future. For these purposes, with the properties described in the previous section, and summarized in Table 1, β-Ga_2O_3 proves a promising candidate. Table 1 also includes comparison to other relevant material systems; and for evaluating the relative performance potential, some power electronics figures of merit are provided. Baliga's figure of merit (BFOM) is based on how the performance-indicating device parameters on-resistance (R_{on}) and breakdown voltage (V_{br}) relates to the material properties critical breakdown electric field (E_C), permittivity (ε) and majority carrier mobility (μ) [54];

$$\frac{4V_{br}^2}{R_{on}} = \varepsilon\mu E_C^3 \equiv BFOM. \tag{4.1}$$

This is relevant for unipolar transistors operated at low frequencies, assuming power loss only takes place by dissipation through the on-resistance. The breakdown voltage is the maximum voltage a transistor can block in the off-state, and the on-resistance is the resistivity per area in the on-state. We see that the BFOM depends on the mobility of the majority carriers, a dependence that comes from the on-resistance, and favors semiconductors such as gallium arsenide with high mobility. However, the cubic dependence on the critical field favors more strongly the wider bandgap semiconductors like gallium oxide, as in turn the critical field depends approximately squarely on the bandgap magnitude. [51, 55]

Table 1 - Fundamental properties of gallium oxide and relevant materials for applications in unipolar devices. The values are taken from Ref. [56], except where otherwise stated.

	Si	GaAs	4H-SiC	GaN	β-Ga_2O_3	Diamond
Bandgap E_G (eV)	1.12	1.4	3.2	3.39	4.8 – 4.9 [37, 42]	5.6
Electron mobility μ_n (cm^2/Vs)	1450	8500	950	2000	300 [57]	4000
Hole mobility μ_p (cm^2/Vs)	450	400	115	350	10^{-6} [58]	3800
Critical electric field E_C (MV/cm)	0.3	0.4	3	5	9 [49]	10
Electron saturation velocity v_S (cm/s)	10^7	2×10^7	2×10^7	2×10^7	2×10^7 [59]	3×10^7
Thermal conductivity λ (W/cmK)	1.3	0.54	5	1.3	0.11–0.29 [52]	20
Relative permittivity ε_r	11.7	12.9	10	8.9	10.2	5.7
Calculated BFOM $\varepsilon\mu_n E_C^3$ (normalized to Si)	1	14.4	560	4857	4870	49776
Calculated JFOM $v_S E_C/2\pi$ (normalized to Si)	1	2.7	20	33	60	100

Other figures of merit have been suggested too, and relating more to high frequency operation the Johnson FOM is often mentioned;

$$JFOM \equiv \frac{v_S E_C}{2\pi}, \tag{4.2}$$

where v_S is the saturated drift velocity [60], and it is evident that also JFOM favors wide bandgap materials. Further in-depth review of these properties can be found in Refs. [1, 51]. As is evident from Table 1, the material properties of β-Ga_2O_3 add up to a favorable comparison to the other relevant materials.

While β-Ga_2O_3 is still in its infancy compared to the other materials, several promising prototype devices have been shown over the last years. Due to the unavailability of p-type material, these devices are unipolar, and the Schottky rectifying diode is the simplest, two-terminal device. Several high work function metals, including Au, Ni, Pt and Cu, provide good rectification, with high energy barriers and low ideality factors with β-Ga_2O_3 [61-66]. Recently, ten orders of magnitude rectification was reported using Pt as contact material [67], and further optimization of edge termination with field-plate has allowed record-high breakdown voltage of 1076 V with the same materials [68]. Meanwhile, even higher breakdown voltages are predicted if even more sophisticated edge termination techniques from Si and SiC processing is fully adapted [49]. Also, for three terminal devices, promising devices have been shown, including MOSFETs and MESFETs [39, 69-72]. In a MOSFET on epitaxial material, a breakdown voltage of 755 V has been achieved together with drain-source current with an on-off ratio of nine orders of magnitude [73]. The theoretical excellence of β-Ga_2O_3 has also been demonstrated experimentally with a mean gate-to-drain field corresponding to 3.8 MV/cm, and by that surpassing the theoretical limit for SiC [69]. Radio frequency (RF) operation has also been shown possible with β-Ga_2O_3. High trans-conductance at an extrinsic cut-off frequency of 3.3 GHz and maximum oscillating frequency of 12.9 GHz has been shown in a MOSFET structure [74].

In addition to power electronics, applications of the ultra-wide bandgap of β-Ga_2O_3 is foreseen in deep-UV solar blind photo-detectors [1]. With cut-off wavelength in the range 250-280 nm, such detectors can be used in a range of applications including flame detection, and practical devices have already been demonstrated [75]. Furthermore, hetero-structures may become useful; InGaN-based LEDs on β-Ga_2O_3 substrates has been considered for making use of β-Ga_2O_3's higher electrical conductivity and high optical transparency in the visible and UV ranges [51]. And conversely, using thin films of β-Ga_2O_3 on more heat conductive substrates has been suggested as a means to surpass the issue of low thermal conductivity [1, 76].

4.1.3 Synthesis

Compared to the two primary competing materials for power electronics, GaN and SiC, β-Ga_2O_3 has the advantage of availability of melt growth synthesis. Tsao et al. [51] remarks that 2 inch substrates of β-Ga_2O_3 are now price-competitive with GaN, and notes that with the present low volume, β-Ga_2O_3 prices have room to drop considerably, and even approach the price of sapphire if production is scaled up.

Melt growth synthesis can be realized with several different methods for β-Ga_2O_3. The first example was achieved in the 1960's with the Verneuil method, to yield crystals reaching 1 cm in diameter, and ranging from insulating to highly conductive depending on the synthesis parameters [36, 77]. Since then other methods have been developed to yield higher quality material and more efficient production. Like the Verneuil technique, float-zone synthesis uses no crucible, thus allowing high oxygen pressure during synthesis and avoiding contamination. The melting occurs in a moving zone under irradiation from halogen lamps and monocrystalline rods can be grown from sintered powders, as described in Ref. [78]. However, high temperature gradients and low volume processing leads to relatively low structural quality [39].

The best quality, and most studied, crystals are achieved from Czochralski and Edge-defined Film-Fed Growth (EFG). These methods use crucibles, but contrary to another method – the Vertical Bridgman technique [79] – the solidified material does not contact the crucible, so there is no conflict from different thermal expansion [39]. In the Czochralski technique, a seed crystal is dipped into the melt and pulled out under rotation, to yield a high quality monocrystalline β-Ga_2O_3 boule [80, 81] . Wafers up to 2 inches are available with orientations (100), (010), and (001), whereas realization of bigger boules is problematic due to difficulty to achieve high enough oxygen content under the high temperature melt conditions [39]. In EFG growth, material in an iridium crucible is heated inductively, and the melt is transferred by capillary forces through a narrow slit that shapes the crystallizing material. Wafers of 2 inches are commercially available today, while 6x6 inch slabs have been demonstrated [45]. For both EFG and Czochralski, pulling of the crystal is required, which puts constraints on the size that can be made and the direction of growth due to the propensity of β-Ga_2O_3 to cleave parallel to the (100) and (001) families of planes.

Regarding thin-film synthesis, several techniques can be used, including Metal-Organic Chemical Vapor Deposition (MOCVD), Pulsed Laser Deposition (PLD), MIST-CVD, Atomic Layer Deposition (ALD), Molecular Beam Epitaxy (MBE), and Halide Vapor Phase Epitaxy (HVPE) [1]. Of these, the two latter are commercially available on bulk β-Ga_2O_3 substrates, and relevant for this work. HVPE growth of films is considered to be the best developed technique, and although polishing is needed to give a good surface morphology, dislocation densities down to 10^3 cm^{-2} can be achieved [82, 83].

4.2 Shallow electronic states

In the present section and the next we will use the slightly arbitrary distinction of shallow and deep electronic states to discuss intentional doping and unintended states from impurities and intrinsic defects.

4.2.1 Donor doping

Donor doping is readily available in β-Ga_2O_3, by several dopants providing shallow levels; in fact, shallower than might be expected for such a wide bandgap material. Through the initial studies of β-Ga_2O_3 it was found that samples without intentional doping showed increasing charge carrier concentrations upon annealing in reducing atmospheres. Hence, it was concluded that the oxygen vacancy was the dominant donor in these samples [77]. However, as is also the case for other oxide semiconductors, it is now known that the oxygen vacancy cannot explain n-type behavior, and that another mechanism must be responsible for the increased conductivity [84]. Varley et al. [2] have from first-principle simulations shown that the oxygen vacancy have a too deep donor level to contribute substantial concentrations of electrons to the conduction band. Instead they find that common unintentional impurities like Si, Ge, Sn, F, Cl, or H can provide shallow levels [2]. Among these, H is an impurity that is present in most situations and materials, and its presence in oxide semiconductors has been reviewed in Ref. [84]. Experimental knowledge of H is made difficult due to its often relatively high mobility, propensity to form complexes, and high detection limits in methods like SIMS. Somewhat contradictory to the theoretical predictions, annealing in H atmosphere does not seem to increase carrier concentrations drastically, unless previous annealing treatments to reduce existing concentrations were done [80]. Meanwhile, experiments with muons indicate that interstitial H will act as a shallow donor [85].

Intentional doping in commercially available bulk substrates and thin films is now commonly done with Sn and Si [86], and with controllable concentrations up to

10^{19} cm^{-3} high conductivity is achievable [48, 87-90]. Experimental approaches have also shown that Si may be correlated with the charge carrier concentrations in unintentionally doped samples [61, 87]. Farzana et al. [91] uses Ge instead of Si doping in their thin-films, as oxidation of a Si source in plasma-assisted MBE would be problematic. With Ge, charge carrier concentrations can also be controlled in the range 10^{16} to 10^{20} cm^{-3}, and it is argued that Ge is a better fit for Ga substitution due to more similar ion-size [92]. Transition metal dopants have been considered from a theoretical point of view, and considering W, Mo, Nb, and Re, Nb with donor level at 30 meV below E_C is considered the best candidate [93].On the other end of the n-type conductivity scale, to achieve semi-insulating substrates with charge carrier concentrations down to 10^{15} cm^{-3}, compensating acceptor doping has to be done. Whereas shallow acceptors are not readily available, as will be discussed in the next sub-section, deeper acceptor levels from Fe, Mn, or Mg can be used to effectively limit the n-type conductivity [57, 80, 94, 95].

Previous studies have reported donor levels from dopants to be in a range from 15-35 meV below E_C [61, 85, 96]. Son et al. [97] conducted electron paramagnetic resonance (EPR) experiments on UID samples to reveal a single electron level at 44-49 meV. However, banding shifts the observed level closer to the conduction band for higher concentrations, and with 10^{18} cm^{-3} charge carriers, the ionization energy drops to around 15 meV, explaining the variability in experimentally reported values in literature [61, 97].

Deeper donors can also exist in β-Ga_2O_3; Neal et al. [98] has studied (2;¯01) oriented bulk β-Ga_2O_3 by Hall and TAS, and finds a level with values from the two methods of 110 and 131 meV from the CBM, respectively. Their analysis of such deep donors, only being partially ionized at operating temperatures concludes that the on-resistance will increase and the breakdown voltage decrease with increasing concentration. Hence, control over this specie is called for, and in particular removal or reduction of its concentration in the drift layers of devices is important to achieve the highest possible performance. Of intrinsic defects, antisites and interstitials are considered possible candidates for these levels[98], whereas vacancies are discarded due to predictions indicating deeper levels [2, 40, 99, 100]. An extrinsic impurity may also be considered the cause of this level, and in particular Si on the octahedral Ga(II) site is suggested [98], bearing in mind that Si has a shallower level when substituting Ga(I) but can be found on both lattice sites [2, 101].

4.2.2 Acceptor doping

Several factors play a role for the availability of p-type conductivity in a material. Firstly, acceptor dopants must be available, with sufficiently shallow electron states to give considerable ionization at relevant temperatures. Secondly, if existing, the material must be possible to synthesize with substantially higher concentrations of acceptors than of any compensating native or impurity donor levels. And thirdly, the mobility of holes in the valence band must be high enough to yield a usable conductivity.

Some experimental reports on observations of p-type conductivity has appeared in the literature; in particular in nano-wires, doped with N [102] or Zn [103]. Indeed, for the choice of dopant, N is a reasonable candidate from the perspective of its ionic radius being similar to O which is favorable for substitution. However, theoretical calculations of N incorporation indicates deep acceptor levels, and that N readily makes complexes with vacancies in β-Ga_2O_3 that act to compensate potential p-type behavior [104]. Meanwhile, Kyrtsos et al. [105] points at the limited number of experimental p-type reports being a sign of poor reliability and reproducibility in these samples, and calls for more extensive studies. A very recent experimental study of highly pure hetero-epitaxial films of β-Ga_2O_3 on sapphire reports p-type conductivity with mobility up to 0.2 cm^2/Vs at room temperature with concentration around 2×10^{13} cm^{-3} [106]. However, the acceptor is unknown, and close control over compensating donors, among them oxygen vacancies [105], would be needed to scale this up to more usable hole concentrations. Further, also measurements of electron beam induced current (EBIC) indicates relatively mobile holes, showing hole diffusion lengths of up to 400 nm in HVPE samples [107].

From the perspective of theoretical modelling the extent of investigation of p-type behavior is more developed. Unfortunately, most results imply that realization of p-type β-Ga_2O_3 will not be possible. Substitutional impurity elements on the two inequivalent Ga sites have been simulated using density functional theory [105]. This was done for Li, Na, K, Be, Mg, Ca, Cu, Au, and Zn; all elements that were considered likely to contribute acceptor states based on their origin in groups 1, 2, 11, and 12 in the periodic table. As all of the aforementioned elements proved to have levels further than 1 eV from the valence band maximum it was concluded that none of them could contribute to p-type conductivity. Furthermore, calculations have shown that self-trapped holes are more energetically favorable than free holes in β-Ga_2O_3, and that these may be further stabilized by defects [58]. This is attributed to the orbital composition of the valence band, dominated by O 2p orbitals with small dispersion that leads to high effective mass, and the formation of small polarons. The oxygen dominated valence band is common to most oxide semiconductors, with the notable exception of copper oxides, where the Cu 3d states mix in to give a more favorable band structure for doping [105]. In β-Ga_2O_3, Varley et al. [58] predicts the mobility to be as low as 10^{-6} cm^2/Vs for holes in the valence band, and concluded that this constitutes an insurmountable obstacle to achieve p-type behavior.

4.3 Deep levels

From research on other material systems it is well known that deep level defects influence the performance of devices by affecting properties like threshold voltage, and high frequency operation performance [108, 109]. Deep levels in β-Ga_2O_3 have been studied with several methods, and the first study using DLTS was done by Irmscher et al. for Czochralski grown material [61]. Three levels, E1, E2 and E3 were observed at 0.55, 0.74 and 1.04 eV below E_C, respectively. The E2 state is present in all the samples they studied, with concentrations correlating to the amount of compensating acceptors, as deduced from Hall measurements. Meanwhile they speculate the E1 and E3 levels to be related to Fe and Co impurities, as these elements were seen by EPR measurements [61]. Zhang et al. [110] similarly observed three levels that must be assumed to be the same ones in EFG material, with energy positions at 0.62, 0.82 and 1.00 eV below E_C. In addition, two more levels in the remainder of the bandgap were found located at E_C-2.16 and E_C-4.40 eV, with the second one as the most prominent with concentration of 1.5×10^{16} cm^{-3} [110]. The latter levels were seen by using deep level optical spectroscopy (DLOS), which is a method related to DLTS, where emission from the deep levels is triggered by monochromatic light rather than temperature after being filled by bias voltage pulsing [111].

DLTS and DLOS studies have also been done on samples of plasma-assisted MBE, by Farzana et al. [91] to reveal a total of seven levels. Of these, there are two relatively shallow levels at 0.18 and 0.21 eV below the conduction band minimum seen with DLTS, and based on calculations, one of these are speculated to be from a potential double-donor behavior of the main dopant, Ge [91]. One more level, corresponding to the E3 level mentioned above was seen with DLTS, whereas the E2 level that is abundant in other materials was not observed. The remaining four levels were observed by DLOS at 1.27, 2.00, 3.25, and 4.37 eV below E_C. The first of these with relatively low concentrations, while the three others in more substantial numbers, on the order of 10^{16} cm^{-3}. Whereas the levels at 1.27 and 3.25 had not been described before, the two others resemble the ones reported in EFG material by Zhang et al. [110]. Remarkably, the level at 4.37 eV match the previous description well regarding both trap signature and concentration, despite material synthesis of very different kind. This is in agreement with speculations of its origin from self-trapped holes, as predicted in this energy range by Refs. [58, 99, 112].

Using positron annihilation spectroscopy, Korhonen et al. have studied the concentrations of gallium vacancies [100]. The recombination of implanted positrons with electrons reveals V_{Ga} concentrations on the order of 5×10^{18} cm^{-3}, capable of accounting fully for the compensation observed in their Si doped films. Kananen et al. have also studied the presence of V_{Ga}, and determine that both doubly and singly ionized V_{Ga} are present in the material at room temperature [113]. High degree of localization of the associated hole on neighboring oxygen is interpreted as a sign that these levels are not of a particularly shallow nature [113].

4.3.1 Predictions for intrinsic defects

In parallel with the experimental characterization effort, first principles calculations reports in the literature investigate the expectations for electrical properties of intrinsic defects and their complexes [2, 40, 99, 114-117]. Most of the primary defects have been predicted to be electrically active, with transition levels within the bandgap. Hybrid functional calculations have suggested gallium vacancies, as well as their complexes with hydrogen, to be deep acceptors, whereas the gallium interstitial to be a shallow donor [40, 116]. Of the two configurations of gallium vacancies the $V_{Ga(I)}$ is energetically more favorable than $V_{Ga(II)}$ [40]

In the oxygen sub-lattice, both the vacancies and interstitial are expected to be deep donors and thus electrically neutral for most practical purposes in n-type materials, where the Fermi level position is close to conduction band minimum [2, 99]. Furthermore, the primary defects are predicted to be mobile at relatively low temperatures; as recent theoretical estimates suggest that the activation barrier for vacancy migration is in the range of 0.5 to 1.6 eV, while that for the gallium interstitial (Ga_i) may be as low as 0.1 eV [115, 116]. Regarding diffusion, it is also found that the anisotropy of the material may favor diffusion along the b-axis for certain defects

[116]. Kyrtsos et al. considers several metastable intermediate states for the gallium vacancies in their work, and predict the V_{Ga} to be mobile at around 500 K [115]. Similarly, the oxygen vacancies are predicted to be mobile at slightly higher temperatures, down to about 800 K [115].

4.4 Irradiation damage

As mentioned previously, high radiation tolerance is expected for materials with wide bandgaps due to strong binding, and accordingly β-Ga_2O_3 is considered for applications where this is important. Radiation studies of this material has recently appeared regarding irradiation with protons [107, 118, 119], electrons [120, 121], neutrons [122], and gamma rays [123].

Polyakov et al. [118] studied the influence of 10 MeV proton irradiation on 10 μm HVPE homo-epitaxial films. Using irradiation dose of 10^{14} cm^{-2} they report reduction in charge carrier concentration from 3.8×10^{16} cm^{-3} to 2.5×10^{15} cm^{-3}. Before irradiation, their samples show DLTS signatures of the three known levels E1-E3, and DLOS reveals the presence of the level 2.3 eV below E_C. After irradiation they describe increasing concentrations of the E2 level and the 2.3 eV level, in addition to generation of a new level 1.2 eV below E_C. Also some signs of hole traps at 0.4 and 1.2 eV above the valence band is discussed [118]. The level at 4.4 eV from E_C, seen in different materials by several groups [91, 110] is not recorded by Polyakov et al., as optical excitation was not available above 3.4 eV [118]. Meanwhile, the concentrations of the observed levels are not sufficient to explain the compensation of charge carriers, so the authors hypothesize a level closer to the valence band to be the cause. Further, in these same samples, the authors measure relatively long diffusion lengths for holes, whereas this hole diffusion length is halved after irradiation [107, 118]. Also in the same samples, an investigation of the compensation and recovery shows that the carrier removal rate is 236 cm^{-1} , and that increasing recovery takes place at temperatures from 300 to 450 °C [124]. Also rapid thermal annealing at 500 °C has been shown to recover irradiation damage from protons, enabling Yang et al. to restore the properties of a FET without compromising the structure [125]. Furthermore, Weiser et al. [119] have also investigated proton irradiated samples, with the additional aspect of H and deuterium (D) present in the samples from in-diffusion and implantation. From IR studies of the vibrational stretch modes of OH and OD, they find Ga vacancies decorated with two H as the most common outcome [119].

Like for protons, electron irradiation has also been shown to cause charge carrier concentration reduction, but with a rate of 4.9 cm^{-1} it is considerably less severe than for protons [121]. The irradiation done with 1.5 MeV electrons and fluences order of 10^{16} cm^{-2} also caused reduced rectification and increased ideality factor and series resistance in the Schottky contacts.

For space applications, the influence of neutrons is also important, especially considering displacement damage causing long term degradation. Chaiken and Blue [122] have determined the displacement cross-section of neutron irradiation as function of energy to enable comparison with other material system and other forms of irradiation. Their calculation methodology was evaluated against Si literature and confirmed reliable in the range 300 eV to 7 MeV. Arehart et al. [126] studied the influence of neutrons, by subjecting samples to doses of 4×10^{15} cm^{-2} at 2 MeV, and saw reduction in charge carriers with a rate 20 cm^{-1}. Additionally, two new levels observed with DLOS appeared after the irradiation, at 1.29 and 1.88 eV below E_C, of which the latter was the dominating specie.

Wong et al. [123] studied the effect of gamma radiation on MOSFET's, with doses up to 1.6 MGy(SiO_2), seeing no significant generation of displacement defects. Meanwhile, there were signs of interface charge trapping and damage to the dielectric, giving gate leakage and drain current dispersion.

Pearton et al. summarizes that all in all, with the information available at present the radiation properties appear to be similar to GaN devices under the same conditions [1].

Chapter 5

Summary of results

Our first paper sets the stage for the detailed β-Ga_2O_3 studies presented in the later papers, by describing the routines of sample preparation and determination of quality of Schottky contacts. It also describes some differences between samples with (010) and (2;¯01) orientation, and contributes to the literature of deep levels by being the first report of the E4 level observed at about E_C -1.48 eV. In the remainder of this chapter follows a review of our other papers, as well as some additional description of shallow levels in β-Ga_2O_3 and a more in-depth account of the capacitance x-ray absorption studies.

5.1 Iron in β-Ga_2O_3

From Paper I it was in particular the large difference in concentration of the E2 level between the different samples that spurred our interest. SIMS measurements had shown a comparable difference in the concentrations of Fe in the samples, whereas other impurities were also present and we were not able to conclude on the causation of this correlation at the time.

In Paper II we go in depth on the E2 level, and present a further investigation of its relationship with the Fe content based on several different approaches. The first approach was to look at several new samples in addition to those included in Paper I, particularly also involving measurements on epitaxial samples from both MBE and HVPE synthesis. These new measurements also fit the correlation observed in bulk material, and strengthened our hypothesis of Fe origin for the E2 level. However, based on theoretical treatments, several deep levels from intrinsic origins are also expected in the energy range around E2 [2, 99]. Furthermore, Irmscher et al. speculated the E1 and E3 levels, rather than E2, to be impurity related based on their measurements of Czochralski material [61]. Hence, for a more convincing argument about the origin of E2 we also wanted to check for response to intrinsic defect generation. As discussed in section 3.5.2, the generation of intrinsic defects can be caused by irradiation of samples, and further results of such experiments are detailed below, in sections 5.3 and 5.4. Meanwhile, the irradiation experiments also serve as the second approach to investigate the E2 level in Paper II. The samples were irradiated with H^+, with high acceleration energy to give a flat defect profile in the depletion region of the Schottky contacts on β-Ga$_2$O$_3$, and with different doses to look for possible dose-dependencies in the E2 signature. These irradiation experiments, on both bulk and epitaxial samples, gave no increase in the concentrations of the E2 level, and further strengthened the idea of its extrinsic origin. What we did see from irradiation was the generation of a new level that we labeled E2*. The similarity in our labels reflect the similarity in the electronic properties of these two levels, being so close that they could have been confused, had it not been for their simultaneous presence in the bulk material samples. Figure 10 (a) shows the DLTS data from irradiated and non-irradiated samples of both bulk and HVPE material. In the bulk sample, after irradiation, it is clearly seen the simultaneous presence of the E2 and E2* level. Figure 10 (b) shows the relation between the E2 concentrations in the samples with the Fe impurity concentrations, showing a close to linear behavior.

Finally, the third approach was to investigate theoretically what kind of electronic properties could be expected from Fe in β-Ga$_2$O$_3$. Calculations were carried out by Joel Varley, using his established and well-regarded methods for theoretical calculations in β-Ga$_2$O$_3$ [2, 40, 58]. In these calculations, substitutional Fe on Ga sites (Fe_{Ga}) was considered, whereas the interstitial and O-substituting Fe were left out due to having much higher formation energies. The formation energies for Fe_{Ga} were

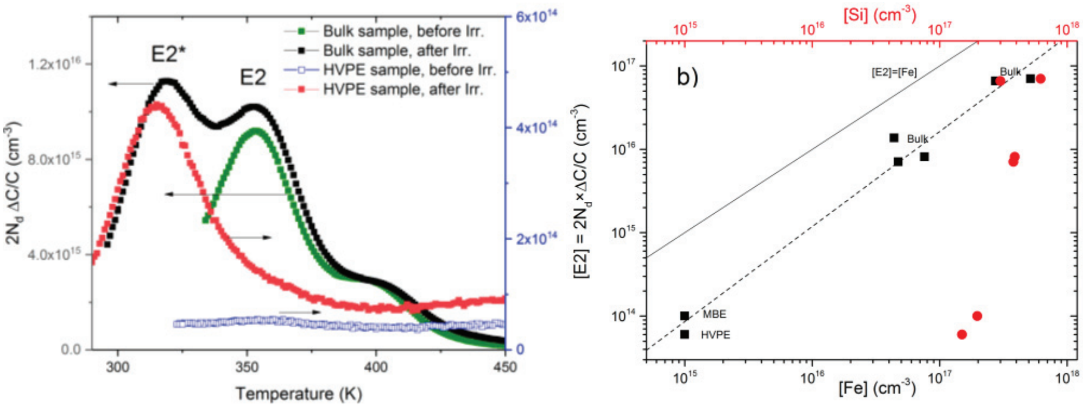

Figure 10 – (a) Shows the generated E2* level in bulk and HVPE material upon irradiation, and the unresponsiveness of the E2 level to the same treatment. (b) Shows the correlation between E2 concentration and Fe impurity concentration in several samples.

found to be favorable across different Fermi levels in the material, and under both Ga- and O-rich conditions, with a slight preference for Fe on the octahedral Ga(II) site. Furthermore, the acceptor transition levels from both substitutions were predicted in energy positions in reasonable agreement with the experimental observation of the E2 level.

Altogether, the correlation of E2 with Fe concentrations, the lack of response in E2 with irradiation, and the prediction of electronic states in this energy range from substitutional Fe provides a strong argument for saying that Fe causes the E2 level. Furthermore, it is possible that this E2 state is the acceptor level that compensates n-type conductivity, as is utilized commercially to produce semi-insulating material [86, 127]. With the generation of the very similar E2* level with irradiation we also provide an explanation for the previous conflicting ideas of the E2 origin that was seen in the literature.

Since Paper II was published, McGlone et al. have observed two levels in the same energy region as E2 and E2* in their MBE films on Fe-doped β-Ga_2O_3 substrates [128]. These measurements were carried out on MESFET's using gate-controlled constant drain-current DLTS, and Fe contamination from the substrate was suspected. Neal et al. have studied Fe doped samples with Hall effect measurements, and find an acceptor level at E_C-0.86 eV [96]. The slightly higher value of the acceptor level seen by Neal et al. is suggested to potentially come from widening of the level due to their considerably higher concentration of around 8×10^{17} cm^{-3}.

5.2 Donors in bulk and epitaxial material

Whereas most samples investigated in our work contain only a single shallow donor level, some MBE samples showed some more variation. The left panel of Figure 11 shows the capacitance at 1 MHz versus temperature from TAS measurements for a bulk sample and two contacts on the MBE samples. In the bulk (010) sample the single freeze-out observed at about 30 K (label A), corresponds to a shallow donor state of about 15 meV. This low temperature freeze-out of the shallow level is common to bulk samples of both surface orientations as well as the HVPE samples. SIMS measurements show that Si is present in all these samples in concentrations higher than the charge carrier concentrations, and correlating better than any other impurity element. Meanwhile, substantial compensation by acceptors is suggested based on the higher Si concentrations than charge carrier concentrations, particularly in bulk samples.

The MBE samples on the other hand reveals three shallow donor states labelled B, C, and D. Since both the MBE samples originate from one wafer, the variation between them corresponds to lateral variation from the synthesis. The residual capacitance observed at low temperatures in the MBE samples is likely related to full depletion of the approximately 2 µm thick films. However, Si is present also in this material, in concentrations that indicate strong compensation also here.

The right panel of Figure 11 shows the Arrhenius plot of the shallow states, and from the linear fits their activation energy is found to be 0.09, 0.12 and 0.18 eV from the conduction band edge, for B, C and D, respectively. These levels have not been identified, but may be related to the ones observed by Neal et al. [96, 98] at E_C-0.11 and 0.13 eV, where one is tentatively attributed to the less energetically favorable Si substitution on octahedral Ga(II). Also Farzana et al.'s [91] observed levels at E_C-0.18 and 0.21 eV, which may be related although their suspicion of this being from a double donor effect of Ge dopants does not fit our defect profile.

5.3 Irradiation-induced charge carrier removal

Having touched upon the effects of irradiation briefly in section 5.1, and the donor properties in section 5.2, we now turn to a discussion of the influence of

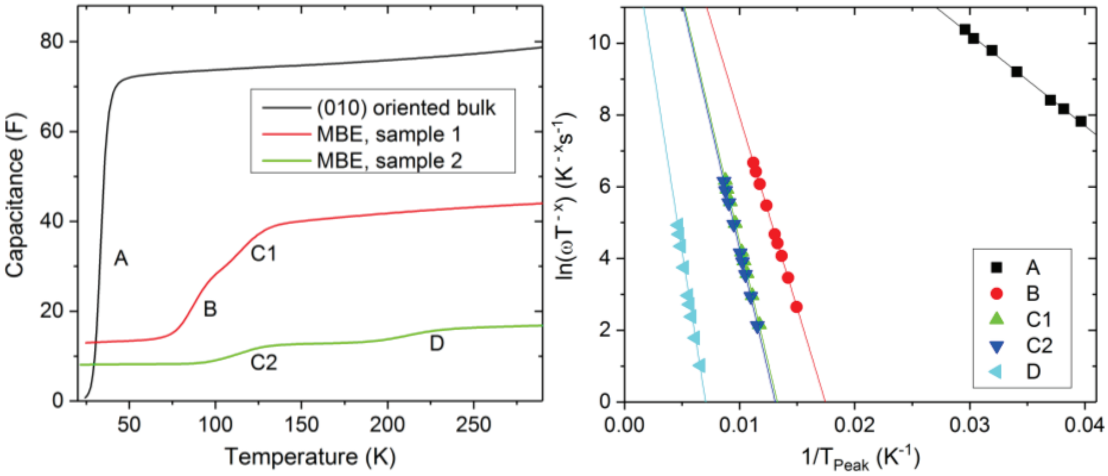

Figure 11 – To the left; TAS measurements represented by 1 MHz capacitance as function of temperature from two MBE samples and one (010) bulk sample. Qualitatively the HVPE and $(\bar{2}01)$ bulk samples are similar to (010) bulk. To the right are Arrhenius plots for the same levels taken from multiple-frequency measurements.

irradiation on the charge carrier concentrations. In Paper III we go in depth on the irradiation induced damage on β-Ga_2O_3 from protons of acceleration energy 0.6 and 1.9 MeV. Additionally, we have also checked for potential influences from the implanted H by using control samples with He irradiation, for which 2 MeV acceleration energy is chosen to give a profile matching 0.6 MeV H^+. Figure 12 shows the damage depth-profiles from the 0.6 MeV H^+ and 2 MeV He^+ irradiation giving similar depth distributions, as determined from SRIM calculations. Notice that due to the different acceleration and mass of our implanted species, the rate of vacancy generation differs. In order to achieve comparable concentrations in the depletion region close to the surface, about seven times higher H^+ doses are required compared to He^+. For the calculations in Figure 12, a displacement energy of 15 eV for both Ga and O were used, in agreement with experience from other semiconductors [14, 129]. Meanwhile, Chaiken et al. [122] used 25 eV for Ga-, and 28 eV for O-displacements, agreeing with default values in the SRIM package [12]. These choices of displacement energies do not affect the projected range; however, in the near-surface region the vacancy generation is inversely proportional to the displacement energy. Hence, this introduces an uncertainty in the prediction of damage concentrations, since exact displacement energies are not known at present.

Doses of H^+ used in Paper III range from 5×10^{9} to 6×10^{14} cm^{-2}, and we observe that for doses at or above 2×10^{13} cm^{-2} complete removal of free charge carriers occurs in the as-irradiated samples. For these high doses, the capacitance seems to be defined solely by the depth of the implantation peak, with no response to applied voltages, thus inhibiting CV and capacitance spectroscopic measurements. As a first observation we note that the degree of dynamic annealing is relatively low in β-Ga_2O_3 compared to what is anticipated from other semiconductors, discussed in section 3.5.2.

After removing charge carriers with irradiation, we did heat treatments and observed a temperature activated process to recover conductivity. The initial measurements showed that the temperature at which this recovery took place depended on both the irradiation dose and whether the sample was bulk or HVPE β-Ga_2O_3. To study the kinetics of the recovery process, we performed continuous measurements of CV at a constant high temperature for long time. This revealed a process having a second order kinetic, or in some samples possibly two simultaneous second order processes. Second order kinetics means that in a reaction where two precursors combine to one product, the rate depends on the concentrations of both precursors. This is in agreement with for example a reaction mechanism involving diffusion and trapping of a mobile defect. As for Paper II, Joel Varley contributed the calculations done in Paper III as well. These calculations accommodate a broad study of a multitude of point defects and their complexes, with regard to deep levels (as will be further discussed in the next section), and stability and migration barriers. The latter, in combination with the experimental observations, allow us to at least speculate on the origins of the charge carrier removal and recovery. We suggest that the origin of the charge carrier depletion is pinning of the Fermi level from the generation of V_{Ga} acceptors and Ga_i and Ga_O donors, at least ~0.5 eV below the CBM. The subsequent recovery is then predicted to be mediated by formation of V_{Ga} complexes and passivation with H or V_O-related defects.

The irradiation with He^+ was done with doses of 1.4×10^{12} to 1.4×10^{13} cm^{-2}, to correspond to the 1×10^{13} to 1×10^{14} cm^{-2} dose range used for H^+ in terms of vacancy concentration. As for H^+, we see a complete charge carrier removal in the He^+ irradiated HVPE samples. Meanwhile, the recovery in the He-irradiated samples seems to require higher temperatures and longer time, as can be seen by comparing Figure 13 (a) and (b). For the sample with 2×10^{13} cm^{-2} dose of H^+, the recovery took place at around 500 K, as can be seen in Paper III, while a similar recovery was seen only at 600 K for the comparable He^+ irradiation dose. The latter was done after only a saturating fractional recovery was achieved at 550 K during 18 hours of CV looping. Consequently, recovery through two different mechanisms may be the case in the He-irradiated samples as discussed above also for H irradiation. Another difference between samples irradiated with the two species is observed in the depth profiles of the recovered charge carriers. Increasing concentrations are seen towards the interface for He-irradiation while the profiles are flatter after recovery from H-irradiation. We

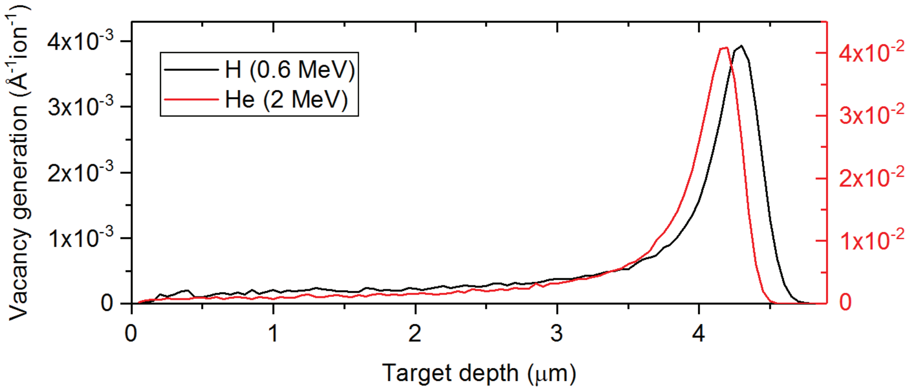

Figure 12 – A comparison of the vacancy generation depth profiles from H^+ and He^+ irradiation in β-Ga_2O_3, using 0.6 and 2 MeV acceleration energy, respectively.

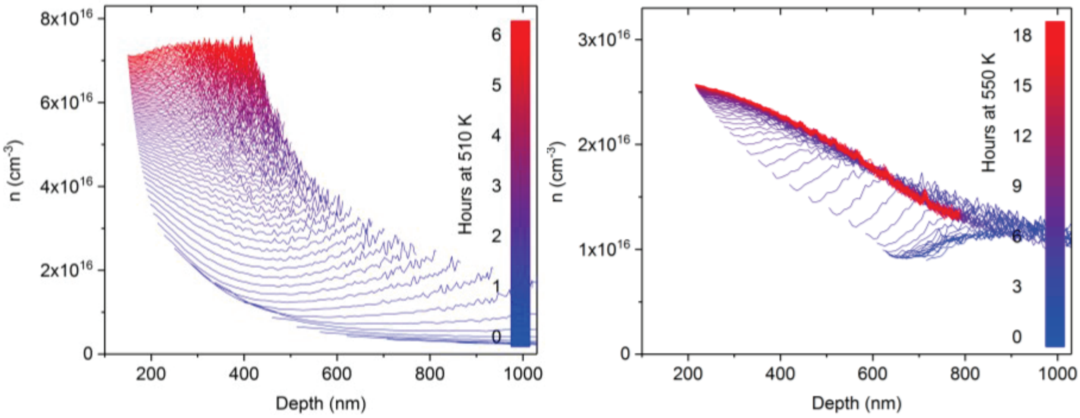

Figure 13 – (a) Recovery of charge carriers in bulk after H$^+$ irradiation, as discussed in paper III, and (b) after He$^+$ irradiation, showing a more pronounced concentration profile. Note also the different time scale.

may speculate on some defect diffusing from the interface playing a more important role in the He-irradiated samples compared to H. Furthermore, the observations of more rapid recovery in H-irradiated samples may be interpreted as H itself playing a role in the recovery, in agreement with the speculations based on the calculations in Paper III.

5.4 Irradiation-induced deep levels

In the charge carrier recovery process described above we recover about 60-100 % of the charge carriers present before irradiation. This means that again the capacitance measurements probe depths close to the Schottky contact interface, far from the implantation peak, allowing also DLTS and TAS measurements. As might be expected from the dynamic behavior of the charge carrier recovery, we also observe some instability in the deep levels during the first DLTS measurements at high temperatures.

In Paper III we describe how we, in all irradiated samples on bulk, MBE, and HVPE material, observe two new deep levels that we label E2* and E4*. The properties of E2* resembles those of E2, while the distinction between the closely spaced levels is being emphasized by the simultaneous presence in bulk material, as discussed above. What was not discussed above or in Paper II, but is elaborated in Paper III, is the generation behavior. In the first measurements after regaining charge carriers, the E2* level can be seen as a shoulder on the E2 level in bulk, or as a new free-standing peak in the epitaxial materials that does not contain the Fe-related E2.

The subsequent measurement cycles to high temperatures are followed by an increase in the E2* concentration. The E2* concentration settles at values that we show to have a close to linear proportionality to the irradiation dose across the different samples. Meanwhile, the E4* with a trap signature similar to E4 is present in the first measurements, whereas its concentration drops below values where it is discernable in the DLTS signal during the ensuing high-temperature measurements.

Through the theoretical approach led by Joel Varley, we also discuss the cause of the two irradiation induced levels in Paper III. The thermally activated formation of a larger E2* concentration following the irradiation suggests two possibilities; either the formation of a defect complex, or an activated rearrangement of a defect.

For the former, we discuss the mobility of H_i impurities at room temperature and how it has been shown that they can interact with intrinsic defects such as vacancies. However, the calculations indicate that these defects give too deep transition levels to be held accountable for our experimental data. On the other hand, the rearrangement between different configurations of V_{Ga} is found possible at the relevant temperatures, and to provide transition levels close to the observed ones. Yet, this explanation is complicated by the relative stabilities of the two levels that do not fit the observations, and that other levels should also be visible in the DLTS measurements. An additional, interpretation is that the E4* level is a Ga_i-derived signal, which through annealing leads to trapping at V_O leading to an increased E2* signal coming from Ga_O. In conclusion, we discussed several possible explanation models for the experimental data, based on the theoretical calculations of an intricate system of intrinsic defects. At the same time the theoretical analysis provides a strong foundation for further work and determination of the origin of experimental data in the future.

5.5 Meta-stability of deep levels in β-Ga_2O_3

After our initial studies of bulk material, the first epitaxial film we studied was from MBE synthesis. In addition to shallow levels differing from those in bulk samples discussed in section 5.2, the MBE sample also showed a peculiar behavior for deep levels. Specifically, we observed generation of three new deep levels, triggered by the DLTS operating conditions of combined applied voltage and high temperature. These three levels are all in the range from 1 to 2 eV below the conduction band minimum, and thus associable with several predictions of intrinsic levels. This lead us to believe that we were able to generate some of these intrinsic deep levels, and detect them in the MBE material since it was otherwise cleaner and with lower charge carrier concentration than bulk samples. However, as we moved on to measure HVPE samples, with comparable charge carrier concentrations and impurity profiles, the hypothesis was challenged when similar deep level generation was not found.

In Paper IV, we collect and present our data on the three levels in MBE that we labeled E3*, E5, and E6. A temperature dependence study was done with DLTS measurements to gradually higher maximum temperature, and we find that for both E3* and E5 temperature above 625 K is necessary for any substantial generation to take place. The temperature limit for E6 generation is more difficult to determine, since high temperature is needed to detect it with DLTS in the first place, but a similar limit is implied. We also determine that only temperature is not sufficient to trigger the generation; on samples with several diodes, there is no generation of the deep levels in others than the measured diode that has the DLTS biasing. It may in fact also be necessary to have the pulsing of the DLTS biasing to generate some of the defects. Using a fixed reverse bias during annealing to the same temperatures as in DLTS provides generation of E5, and to a lesser extent E6, but not E3*. This indicates that the variation in Fermi level and occupancy provided by the pulses may be a driving factor for generation of the defects.

A curiosity with the E3* level is found by the observation that it can be removed again by a heating cycle without bias voltage. Furthermore, DLTS profiling was used to determine the distribution of the E3* level after generation, and we see a strong dependence of the depth profile with the magnitude of the voltage used in the high temperature DLTS. A possible interpretation of this is that the defect that provides the E3* level comes from the interface of the Schottky contact and diffuses in under the measurement conditions. DLTS with different reverse bias voltages also reveal field dependence in the peak position of E3*. A linear relationship between the observed energy level and the square root of the applied electric field indicates Poole-Frenkel lowering of the barrier, in agreement with equation (3.10) and the discussion in section 3.2.3. This implies that the deep level has donor properties, being positively charged when empty.

While E3* is metastable and can be removed, the E5 and E6 levels seem stable after generation. For the latter two, we do not see any trend in energy position as function of measurement voltage, so no conclusions can be drawn on the levels' properties as donors or acceptors. Meanwhile, at least E5 shows profiles similar to E3*, indicating origin from the interface and generation only in the depletion region.

Having initially studied only the MBE epitaxial films, we found the E5 and E6 levels particularly interesting, being very close to the predicted values for the two configurations of gallium vacancies. Early theoretical estimates by Varley et al. placed the V_{Ga} 1.6 and 1.8 eV from the CBM [40], in good agreement with our observations. However, in later theoretical predictions Deák et al. found the vacancies to contribute shallower levels [99]. Considering this along with the lack of similar generation in HVPE or even bulk material, we speculate that the origin of these defects in the MBE material must be of more intricate nature, possibly involving defect complexes. Nonetheless, we cannot completely exclude simpler intrinsic origins and in-diffusion of these during measurement operation; the MBE samples are synthesized with (010) surface orientation, contrary to the (001) of the HVPE samples, and there are indications in the literature of anisotropic diffusion of intrinsic defects in β-Ga_2O_3 favoring diffusion along the b-axis [115].

5.6 Development of capacitance x-ray recording

In Chapter 3, the schematic of the measurement setup in Figure 7 shows how the sample holder intercepts the beamline and is connected to the capacitance meter. In our setup, the capacitance meter is again connected to a computer that collects data and controls measurement parameters, including the temperature control hardware. Further details on both hardware and software of the experimental setup we developed are included in Appendix 7.1. From an engineering point of view, the biggest challenge was to make a sample holder that would allow capacitance measurements along with fluorescence and transmission, while being cooled to cryogenic temperatures. For our visits to the beamline facilities we made two iterations of sample chambers and holders, of which the latter is illustrated in Figure 14. The sample holder is enclosed by the vacuum chamber, which was made with windows on four sides to allow flexibility in achieving both transmission and fluorescence measurements. In order to allow a wide energy range of x-rays, Kapton films were used for the windows, and 0.125 mm thickness was found sufficient to maintain a rough vacuum in the chamber. To the copper cold-finger, a holder was made to give proper angle for fluorescence measurements, while also giving minimal shadowing for the transmission. The samples were mounted on the white alumina card also visible in

Figure 14, with contact pads for backside contacting. A tungsten needle was used to contact selectively the Schottky diodes on the samples, and further details are provided in the Appendix section 7.2.

The first idea we pursued in search for realization of CXAFS was to investigate a simpler material system than the complex Se doped AlGaAs used by Ishii et al. [22, 23, 25]. Since Si is the most studied material available, we selected a known impurity in this system, namely Fe. A weakness with the previous literature on CXAFS is that it only attempts at creating defect related XAFS signal from species that is also present in bulk. This of course is also the claimed advantage of the method, but considering the doubts to the mechanism presented by Bollmann et al. [20, 30, 31], an unambiguous defect signal would be good for further understanding of the recombination mechanism. In p-type Si, interstitial Fe contributes a state about 0.42 eV from the valence band which can be detected by DLTS. Additionally, Fe forms a complex with the dopant B, with electronic state about 0.1 eV from the valence band maximum. Changing between these two states can be achieved by annealing and reverse-bias annealing [130, 131]. In Si samples with a wide range of charge carrier concentrations, Fe was introduced by ion-implantation. Two implantation schemes were used; firstly, with high-dose implantation from the backside followed by annealing to give Fe diffusion and concentration determined by the solubility, and secondly, a lower dose where only rapid thermal annealing was done to remove excess damage. In the latter samples, the peak concentration was expected at approximately 10^{16} cm^{-3} according to SRIM calculations. While this

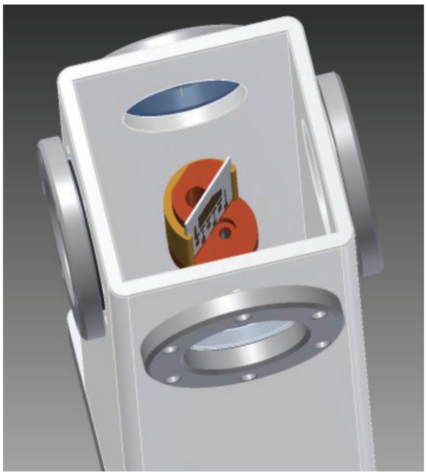

Figure 14 – A schematic representation of our second iteration of a vacuum chamber and sample holder used in the beam line for CXAFS measurements.

concentration is challenging to regular XAFS techniques, we imagined it possible for capacitance-based methods considering the large impact on capacitance measurements when the charge carrier concentrations are comparably lower. At first, as we did observe a change in capacitance upon exciting with x-ray energy below and above the Fe K-shell energy, we thought the foundation for the measurement was there. However, after improvements to both the sample Fe concentration and the experimental setup, it became clear that we were more likely recording background absorption in the Si rather than Fe specific absorption.

5.7 CXAFS of epitaxial β-Ga_2O_3

In a further attempt at recording CXAFS, we investigated the response of K-shell excitations of Ga in β-Ga_2O_3. This was done on an MBE sample where we were able to record the absorption signal carried by both capacitance and fluorescence. These results are reported in Paper V.

Deconvolution of the fluorescence signal on top of the Ga K-shell absorption edge revealed a good fit with literature data, as we observed a fine structure that resembled previous reports on β-Ga_2O_3, as can be seen in Figure 15. Notably, the low-energy part of the absorption step, which is typically called the white line, carries sign of the two different Ga configurations in the material. Figure 15 (a) is adapted from Nishi et al.'s work [132], comparing reference samples where Ga is present purely in tetrahedral- or octahedral configurations with β-Ga_2O_3 samples containing both. Our fluorescence measurements presented in Figure 15 (b) fits well the expectation from the above. In Figure 15 (c) and (d) a comparison is made in a larger energy range, but translated to wavenumber as is customary in XAFS analysis. The data in (c) is a representation of a β-Ga_2O_3 measurement from Choi et al. [133], whereas (d) shows our fluorescence measurements on the MBE sample (a single scan in red and a merge of several in blue).

Looking at the capacitance signal recorded at room temperature, it is immediately evident that it does indeed carry an XAFS signal. This can be seen in the left panel of Figure 16, along with several other capacitance recordings done at different temperatures. At first inspection, the room-temperature capacitance signal seems to reproduce the main features of the fluorescence, with the possible exception of a slight difference in the relative magnitude of the two parts of the white line. At the same time, Figure 16 introduces an important part of the discussion we made in

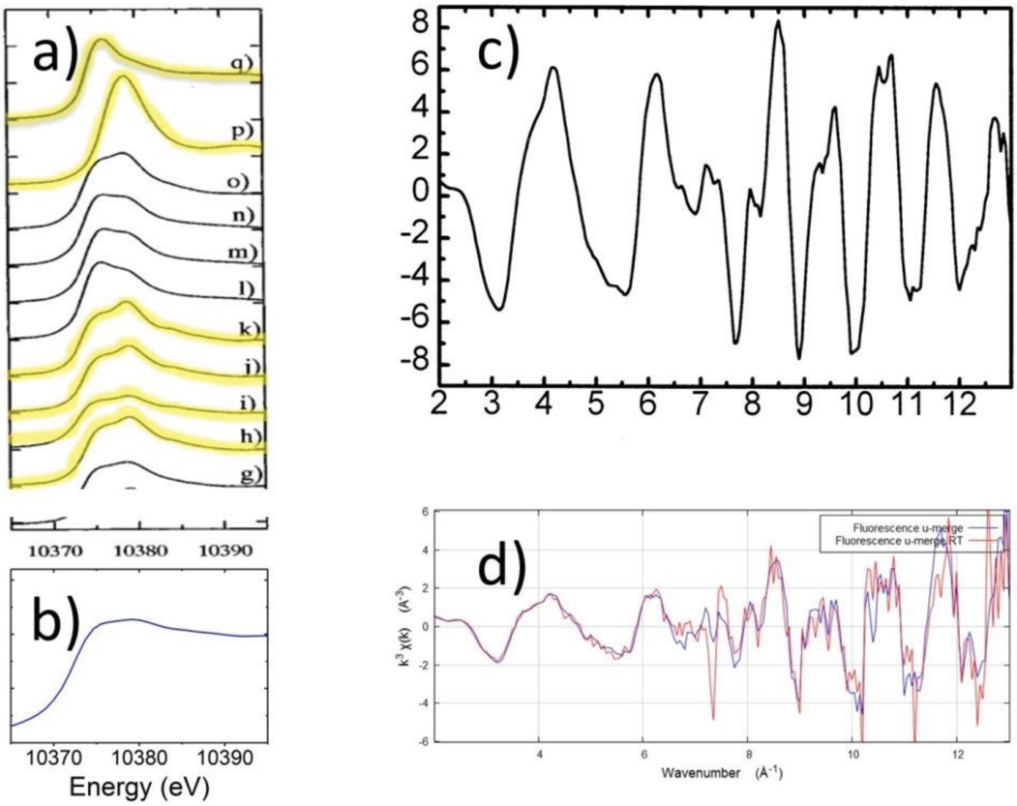

Figure 15 – a) is an adaption from Nishi et al.'s work on deconvolution of the β-Ga$_2$O$_3$ K-edge absorption [132]. In a) the two upper lines represent Ga-references with tetrahedral and octahedral configuration respectively, while the others marked in yellow are samples of β-Ga$_2$O$_3$. In b) is an example of our observations with traditional fluorescence detection. The graph in c) is adapted Choi et al. [133], showing the β-Ga$_2$O$_3$ XAFS extracted from the absorption step, and d) shows similar data from our measurements reproducing the features over a long range of wavenumber (Å^{-1}) translated from energy. In d) the red line is from a single measurement, while the blue is a merge of several measurements for improved signal-to-noise ratio. Figures a and c are adapted from [132] and [133], with permission from American Chemical Society (1998) and AIP Publishing, respectively.

Paper V regarding the differences in observations of CXAFS depending the temperature.

In Paper V, we also observe and discuss that the capacitance signal depends on the energy scan rate applied for the measurements. Altogether, the temperature and scan rate dependencies may point in the direction of some thermally activated process, where statistical considerations determine the occupancy of an inter-bandgap electron state. Ishii et al. also report a similar difference between capacitance and fluorescence in Ref. [22], from which the graph in the right panel of Figure 16 is a reproduction. As mentioned in section 3.7, this difference was interpreted as a sign of different

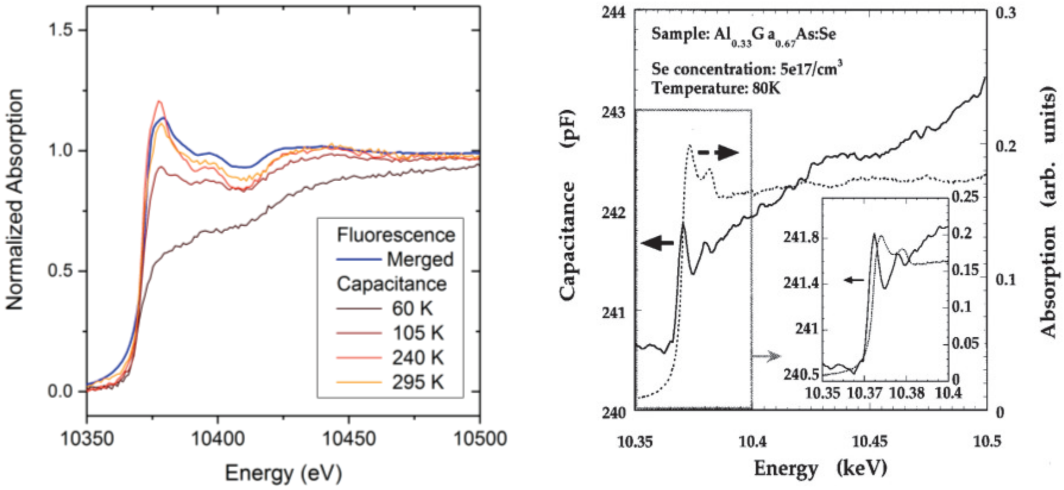

Figure 16 – Left is shown a comparison of our capacitance measurements to the fluorescence that was also discussed in Figure 15. Different temperatures show substantial variations in the steepness of the absorption step. To the right is a figure from Ishii et al.'s capacitance and fluorescence measurements on AlGaAs:Se. Reprinted from [22], with the permission of AIP Publishing

origin of the signals; specifically, a defect related site-selectivity in the capacitance. Meanwhile, based on the presented experimental data, we cannot make a strong argument for relating the capacitance signal to specific defect configurations, as was proposed by Ishii et al. [22, 24, 25]. On the contrary, in Paper V we consider the absolute gain in capacitance across the absorption step to provide an argument against site-selectivity. Specifically, the ~4.5 pF absolute gain is very unlikely to only origin in the λ-region of the depletion region, as it would be difficult to correlate the magnitude of this gain with the x-ray flux (~10^{11} cm^{-2} s^{-1}), the initial donor concentration (~3×10^{16} cm^{-3}), and the depletion depth at zero bias. This is because the ~4.5 pF increase in capacitance would require an additional ~10^{15} cm^{-3} atoms to be ionized in the depletion region. Even if all the Ga atoms were to contribute to the absorption it can be shown that only about 2 % of incident x-rays are absorbed in a 200 nm slab of β-Ga_2O_3. Considering this, the absorption would be insufficient even with contributions from bulk Ga atoms. With the additional assumption that the signal comes selectively from Ga in defect complexes (implying much lower density of atoms that could be ionized), the absorption would be several orders of magnitude too small.

Chapter 6

Conclusions and future work

This thesis summarizes my PhD-research work on characterization of electrically active defects in semiconductors. In particular, the novel semiconducting oxide β-Ga_2O_3 was the focus, and Table II enlist some properties of the deep levels observed in this study.

Due to the novelty of defect studies in β-Ga_2O_3 the development of routines for sample preparation and characterization was necessary. Paper I reports the initial characterization of bulk material, and also selecting metals to achieve optimal Schottky contacts on β-Ga_2O_3. We reported on the IV-characteristics of Schottky contacts and by DLTS found four deep levels labeled E1-E4. In Paper II we expand the study to include several epitaxially grown samples and a theoretical investigation of Fe as a substitutional impurity. We find that Fe is responsible for the dominating deep level E2. Meanwhile, we were also able to introduce the deep level E2* in the material by proton irradiation. Since E2* has very similar properties to E2, we could account for the diverging ideas of E2's origin in previous literature reports.

Paper III extended our investigations of irradiation induced defects further, by describing in detail the charge carrier removal and subsequent recovery by annealing. In Paper III we also detailed the properties of the generated deep levels E2* and E4*, in particular discussing the temperature activated properties following the irradiation. From theoretical calculations, a host of different intrinsic defects and complexes were investigated as candidates for the experimental observations, although further work remains for a strong conclusion in this regard.

In Paper IV we describe interesting generation properties of three new deep levels that we observe in epitaxial material. Specifically, we find E3* to be a metastable donor level that is generated under DLTS operating conditions and removed during annealing. Meanwhile, E5 and E6 are generated with the same premises, but stable afterwards within the parameters tested. For E5 we also show that even the pulsing action of the DLTS biasing plays a role in the generation.

Table II – A summary of the deep levels observed in β-Ga_2O_3 in this work

	E1	E2*	E2	E3	E3*	E4	E4*	E5	E6
$E_C - E_t$ $[eV]$	0.56±0.03	0.75±0.04	0.78±0.04	1.01±0.05	0.92-1.05	1.4±0.15	1.4±0.15	1.5±0.15	1.8±0.2
σ_n $[cm^2]$	$0.3\text{-}5\times10^{-13}$	$3\text{-}7\times10^{-14}$	$0.2\text{-}1.2\times10^{-15}$	$2\times10^{-14}\text{-}1\times10^{-12}$	$0.2\text{-}6\times10^{-13}$	$3\times10^{-15}\text{-}2\times10^{-12}$	$3\times10^{-15}\text{-}2\times10^{-12}$	$10^{-14}\text{-}10^{-11}$	$10^{-12}–10^{-9}$
Observation		Irradiation induced – generation with temperature			Generated by combination of bias and high temperature Metastable		Irradiation induced – removed at relatively low temperature anneal	Generated by combination of bias and high temperature	Generated by combination of bias and high temperature
Origin		Complex with one intrinsic component; likely V_{Ga}	Fe				Intrinsic		

In Paper V we showed that x-ray absorption does influence the diode depletion capacitance, and that the capacitance signal contains information that is comparable to the XAFS signal of traditional recording methods like fluorescence. Meanwhile, we observed a prominent temperature dependence in the CXAFS signal, as well as a dependence on the energy scanning rate. From this we conclude that the CXAFS may contain additional information compared to traditional XAFS, although we find it unlikely to be reporting selectively on defect specific electronic states as has been suggested in previous literature. However, further investigations are necessary to fully comprehend the mechanism of x-ray absorption influence on depletion capacitance.

For β-Ga_2O_3 in general, the identification of deep level defects has only just begun. We believe our work contributes to the new understanding as part of a wave of new literature released over the last couple of years; this wave that will surely continue in the future. Since high radiation resistance has been claimed for β-Ga_2O_3, implying its suitability for operation in harsh environments, it is especially important to confirm the cause of the irradiation damage that we discussed in Paper III. Regarding E2*, a first approach towards more thorough understanding is to look for field dependence in the energy position, similar to what we presented for E3*, to look for its donor behavior. This might preferably be done in HVPE material where the low E2 concentrations allows separation of the E2* signal. Even more important for applications in power electronics is the ability of the material to handle high voltages and power, and consequently operation at high temperatures. The data presented in Paper IV are thus important to reproduce and understand, as the conditions that provoked the generation are relatively modest and may readily affect device performance. Looking at how the recovery of charge carriers in irradiated samples in Paper III occurred at different temperatures for different sample types, a study to even higher temperatures with DLTS conditions might help to understand the generation of E3*, E5, and E6 in other samples too.

The influence of H, both in untreated samples and in the irradiated samples is also still an open question, both regarding donor properties and interaction with other defects. While we did not find H to affect the deep levels generated by irradiation, we saw signs of different behavior in the recovery of charge carriers when irradiating with He. Hence, further work with He irradiation, and comparison to H-irradiated samples, may be an important angle to figure out the influence of H. In terms of irradiation induced effects, the results from in-situ measurements of samples being irradiated also holds a great promise for exciting discoveries. This, in particular holds for the rate of charge carrier removal and to enable the study of E2* and E4* levels without the annealing step to recover charge carriers.

Bibliography

[1] Pearton, S.J., J. Yang, P.H. CaryIV, F. Ren, J. Kim, M.J. Tadjer, and M.A. Mastro, Applied Physics Reviews, 2018. **5**(1): p. 011301.

[2] Varley, J.B., J.R. Weber, A. Janotti, and C.G. Van de Walle, Applied Physics Letters, 2010. **97**(14): p. 142106.

[3] Blood, P. and J.W. Orton. 1992: Academic Press.

[4] Lang, D.V., Journal of Applied Physics, 1974. **45**(7): p. 3023-3032.

[5] 2001Åberg, D., *Capacitance Spectroscopy of Point Defects in Silicon and Silicon Carbide*, in *Mikroelektronik och informationsteknik*. 2001, Kungliga Tekniska Högskolan.

[6] Frenkel, J., Physical Review, 1938. **54**(8): p. 647-648.

[7] Pautrat, J.L., B. Katircioglu, N. Magnea, D. Bensahel, J.C. Pfister, and L. Revoil, Solid-State Electronics, 1980. **23**(11): p. 1159-1169.

[8] Losee, D.L., Journal of Applied Physics, 1975. **46**(5): p. 2204-2214.

[9] 2009Schifano, R., *Schottky contacts and electrical characterization of n-type hydrothermally grown ZnO*, in *Department of Physics/Center for Materials Science and Nanotechnology*. 2009, University of Oslo.

[10] Tang, C.K., L. Vines, B.G. Svensson, and E.V. Monakhov, Physica status solidi. C, Current topics in solid state physics, 2012. **9**(10-11): p. 1992-1995.

[11] Ziegler, J.F. and J.P. Biersack, in *Treatise on Heavy-Ion Science: Volume 6: Astrophysics, Chemistry, and Condensed Matter*, D.A. Bromley, Editor. 1985, Springer US: Boston, MA. p. 93-129.

[12] Ziegler, J.F., M.D. Ziegler, and J.P. Biersack, Nuclear Instruments and Methods in Physics Research Section B: Beam Interactions with Materials and Atoms, 2010. **268**(11): p. 1818-1823.

[13] Hallén, A. and N. Keskitalo, Nuclear Instruments and Methods in Physics Research Section B: Beam Interactions with Materials and Atoms, 2002. **186**(1): p. 344-348.

[14] Svensson, B.G., C. Jagadish, A. Hallén, and J. Lalita, Physical Review B, 1997. **55**(16): p. 10498-10507.

[15] Williams, J.S. and J.M. Poate. 2014: Elsevier Science.

[16] Als-Nielsen, J. and D. McMorrow. 2011: Wiley.

[17] Newville, M., obtained from xafs.org 14.10.2014, 2004.

[18] M. El-Shemi, A. Vol. 28. 2004.

[19] Boscherini, F., in *X-Ray Absorption Spectroscopy of Semiconductors*, S.C. Schnohr and C.M. Ridgway, Editors. 2015, Springer Berlin Heidelberg: Berlin, Heidelberg. p. 77-97.

[20] Bollmann, J., S. Knack, J. Weber, V. Koteski, H.E. Mahnke, and E. Welter, Physical Review B, 2003. **68**(12): p. 125206.

[21] Takeda, Y., H. Ofuchi, H. Kyouzu, R. Takahashi, and M. Tabuchi, Journal of Synchrotron Radiation, 2005. **12**(4): p. 494-498.

[22] Ishii, M., Y. Yoshino, K.-i. Takarabe, and O. Shimomura, Applied Physics Letters, 1999. **74**(18): p. 2672.

[23] Ishii, M., Y. Yoshino, K.-i. Takarabe, and O. Shimomura, Physica B: Condensed Matter, 1999. **273**: p. 774-777.

[24] Ishii, M., Y. Yoshino, K.-i. Takarabe, and O. Shimomura, Journal of Applied Physics, 2000. **88**(7): p. 3962-3967.

[25] Ishii, M., Physical Review B, 2002. **65**(8): p. 085310.

[26] Boehme, R.F., G.S.C. III, W. Weber, and T. Jackson, Journal of Applied Physics, 1985. **58**(2): p. 811-815.

[27] Hu, T.D., Y.N. Xie, S. Qiao, Y. Hai, Y.L. Jin, and D.C. Xian, Physical Review B, 1994. **50**(4): p. 2216-2220.

[28] Ishii, M., Japanese Journal of Applied Physics, 2002. **41**(6S): p. 4415.

[29] Fujioka, H., T. Sekiya, Y. Kuzuoka, M. Oshima, H. Usuda, N. Hirashita, and M. Niwa, Applied Physics Letters, 2004. **85**(3): p. 413.

[30] Bollmann, J., S. Knack, J. Weber, V. Koteski, H.E. Mahnke, and E. Welter, Physica Scripta, 2005. **2005**(T115): p. 188.

[31] Weber, J., J. Bollmann, S. Knack, V. Kotestki, H.E. Mahnke, and E. Welter, in *Gettering and Defect Engineering in Semiconductor Technology*, H. Richter and M. Kittler, Editors. 2004, Trans Tech Publications Ltd: Zurich-Uetikon. p. 483-488.

[32] Konovalov, I., L. Makhova, and R. Mitdank, Physica B-Condensed Matter, 2007. **401**: p. 654-657.

[33] Konovalov, I., L. Makhova, D. Wett, K.H. Hallmeier, R. Szargan, and R. Mitdank, Applied Physics Letters, 2006. **88**(22): p. 222106.

[34] Bazlov, N., O. Vyvenko, A. Bondarenko, M. Trushin, A. Novikov, A. Vinogradov, M. Brzhezinskaya, and R. Ovsyannikov, Superlattices and Microstructures, 2009. **45**(4–5): p. 190-199.

[35] Roy, R., V.G. Hill, and E.F. Osborn, Journal of the American Chemical Society, 1952. **74**(3): p. 719-722.

[36] Chase, A.O., Journal of the American Ceramic Society, 1964. **47**(9): p. 470-470.

[37] Tippins, H.H., Physical Review, 1965. **140**(1A): p. A316-A319.

[38] Fleischer, M. and H. Meixner, Sensors and Actuators B-Chemical, 1991. **5**(1-4): p. 115-119.

[39] Baldini, M., Z. Galazka, and G. Wagner, Materials Science in Semiconductor Processing, 2018. **78**: p. 132-146.

[40] Varley, J.B., H. Peelaers, A. Janotti, and C.G.V.d. Walle, Journal of Physics: Condensed Matter, 2011. **23**(33): p. 334212.

[41] Momma, K. and F. Izumi, J. Appl. Crystallogr, 2011. **44**( ): p. 1272-1276.

[42] Janowitz, C., V. Scherer, M. Mohamed, A. Krapf, H. Dwelk, R. Manzke, Z. Galazka, R. Uecker, K. Irmscher, R. Fornari, M. Michling, D. Schmeißer, J.R. Weber, J.B. Varley, and C.G.V.d. Walle, New Journal of Physics, 2011. **13**(8): p. 085014.

[43] Mock, A., R. Korlacki, C. Briley, V. Darakchieva, B. Monemar, Y. Kumagai, K. Goto, M. Higashiwaki, and M. Schubert, Physical Review B, 2017. **96**(24): p. 245205.

[44] Peelaers, H. and C.G. Van de Walle, physica status solidi (b), 2015. **252**(4): p. 828-832.

[45] Knight, S., A. Mock, R. Korlacki, V. Darakchieva, B. Monemar, Y. Kumagai, K. Goto, M. Higashiwaki, and M. Schubert, Applied Physics Letters, 2018. **112**(1): p. 012103.

[46] Oishi, T., Y. Koga, K. Harada, and M. Kasu, Applied Physics Express, 2015. **8**(3): p. 031101.

[47] Kang, Y., K. Krishnaswamy, H. Peelaers, and C.G. Van de Walle, Journal of Physics: Condensed Matter, 2017. **29**(23): p. 234001.

[48] Sasaki, K., A. Kuramata, T. Masui, E.G. Víllora, K. Shimamura, and S. Yamakoshi, Applied Physics Express, 2012. **5**(3): p. 035502.

[49] Higashiwaki, M. and G.H. Jessen, Applied Physics Letters, 2018. **112**(6): p. 060401.

[50] Hudgins, J.L., G.S. Simin, E. Santi, and M.A. Khan, IEEE Transactions on Power Electronics, 2003. **18**(3): p. 907-914.

[51] Tsao, J.Y., S. Chowdhury, M.A. Hollis, D. Jena, N.M. Johnson, K.A. Jones, R.J. Kaplar, S. Rajan, C.G. Van de Walle, E. Bellotti, C.L. Chua, R. Collazo, M.E. Coltrin, J.A. Cooper, K.R. Evans, S. Graham, T.A. Grotjohn, E.R. Heller, M. Higashiwaki, M.S. Islam, P.W. Juodawlkis, M.A. Khan, A.D. Koehler, J.H. Leach, U.K. Mishra, R.J. Nemanich, R.C.N. Pilawa-Podgurski, J.B. Shealy, Z. Sitar, M.J. Tadjer, A.F. Witulski, M. Wraback, and J.A. Simmons, Advanced Electronic Materials, 2018. **4**(1): p. 1600501.

[52] Handwerg, M., R. Mitdank, Z. Galazka, and S.F. Fischer, Semiconductor Science and Technology, 2016. **31**(12): p. 125006.

[53] The World Bank. *Electric power transmission and distribution losses (% of output)*. 12.07.2018]; Available from: https://data.worldbank.org/indicator/EG.ELC.LOSS.ZS.

[54] Baliga, B.J., Journal of Applied Physics, 1982. **53**(3): p. 1759-1764.

[55] Baliga, B.J., in *Fundamentals of Power Semiconductor Devices*. 2008, Springer US: Boston, MA. p. 1-22.

[56] Buttay, C., D. Planson, B. Allard, D. Bergogne, P. Bevilacqua, C. Joubert, M. Lazar, C. Martin, H. Morel, D. Tournier, and C. Raynaud, Materials Science and Engineering: B, 2011. **176**(4): p. 283-288.

[57] Higashiwaki, M., K. Sasaki, A. Kuramata, T. Masui, and S. Yamakoshi, Applied Physics Letters, 2012. **100**(1): p. 013504.

[58] Varley, J.B., A. Janotti, C. Franchini, and C.G. Van de Walle, Physical Review B, 2012. **85**(8): p. 081109.

[59] Ghosh, K. and U. Singisetti, Journal of Applied Physics, 2017. **122**(3): p. 035702.

[60] Johnson, E.O., Rca Review, 1965. **26**(2): p. 163-&.

[61] Irmscher, K., Z. Galazka, M. Pietsch, R. Uecker, and R. Fornari, Journal of Applied Physics, 2011. **110**(6): p. 063720.

[62] Suzuki, R., S. Nakagomi, Y. Kokubun, N. Arai, and S. Ohira, Applied Physics Letters, 2009. **94**(22): p. 222102.

[63] Sasaki, K., M. Higashiwaki, A. Kuramata, T. Masui, and S. Yamakoshi, Electron Device Letters, IEEE, 2013. **34**(4): p. 493-495.

[64] Ingebrigtsen, M.E., L. Vines, G. Alfieri, A. Mihaila, U. Badstübner, B.G. Svensson, and A. Kuznetsov, Materials Science Forum, 2017. **897**: p. 755-758.

[65] Yang, J., S. Ahn, F. Ren, S.J. Pearton, S. Jang, J. Kim, and A. Kuramata, Applied Physics Letters, 2017. **110**(19): p. 192101.

[66] Fu, H., H. Chen, X. Huang, I. Baranowski, J. Montes, T. Yang, and Y. Zhao, IEEE Transactions on Electron Devices, 2018. **65**(8): p. 3507-3513.

[67] He, Q., W. Mu, H. Dong, S. Long, Z. Jia, H. Lv, Q. Liu, M. Tang, X. Tao, and M. Liu, Applied Physics Letters, 2017. **110**(9): p. 093503.

[68] Konishi, K., K. Goto, H. Murakami, Y. Kumagai, A. Kuramata, S. Yamakoshi, and M. Higashiwaki, Applied Physics Letters, 2017. **110**(10): p. 103506.

[69] Green, A.J., K.D. Chabak, E.R. Heller, R.C. Fitch, M. Baldini, A. Fiedler, K. Irmscher, G. Wagner, Z. Galazka, S.E. Tetlak, A. Crespo, K. Leedy, and G.H. Jessen, IEEE Electron Device Letters, 2016. **37**(7): p. 902-905.

[70] Chabak, K.D., N. Moser, A.J. Green, D.E.W. Jr., S.E. Tetlak, E. Heller, A. Crespo, R. Fitch, J.P. McCandless, K. Leedy, M. Baldini, G. Wagner, Z. Galazka, X. Li, and G. Jessen, Applied Physics Letters, 2016. **109**(21): p. 213501.

[71] Higashiwaki, M., K. Sasaki, A. Kuramata, T. Masui, and S. Yamakoshi, physica status solidi (a), 2014. **211**(1): p. 21-26.

[72] Higashiwaki, M., K. Sasaki, H. Murakami, Y. Kumagai, A. Koukitu, A. Kuramata, T. Masui, and S. Yamakoshi, Semiconductor Science and Technology, 2016. **31**(3): p. 034001.

[73] Wong, M.H., K. Sasaki, A. Kuramata, S. Yamakoshi, and M. Higashiwaki, IEEE Electron Device Letters, 2016. **37**(2): p. 212-215.

[74] Green, A.J., K.D. Chabak, M. Baldini, N. Moser, R. Gilbert, R.C. Fitch, G. Wagner, Z. Galazka, J. Mccandless, A. Crespo, K. Leedy, and G.H. Jessen, IEEE Electron Device Letters, 2017. **38**(6): p. 790-793.

[75] Oh, S., M.A. Mastro, M.J. Tadjer, and J. Kim, ECS Journal of Solid State Science and Technology, 2017. **6**(8): p. Q79-Q83.

[76] Stevenson, R. *Gallium Oxide: Power Electronics' Cool New Flavor*. 18.07.2018]; Available from: https://spectrum.ieee.org/semiconductors/materials/gallium-oxide-power-electronics-cool-new-flavor.

[77] Lorenz, M.R., J.F. Woods, and R.J. Gambino, Journal of Physics and Chemistry of Solids, 1967. **28**(3): p. 403-&.

[78] Víllora, E.G., K. Shimamura, Y. Yoshikawa, K. Aoki, and N. Ichinose, Journal of Crystal Growth, 2004. **270**(3–4): p. 420-426.

[79] Hoshikawa, K., E. Ohba, T. Kobayashi, J. Yanagisawa, C. Miyagawa, and Y. Nakamura, Journal of Crystal Growth, 2016. **447**: p. 36-41.

[80] Galazka, Z., K. Irmscher, R. Uecker, R. Bertram, M. Pietsch, A. Kwasniewski, M. Naumann, T. Schulz, R. Schewski, D. Klimm, and M. Bickermann, Journal of Crystal Growth, 2014. **404**: p. 184-191.

[81] Galazka, Z., R. Uecker, K. Irmscher, M. Albrecht, D. Klimm, M. Pietsch, M. Brützam, R. Bertram, S. Ganschow, and R. Fornari, Crystal Research and Technology, 2010. **45**(12): p. 1229-1236.

[82] Kuramata, A., K. Koshi, S. Watanabe, Y. Yamaoka, T. Masui, and S. Yamakoshi, Japanese Journal of Applied Physics, 2016. **55**(12): p. 1202A2.

[83] Mastro, M.A., A. Kuramata, J. Calkins, J. Kim, F. Ren, and S.J. Pearton, ECS Journal of Solid State Science and Technology, 2017. **6**(5): p. P356-P359.

[84] McCluskey, M.D., M.C. Tarun, and S.T. Teklemichael, Journal of Materials Research, 2012. **27**(17): p. 2190-2198.

[85] King, P.D.C., I. McKenzie, and T.D. Veal, Applied Physics Letters, 2010. **96**(6): p. 062110.

[86] Novel Crystal Technology. 04.08.2018]; Available from: https://www.novelcrystal.co.jp/eng/.

[87] Víllora, E.G., K. Shimamura, Y. Yoshikawa, T. Ujiie, and K. Aoki, Applied Physics Letters, 2008. **92**(20): p. 202120.

[88] Suzuki, N., S. Ohira, M. Tanaka, T. Sugawara, K. Nakajima, and T. Shishido, physica status solidi (c), 2007. **4**(7): p. 2310-2313.

[89] Ueda, N., H. Hosono, R. Waseda, and H. Kawazoe, Applied Physics Letters, 1997. **70**(26): p. 3561-3563.

[90] Baldini, M., M. Albrecht, A. Fiedler, K. Irmscher, R. Schewski, and G. Wagner, ECS Journal of Solid State Science and Technology, 2017. **6**(2): p. Q3040-Q3044.

[91] Farzana, E., E. Ahmadi, J.S. Speck, A.R. Arehart, and S.A. Ringel, Journal of Applied Physics, 2018. **123**(16): p. 161410.

[92] Ahmadi, E., O.S. Koksaldi, S.W. Kaun, Y. Oshima, D.B. Short, U.K. Mishra, and J.S. Speck, Applied Physics Express, 2017. **10**(4): p. 041102.

[93] Peelaers, H. and C.G. Van de Walle, Physical Review B, 2016. **94**(19): p. 195203.

[94] Higashiwaki, M., K. Sasaki, T. Kamimura, M. Hoi Wong, D. Krishnamurthy, A. Kuramata, T. Masui, and S. Yamakoshi, Applied Physics Letters, 2013. **103**(12): p. 123511.

[95] Guo, D., P. Li, Z. Wu, W. Cui, X. Zhao, M. Lei, L. Li, and W. Tang, Scientific Reports, 2016. **6**: p. 24190.

[96] Neal, A.T., S. Mou, S. Rafique, H. Zhao, E. Ahmadi, J.S. Speck, K.T. Stevens, J.D. Blevins, D.B. Thomson, N. Moser, K.D. Chabak, and G.H. Jessen, Applied Physics Letters, 2018. **113**(6): p. 062101.

[97] Son, N.T., K. Goto, K. Nomura, Q.T. Thieu, R. Togashi, H. Murakami, Y. Kumagai, A. Kuramata, M. Higashiwaki, A. Koukitu, S. Yamakoshi, B. Monemar, and E. Janzén, Journal of Applied Physics, 2016. **120**(23): p. 235703.

[98] Neal, A.T., S. Mou, R. Lopez, J.V. Li, D.B. Thomson, K.D. Chabak, and G.H. Jessen, Scientific Reports, 2017. **7**(1): p. 13218.

[99] Deák, P., Q. Duy Ho, F. Seemann, B. Aradi, M. Lorke, and T. Frauenheim, Physical Review B, 2017. **95**(7): p. 075208.

[100] Korhonen, E., F. Tuomisto, D. Gogova, G. Wagner, M. Baldini, Z. Galazka, R. Schewski, and M. Albrecht, Applied Physics Letters, 2015. **106**(24): p. 242103.

[101] Iwaya, K., R. Shimizu, H. Aida, T. Hashizume, and T. Hitosugi, Applied Physics Letters, 2011. **98**(14): p. 142116.

[102] Liu, L.L., M.K. Li, D.Q. Yu, J. Zhang, H. Zhang, C. Qian, and Z. Yang, Applied Physics A, 2010. **98**(4): p. 831-835.

[103] Feng, Q., J. Liu, Y. Yang, D. Pan, Y. Xing, X. Shi, X. Xia, and H. Liang, Journal of Alloys and Compounds, 2016. **687**: p. 964-968.

[104] Dong, L., R. Jia, C. Li, B. Xin, and Y. Zhang, Journal of Alloys and Compounds, 2017. **712**: p. 379-385.

[105] Kyrtsos, A., M. Matsubara, and E. Bellotti, Applied Physics Letters, 2018. **112**(3): p. 032108.

[106] Chikoidze, E., A. Fellous, A. Perez-Tomas, G. Sauthier, T. Tchelidze, C. Ton-That, T.T. Huynh, M. Phillips, S. Russell, M. Jennings, B. Berini, F. Jomard, and Y. Dumont, Materials Today Physics, 2017. **3**: p. 118-126.

[107] Yakimov, E.B., A.Y. Polyakov, N.B. Smirnov, I.V. Shchemerov, J. Yang, F. Ren, G. Yang, J. Kim, and S.J. Pearton, Journal of Applied Physics, 2018. **123**(18): p. 185704.

[108] Arehart, A.R., A. Sasikumar, S. Rajan, G.D. Via, B. Poling, B. Winningham, E.R. Heller, D. Brown, Y. Pei, F. Recht, U.K. Mishra, and S.A. Ringel, Solid-State Electronics, 2013. **80**: p. 19-22.

[109] Armstrong, A.M., A.A. Allerman, A.G. Baca, and C.A. Sanchez, Semiconductor Science and Technology, 2013. **28**(7): p. 074020.

[110] Zhang, Z., E. Farzana, A.R. Arehart, and S.A. Ringel, Applied Physics Letters, 2016. **108**(5): p. 052105.

[111] Chantre, A., G. Vincent, and D. Bois, Physical Review B, 1981. **23**(10): p. 5335-5359.

[112] Armstrong, A.M., M.H. Crawford, A. Jayawardena, A. Ahyi, and S. Dhar, Journal of Applied Physics, 2016. **119**(10): p. 103102.

[113] Kananen, B.E., L.E. Halliburton, K.T. Stevens, G.K. Foundos, and N.C. Giles, Applied Physics Letters, 2017. **110**(20): p. 202104.

[114] Deák, P., Physica B: Condensed Matter, 2018. **535**: p. 35-43.

[115] Kyrtsos, A., M. Matsubara, and E. Bellotti, Physical Review B, 2017. **95**(24): p. 245202.

[116] Blanco, M.A., M.B. Sahariah, H. Jiang, A. Costales, and R. Pandey, Physical Review B, 2005. **72**(18): p. 184103.

[117] Zacherle, T., P.C. Schmidt, and M. Martin, Physical Review B, 2013. **87**(23): p. 235206.

[118] Polyakov, A.Y., N.B. Smirnov, I.V. Shchemerov, E.B. Yakimov, J. Yang, F. Ren, G. Yang, J. Kim, A. Kuramata, and S.J. Pearton, Applied Physics Letters, 2018. **112**(3): p. 032107.

[119] Weiser, P., M. Stavola, W.B. Fowler, Y. Qin, and S. Pearton, Applied Physics Letters, 2018. **112**(23): p. 232104.

[120] Lee, J., E. Flitsiyan, L. Chernyak, J. Yang, F. Ren, S.J. Pearton, B. Meyler, and Y.J. Salzman, Applied Physics Letters, 2018. **112**(8): p. 082104.

[121] Yang, J. and F. Ren, Journal of Vacuum Science & Technology B, 2017. **35**(3): p. 031208.

[122] Chaiken, M.F. and T.E. Blue, IEEE Transactions on Nuclear Science, 2018. **65**(5): p. 1147-1152.

[123] Wong, M.H., A. Takeyama, T. Makino, T. Ohshima, K. Sasaki, A. Kuramata, S. Yamakoshi, and M. Higashiwaki, Applied Physics Letters, 2018. **112**(2): p. 023503.

[124] Yang, J., Z. Chen, F. Ren, S.J. Pearton, G. Yang, J. Kim, J. Lee, E. Flitsiyan, L. Chernyak, and A. Kuramata, Journal of Vacuum Science & Technology B, 2018. **36**(1): p. 011206.

[125] Yang, G., S. Jang, F. Ren, S.J. Pearton, and J. Kim, ACS Applied Materials & Interfaces, 2017. **9**(46): p. 40471-40476.

[126] Arehart, A.R., E. Farzana, T.E. Blue, and S.A. Ringel. *Impact of Neutron Irradiation on Electronic Defects in β-*Ga_2O_3. in *International Workshop on* Ga_2O_3 *and Related Materials*. 2017. Parma, Italy.

[127] Wong, M.H., K. Sasaki, A. Kuramata, S. Yamakoshi, and M. Higashiwaki, Applied Physics Letters, 2015. **106**(3): p. 032105.

[128] Mcglone, J.F.n., Z. Xia, Y. Zhang, C. Joishi, S. Lodha, S. Rajan, S.A.n. Ringel, and A.R.n. Arehart, IEEE Electron Device Letters, 2018. **39**(7).

[129] Loferski, J.J. and P. Rappaport, Physical Review, 1958. **111**(2): p. 432-439.

[130] Istratov, A.A., H. Hieslmair, and E.R. Weber, Applied Physics A, 1999. **69**(1): p. 13-44.

[131] 2012Tang, C.K., *Electrical studies of Fe-related defect complexes in silicon*. 2012, UiO.

[132] Nishi, K., K.-i. Shimizu, M. Takamatsu, H. Yoshida, A. Satsuma, T. Tanaka, S. Yoshida, and T. Hattori, The Journal of Physical Chemistry B, 1998. **102**(50): p. 10190-10195.

[133] Choi, Y.G., J. Heo, and V.A. Chernov, Journal of Non-Crystalline Solids, 1997. **221**(2–3): p. 199-207.

Chapter 7

Appendices

7.1 Details of the CXAFS recording setup

Due to the logistics of irradiation safety precautions this whole setup had to be locked into a lead-clad beamline hutch during operation. On-site, a remote desktop connection to the controlling computer was used to access the measurement controls relating to capacitance. Beamline control infrastructure was already set up to be operated from outside the hutch. This existing setup was used to control the transmission measurements, where detection takes place in ion-chambers, primarily to aid for sample alignment. Meanwhile, fluorescence detection was recorded

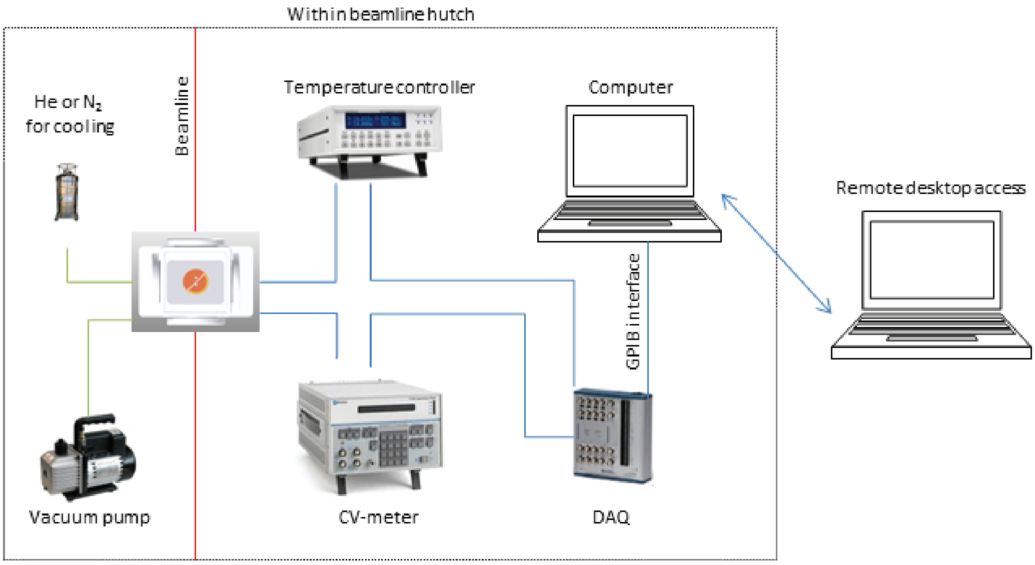
Within beamline hutch
He or N_2 for cooling
Beamline
Temperature controller
Computer
Remote desktop access
GPIB interface
Vacuum pump
CV-meter
DAQ

Figure 17 – A schematic representation of the experimental setup used in the beamline to enable recording of the capacitance response to x-ray irradiation.

simultaneous with (and for comparison with) the capacitance measurements, using a 13-element germanium detector.

A detailed schematic of the capacitance-related measurement setup is shown in Figure 17. Here the computer within the beamline hutch was running a LabView program to control the setup. This code allowed us to set the bias voltage on the diode, the capacitance measurement range, the measurement intervals, as well as record the received data from the measurements. Data acquisition was done with a USB-6341 DAQ from National Instruments with BNC connectors to talk to the capacitance meters. In the first iteration of our setup, with results described in section **Error! Reference source not found.**, we used a HP 4280A capacitance meter, whereas this was changed for a Boonton 7200 for higher time resolution in the later experiments. Temperature control was achieved with a Lakeshore 330, controlling a 48 Ω resistive heater on the sample holder. Below follows a more detailed description of the sample holders and cooling setups.

7.2 Cryostats and sample holders for CXAFS

In both our versions of the sample holder the temperature controller and heater element described above acts to counter balance the cooling from a N_2 or He cooling arrangements to achieve a constant temperature of our choice. Along with good temperature control at the sample, electrical connectivity and x-ray access was common requirements of the sample holders.

7.2.1 Version 1: Nitrogen cryostream

The first iteration of the sample holder made use of a N_2-cryostream chamber that were already available in the beamline system, but with our own design of the sample holder for electrical connectivity. In the left panel of Figure 18 the chamber is pictured, showing also the N_2-tubing coming down from the top, and the beamline coming in from the right. The housing is open for mounting samples in this picture. The sample holder consisted of a plate mounted with a needle lever to pinch the sample, and assure electrical connectivity. In the right panel of Figure 18 a sample is shown connected with the needle, as pictured through a mounted Kapton window. Kapton is the brand name of a polyimide film by DuPont known for good mechanical properties and transparency to x-rays in a wide energy range. With this setup we were

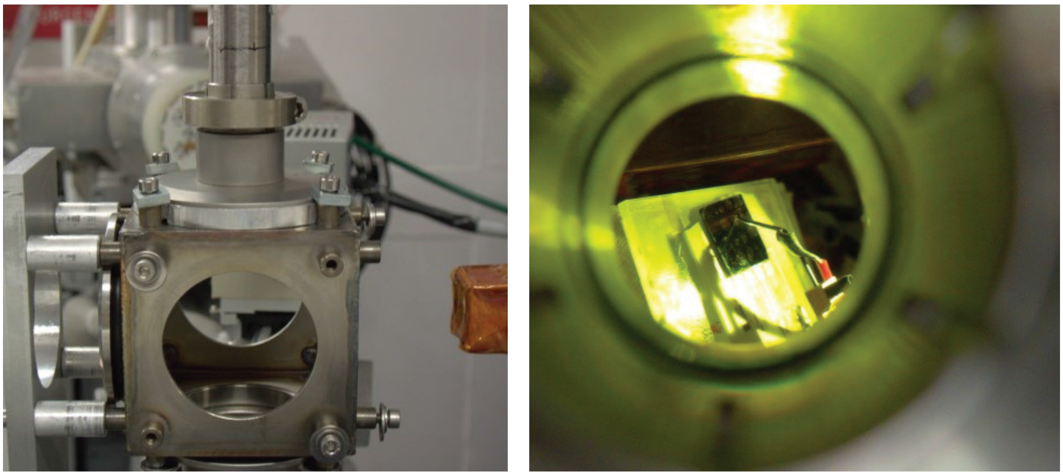

Figure 18 – (left) Showing the chamber with N_2 supply from the top and beamline incoming from the right. In the right panel the sample is mounted in the chamber behind a Kapton window.

able to measure the samples at down to 90 K. Meanwhile, since the N_2 flow was directed directly at the sample, and with somewhat flimsy contacts, the electrical connectivity was less than ideal. In addition, N_2 flow without vacuum pumping of the chamber resulted in icing on the sample and wires, also posing a challenge for good electrical measurements.

7.2.2 Version 2: Helium vacuum system

To avoid the icing problem, we decided to make a vacuum chamber for the next measurements. For this, a refined version of the sample holder was also developed to improve the stability and signal from the electrical connectivity. This was done with basis in a cryostat from Oxford instruments that had served its purpose in a PL setup. We utilized the cold finger and He connectivity, and designed a new outer chamber with Kapton windows on four sides as was mentioned in chapter 5.6 and Figure 14. The existing parts also had a built-in heater and temperature sensor that made the temperature control easier. The finished sample chamber and the cold finger with connectivity are shown in the left panel of Figure 19. In addition to the new outer housing with x-ray windows we made new electrical connectivity for the capacitance measurements, with shielded cables and BNC fittings through the vacuum chamber. On the end of the cold finger the purpose-built sample holder can be seen. The design of the sample holder can also be seen in the drawing in the right panel of Figure 19. Here the incident x-ray beam will come from slightly below the angle of view in the figure; even though the copper backing behind the white sample plate seems solid, there is a hole to allow for transmission measurements, leaving only the alumina plate in line of the beam in addition to the sample itself. Good thermal connection with the sample was ensured by maximizing the copper contact in the holder of the alumina plate, while a tungsten needle was used to electrically connect to the front side Schottky contact. The contrast of the tungsten needle made beam alignment on the diode easy in transmission mode.

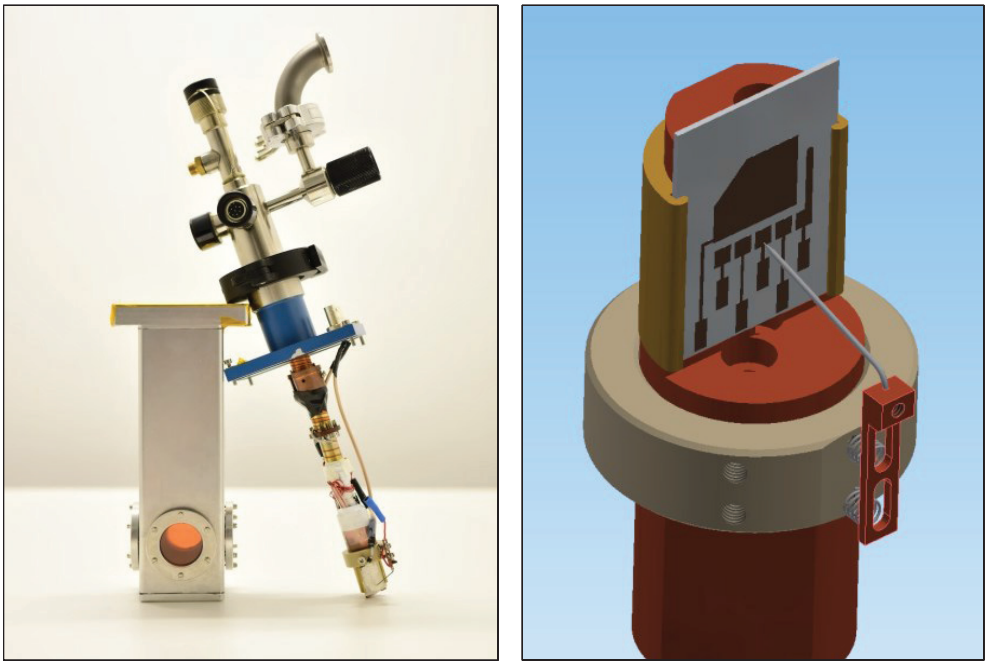

Figure 19 – Adaptions to an existing cryostat included making a new outer housing with x-ray compatible Kapton windows, and shielded cables and a new sample holder for capacitance measurements. The sample holder is seen detailed in the right panel.

Papers

Paper I

Bulk β-Ga_2O_3 with (010) and ($\bar{2}$01) Surface Orientation: Schottky Contacts and Point Defects

M. E. Ingebrigtsen, L. Vines, G. Alfieri, A. Mihaila, U. Badstübner, B.G. Svensson, A. Kuznetsov

Materials Science Forum, 2017. **897**: p. 755-758

Paper II

Iron and intrinsic deep level states in Ga_2O_3

M. E. Ingebrigtsen, J. B. Varley, A. Yu. Kuznetsov, B. G. Svensson, G. Alfieri, A. Mihaila, U. Badstübner, and L. Vines

Applied Physics Letters, 2018. **112**(4): p. 042104.

APPLIED PHYSICS LETTERS **112**, 042104 (2018)

Iron and intrinsic deep level states in Ga_2O_3

M. E. Ingebrigtsen,[1] J. B. Varley,[2] A. Yu. Kuznetsov,[1] B. G. Svensson,[1] G. Alfieri,[3]
A. Mihaila,[3] U. Badstübner,[3] and L. Vines[1]
[1]*University of Oslo, Department of Physics/Centre for Materials Science and Nanotechnology,*
P.O. Box 1048 Blindern, N-0316 Oslo, Norway
[2]*Lawrence Livermore Natl Lab, Livermore, California 94550, USA*
[3]*ABB Corporate Research, Segelhofstrasse 1K, 5405 Baden-Dättwil, Switzerland*

(Received 20 December 2017; accepted 11 January 2018; published online 24 January 2018)

Using a combination of deep level transient spectroscopy, secondary ion mass spectrometry, proton irradiation, and hybrid functional calculations, we identify two similar deep levels that are associated with Fe impurities and intrinsic defects in bulk crystals and molecular beam epitaxy and hydride vapor phase epitaxi-grown epilayers of β-Ga_2O_3. First, our results indicate that Fe_{Ga}, and not an intrinsic defect, acts as the deep acceptor responsible for the often dominating E2 level at $\sim$0.78 eV below the conduction band minimum. Second, by provoking additional intrinsic defect generation via proton irradiation, we identified the emergence of a new level, labeled as E2*, having the ionization energy very close to that of E2, but exhibiting an order of magnitude larger capture cross section. Importantly, the properties of E2* are found to be consistent with its intrinsic origin. As such, contradictory opinions of a long standing literature debate on either extrinsic or intrinsic origin of the deep acceptor in question converge accounting for possible contributions from E2 and E2* in different experimental conditions. © *2018 Author(s). All article content, except where otherwise noted, is licensed under a Creative Commons Attribution (CC BY) license (http://creativecommons.org/licenses/by/4.0/).* https://doi.org/10.1063/1.5020134

After the early work on gallium oxide (Ga_2O_3) in the mid-1900s, renewed interest has recently emerged on behalf of its prospects in power electronics and UV devices.[1–3] Particularly, the monoclinic β-Ga_2O_3 phase attracts interest due to its bandgap of $\sim$4.8 eV and n-type conductivity,[1] and promising MOSFET devices have already been demonstrated.[3] The control of the n-type charge carrier concentration can be achieved in the range of 10^{16}–10^{19} cm^{-3} using Si or Sn as dopants,[4,5] and semi-insulating materials can be made by substituting Ga with Fe, Mn, or Mg.[6–9] The latter elements act as deep acceptors and thereby compensate the n-type dopants, although little is known of the exact positions of their electronic states within the bandgap. Knowledge of the identities and positions of these types of deep levels is critical for further developing Ga_2O_3-based optoelectronic devices.

In the literature, several deep levels have been described in β-Ga_2O_3 from observations by electrical characterization techniques like deep level transient spectroscopy (DLTS)[10–12] and tentatively assigned to be either of intrinsic or extrinsic origin. In particular, Fe and Co—as the most common contaminants—were proposed to be involved in the levels appearing around 0.56 and 1.0 eV below the conduction band minimum (CBM).[10] Another level appearing in the vicinity of 0.8 eV below the CBM, conventionally labeled E2, was identified in numerous samples grown from independent techniques and suggested to be the dominant source of compensation in the bulk crystals.[10,11] Of the native defects, hybrid functional calculations have suggested that gallium vacancies (V_{Ga}) may be the acceptors that contribute to this electrical compensation, as well as their complexes with hydrogen.[13] Initial calculations using HSE (Heyd-Scuseria-Ernzerhof) functionals predicted these levels to be around 1.6 and 1.8 eV below the CBM for (–2/–3) transitions related to the tetrahedrally coordinated V_{Ga} (I) and octahedrally coordinated V_{Ga} (II), respectively,[13] while more recent calculations argue these levels to be closer to the conduction band, specifically around 0.67 and 1.0 below CBM.[14] These results are consistent with positron annihilation studies that identify V_{Ga} -related defects to account for compensation in Si-doped Ga_2O_3 epitaxial films,[15] but their concentration in bulk crystals remains to be determined. The oxygen vacancy (V_O) is also expected to be responsible for deep levels in the upper part of the bandgap, with the (0/+2) transition levels reported to fall between $\sim$1.3 and 2.7 eV below CBM depending on the particular symmetry of the distinct V_O (I), V_O (II), and V_O (III) lattice sites.[2,14] Despite these experimental and theoretical efforts, unambiguous identification of the electrically active defects in β-Ga_2O_3 remains largely unresolved. Here, using a combination of deep level transient spectroscopy (DLTS), secondary ion mass spectrometry (SIMS), irradiation experiments, and hybrid functional calculations, we establish a strong link between the E2 level and the Fe content in a range of different samples. Our results suggest that Fe substitutional impurities are the dominant background acceptor in many bulk crystals and responsible for the E2 deep level 0.78 ± 0.04 eV below the CBM. We also identify an additional, distinct level at around 0.75 eV below the CBM that arises with irradiation and is likely attributed to a native defect or defect complex.

Experimentally, we studied bulk single crystals and homo-epitaxial β-Ga_2O_3 films synthesized by Tamura Corporation. The bulk crystals were fabricated with Edge-defined Film-fed Growth (EFG) and have surfaces oriented in the (010) or the $(\bar{2}01)$ direction. These wafers were nominally undoped but exhibited n-type conductivity with charge carrier

© Author(s) 2018.

concentrations (N_d) in the range of $0.6–2.6 \times 10^{17}\,\text{cm}^{-3}$. The homo-epitaxial films were grown on (010) oriented substrates by either molecular beam epitaxy (MBE) or hydride vapor phase epitaxi (HVPE) to thicknesses of 2 and 10 μm, respectively. The substrates for the films were doped with Sn, yielding charge carrier concentrations $\sim 5 \times 10^{18}\,\text{cm}^{-3}$, while those in the films were found to be $\sim 2 \times 10^{16}$ and $\sim 8 \times 10^{16}\,\text{cm}^{-3}$ for the MBE and HVPE samples, respectively. Samples of the bulk single crystals will hereafter be referred to as bulk samples, while the epitaxially grown ones are labelled as MBE and HVPE. For electrical characterization, Schottky contacts were deposited through a shadow mask using e-beam evaporation of 150 nm Ni, yielding circular contacts of radii 400, 240, and 100 μm. Further, backside Ohmic contacts were prepared by e-beam deposition of a Ti and Al stack of 10 and 150 nm thickness, respectively. Barrier heights of the Schottky contacts as high as $\sim$1.4 eV and ideality factors as low as 1.05 were observed from current-voltage characteristics with up to eight orders of magnitude rectification.[12]

The (010) oriented bulk and the HVPE samples were exposed to an irradiation of 600 keV protons (H^+) at room temperature, with a projected range of about 4.3 μm as estimated by Monte Carlo simulations using the SRIM code.[16] From these SRIM simulations, a close to homogeneous profile of vacancy generation is anticipated in the shallower depths relevant for DLTS characterization. Irradiation doses of 2×10^{13} and $3 \times 10^{14}\,\text{H/cm}^2$ were used for the HVPE and bulk samples, respectively. These irradiation conditions caused strong charge carrier compensation, but the electrical conductivity was largely re-established during the first DLTS temperature scan up to 600 K. Subsequent capacitance-voltage measurements indicate flat charge carrier concentration profiles in the irradiated samples. The DLTS measurements were performed with a refined version of the system described in Ref. 17, with –8 V reverse bias voltage and pulsing up to –1 V. From this, analysis of the DLTS signal was done using lock-in and GS4 weighting functions applied to the transients in rate windows from $(20\,\text{ms})^{-1}$ to $(2560\,\text{ms})^{-1}$. The energy positions and capture cross sections of the deep levels were derived from Arrhenius plots of the peak positions. Identification of residual impurities and quantification of their concentrations in the samples were accomplished by SIMS using a Cameca IMS7f spectrometer equipped with Cs and O_2 primary ion sources. Absolute concentration calibrations for the observed impurities were obtained using ion implanted reference samples. For the depth calibration, the sputtered crater depths were measured using a Dektak 8 stylus profilometer and a constant erosion rate was assumed.

Our modelling adopts the HSE06 screened hybrid functional[18,19] and projector-augmented wave (PAW) approach[20] as implemented in the VASP code.[21,22] We include semicore Ga 3*d* and Fe 3*p*, 3*d*, and 4*s* electrons as explicit valence states and set the fraction of screened Hartree-Fock exchange to 32%. This choice yields a bandgap of 4.85 eV and optimal lattice constants of 12.21, 3.03, and 5.79 Å for the *a*, *b*, and *c* lattice parameters, respectively, in excellent agreement with experimental values.[2,24,25] To assess the favorability of incorporating Fe on a Ga site, we compute the formation energy (E^f) given by the expression

$$E^f\left[\text{Fe}_{\text{Ga}}^q\right] = E_{\text{tot}}\left[\text{Fe}_{\text{Ga}}^q\right] - E_{\text{tot}}[\text{Ga}_2\text{O}_3] + \mu_{\text{Ga}} - \mu_{\text{Fe}} + q\epsilon_F + \Delta^q, \qquad (1)$$

where $E_{\text{tot}}[\text{Fe}_{\text{Ga}}^q]$ represents the total energy of the supercell containing one substitutional Fe_{Ga} in the charge state *q*, and $E_{\text{tot}}[\text{Ga}_2\text{O}_3]$ is the total energy of a perfect crystal in the same supercell. We vary the chemical potential of Ga (μ_{Ga}) between the Ga-rich limit in which it is in equilibrium with bulk elemental Ga, and the O-rich limit in which it is bound by the stability condition of Ga_2O_3 (e.g., $\mu_{\text{Ga}} = 1/2\ \Delta H[\text{Ga}_2\text{O}_3] = -4.47\,\text{eV}$). Similarly, the chemical potential of μ_{Fe} is bound by the solubility-limiting phases of Ga_3Fe ($\Delta H = -1.03\,\text{eV}$) in the Ga-rich limit and Fe_2O_3 ($\Delta H = -8.54\,\text{eV}$) in the O-rich limit.[23] The electron chemical potential is defined by the Fermi level position ϵ_F, which we reference to the valence-band maximum (VBM). The Δ^q term defines the finite-size correction for charged defects following the scheme of Refs. 26–28 for which we consider the dielectric tensor assuming electronic only (ϵ_∞) and electronic plus ionic (ϵ_{DC}) screening contributions as a proxy for the uncertainty in our reported values.[14,29] Specifically, these adopt values of 11.5 (3.8), 11.8 (2.8), and 11.1 (3.8) for the ϵ_{xx}, ϵ_{yy}, and ϵ_{zz} components of ϵ_{DC} (ϵ_∞) tensors.[29]

Figure 1 shows DLTS spectra of four different samples: two spectra from the bulk samples having different surface orientations and two from the MBE and HVPE films. At least four signatures of deep level defects are observed; similar defect levels have previously been reported in the literature and labelled E1-E4.[10,12] The energy positions for E1 to E4 in Fig. 1 are 0.56, 0.78, 1.01, and 1.48 eV below CBM, respectively. Of these levels, E1 occurs in the (010) oriented bulk sample and with a low concentration in the MBE sample. E3 is clearly resolved only in the bulk (010) sample, although it may also be found as part of the high temperature shoulder of the E2 level in the ($\bar{2}01$) bulk sample. In contrast, E4 is only seen in the bulk (010) sample. The level traditionally labelled as E2 is the most prominent one of all and particularly dominant in the ($\bar{2}01$) sample (note the large scale around the E2 region in Fig. 1). The expression on the y-axis of Fig. 1 ($2N_d \times \Delta C/C$) is an approximation valid for dilute

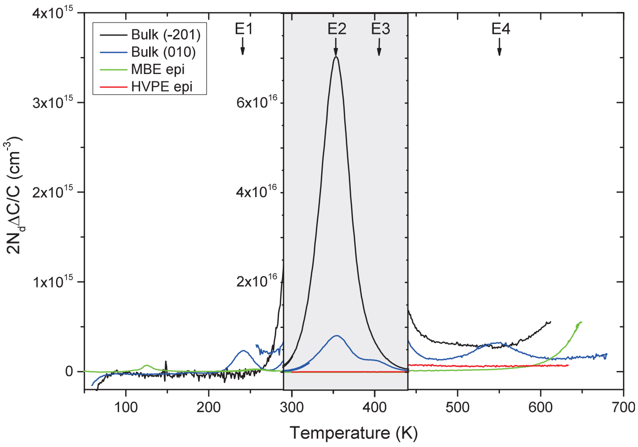

FIG. 1. DLTS signal ($2N_d \times \Delta C/C$) versus temperature for (010) and ($\bar{2}01$) oriented bulk, as well as MBE and HVPE samples, here represented by $(640\,\text{ms})^{-1}$ lock-in rate window. Note the different vertical-scale in the temperature range of E2.

deep level concentrations, typically considered up to 10%–20% of (N_d). Note, however, that the concentration of E2 in the $(\bar{2}01)$ bulk sample is 30% of (N_d) and thus the dilute approximation does not strictly hold, resulting in a slight overestimation of the E2 concentration.[30] Nonetheless, the conclusion of a dominating presence in this sample over the other samples remains. In the HVPE sample, the E2 peak may be present at concentrations close to the detection limit of the measurement, $\leq 6 \times 10^{13}\,\mathrm{cm}^{-3}$ in this sample, while the MBE sample has no discernible E2 peak above the noise level at $\sim 1 \times 10^{14}\,\mathrm{cm}^{-2}$. As such, the E2 intensity is prominently scaled in the different samples providing a suitable starting point of its identification.

Figure 2(a) shows the DLTS spectra detected in the 300–450 K range (shadowed area in Fig. 1) for the bulk (010) and HVPE samples, before and after irradiation with 600 keV H^+ to doses of 3×10^{14} and $2 \times 10^{13}\,\mathrm{cm}^{-2}$, respectively. Prior to the irradiation (as already shown in Fig. 1), the bulk sample exhibits a dominating E2 signature at 0.78 ± 0.04 eV with a peak at 354 ± 4 K using a lock-in rate window of $(640\,\mathrm{ms})^{-1}$, while it is barely visible in the HVPE sample (with an absolute concentration on the order of $\sim 6 \times 10^{13}\,\mathrm{cm}^{-3}$ as deduced from the inset in Fig. 2). After the irradiation and an initial DLTS scan up to 650 K of the bulk sample, the amplitude of the peak at 354 K remains similar to that before the irradiation, while a new peak, labelled E2*, appears on the low temperature side (with a peak temperature of 317 ± 4 K). The energy position of the E2* is found to be 0.75 eV, i.e., similar to that of E2, but with a larger apparent capture cross section ($\sim 5 \times 10^{-14}$) as compared to E2 ($\sim 7 \times 10^{-15}$) cm^{-2}. A similar trend is observed in the HVPE sample, where the DLTS signature at 317 K emerges, while the trace of the 354 K peak appears as a shoulder on the high temperature side of the 317 K peak (still with a low concentration). Arrhenius plots of the two deep levels are presented in Fig. 2(b). The fact that the concentration of E2 is not significantly influenced by the generation of the intrinsic defects implies that this level is of extrinsic origin involving a residual impurity rather than an intrinsic defect only. E2*, on the other hand, shows a strong response on the irradiation as expected for a defect of intrinsic origin like V_{Ga} or a related complex. The energetic similarity of E2 and E2* helps to resolve the debate in the literature regarding the level identification in the energy range of E2.[10,12,14]

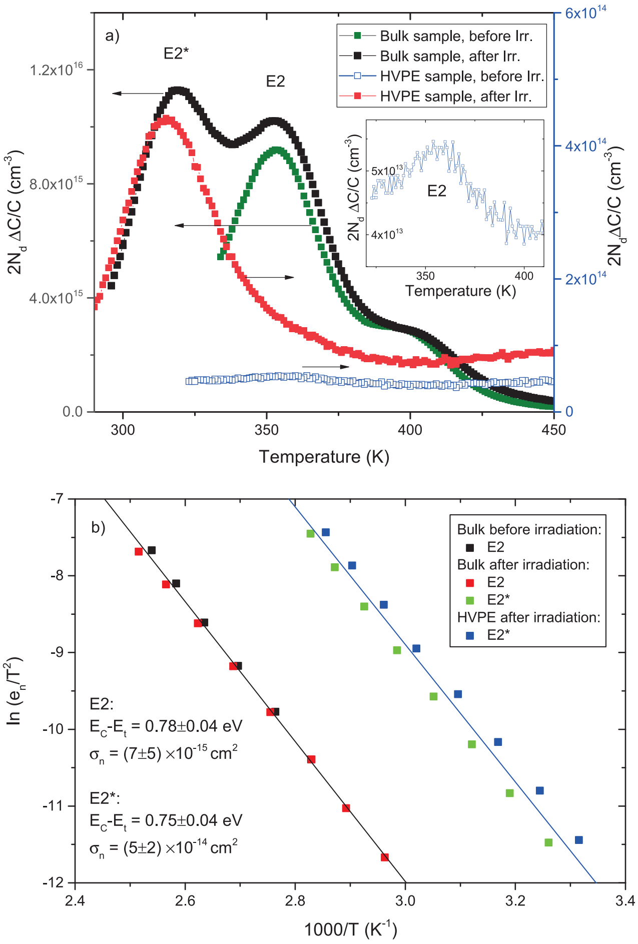

FIG. 2. (a) DLTS signal ($2N_d \times \Delta C/C$) using a $(640\,\mathrm{ms})^{-1}$ lock-in rate window versus temperature scans for the (010) oriented bulk and HVPE samples, before and after irradiation with 600 keV H^+ to a dose of 3×10^{14} and $2 \times 10^{13}\,\mathrm{cm}^{-2}$, respectively. The inset shows an enlarged region of the DLTS signal from the HVPE sample (as-grown), indicating a minor presence of the E2 level already before irradiation. In (b), the corresponding Arrhenius plots of the electron emission rates are shown.

In order to identify the residual impurity associated with E2, SIMS analysis was performed and revealed that Al, Si, Fe, and In are present in concentrations above the E2 concentrations in corresponding samples. Of these, only Si and Fe show the concentration variation resembling that of the E2 concentration variation that was discussed above. The relationships of the E2 concentration with Fe and Si concentrations are presented in Fig. 3. As discussed above, our DLTS measurements result in a small overestimation of the E2 concentration in the $(\bar{2}01)$ bulk samples. Indeed, taking this into account would improve the parallelism with the [E2] = [Fe] line in Fig. 3. However, Si shows only a weak dependence and is excluded as a viable alternative. This is supported by the fact that Si is expected to act as a shallow donor and the observations of very low concentrations (or even absence) of E2 in the epitaxial films despite a strong Si presence. Hence, the remaining candidate accounting for the trend of the E2 content is Fe. Indeed, Fig. 3 shows the E2

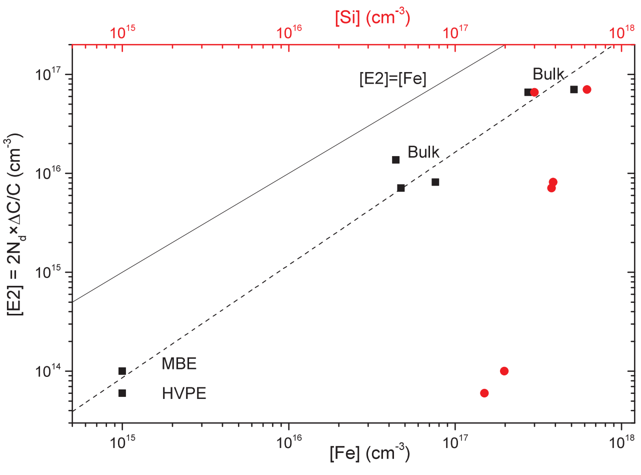

FIG. 3. E2 concentration as measured by DLTS versus Fe concentration (black squares) and Si concentration (red circles) as found by SIMS for bulk and epitaxial samples.

concentration in a close to linear correlation with the Fe concentration in the samples. A similar correlation with the E2* signal is not observed, as evident from the low measured Fe concentration in the thin-films in Fig. 3 and the E2* signal of irradiated films in Fig. 2. This further supports the conclusion of an intrinsic origin of the E2* level. Note that the E2 in MBE and Fe concentrations in both MBE and HVPE films labels an upper limit due to sensitivity limitations in the measurements. Notably, the concentration ratio between E2 and Fe is ~0.1 (Fig. 3), and hence, other Fe-related centers or configurations may also be anticipated to form in β-Ga_2O_3.

To corroborate the experimental results, we include the calculated formation energies of the Fe_{Ga} defects in Fig. 4. We find Fe_{Ga} to be favorable defects for Fermi levels spanning over the entire bandgap and in both O-poor and O-rich limits, suggesting that Fe impurities or dopants may be readily incorporated in Ga_2O_3. We omit Fe interstitials and substitutions on the O sites that have significantly higher E^f in the relevant case of *n*-type conditions. Figure 4 shows the data corrected with the ϵ_{DC} values; the alternative choice of electronic-only screening ϵ_∞ leads to higher E^f values for the singly charged defects by ~0.2 eV. Fe_{Ga} preferentially incorporates on the octahedral Ga site (Fe_{GaII}), while Fe substitution on the tetrahedral site (Fe_{GaI}) also exhibits a low E^f. Both configurations are predicted to act as deep acceptors in *n*-type conditions. The deep acceptor configurations correspond to an Fe^{2+} oxidation state, which preferentially adopts a high-spin configuration ($S = 2$) and exhibits an outward relaxation of the bond lengths by ~4%–8% (similar to that reported for Fe_{Ga} defects in GaN that are subjected to a different local lattice symmetry).[31] As the Fe^{2+} has not been observed by EPR in β-Ga_2O_3, far higher Fe contents may be present than were previously assumed from EPR signals of the residual Fe^{3+} impurities observed in bulk samples grown by independent groups and methods.[10,32,33] Our calculated thermodynamic transition level for the Fe^{3+}/Fe^{2+} [i.e., the $\epsilon(0/-)$ in Fig. 4] falls 0.61 eV below the CBM for Fe_{GaII} and 0.59 eV below the CBM for Fe_{GaI}. If we assume the lower screening associated with the ϵ_∞,[14] these levels fall slightly higher, 0.40 and 0.36 eV below the CBM, respectively. While the agreement with experiment is better with ϵ_{DC}, the levels computed assuming electronic-only screening is still in reasonable agreement with the measured E2 level.

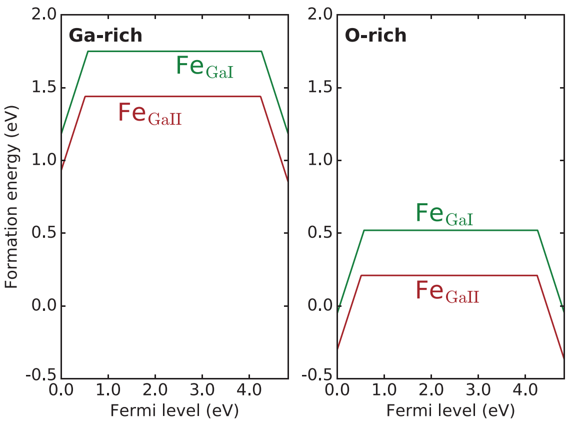

FIG. 4. Formation energy diagram for Fe_{Ga} in β-Ga_2O_3 shown for both Ga-rich and O-rich growing conditions. Ga_I and Ga_{II} denote two possible configurations of Ga in the lattice.

Our results are also consistent with those of Irmscher *et al.*[10] and Zhang *et al.*[11] in Czocralski and EFG-grown bulk crystals that exhibit Fe concentrations in excess of $10^{16}\,cm^{-3}$ and are believed to be the dominant compensating acceptor. Considering the correlation with the Fe content (Fig. 3) and the calculated E^f of the Fe impurities relative to that of other compensating acceptors like V_{Ga} in *n*-type conditions and more Ga-rich growth environments,[13,14] Fe_{Ga} appears to be a likely candidate for the E2 level. We note that while we predict Fe_{Ga} to also have a deep donor level 0.3–0.5 eV above the VBM, this level cannot be observed in by the DLTS approach used in the present study.

In conclusion, our results strongly suggest that Fe_{Ga}, and not an intrinsic defect such as V_{Ga}, acts as the deep acceptor responsible for the prominent E2 level at ~0.78 eV below the CBM. Concurrently, by enhancing the intrinsic defect concentration via proton irradiation, a new deep level emerged, labeled as E2*, having the ionization energy very close to that of E2, but exhibiting an order of magnitude higher capture cross section. Importantly, the properties of E2* are found to be consistent with an intrinsic origin and are consistent with V_{Ga} or related complexes as viable candidates, although an unambiguous assignment of the intrinsic origin of the E2* level will require further study. Perhaps ironically, the contradicting opinions of the literature debate on either extrinsic or intrinsic origin of the deep acceptor E2 converge by accounting for possible contributions from both E2 and E2* in different experimental conditions.

Financial support is acknowledged from the Research Council of Norway through the FriPro and Synknøyt program (Project Nos. 239895 and 228578), the Norwegian Micro- and Nano-Fabrication Facility (NorFab 197411/V30), and was partly performed under the auspices of the U.S. Department of Energy at Lawrence Livermore National Laboratory (LLNL) under Contract No. DE-AC52-07NA27344.

[1] H. H. Tippins, Phys. Rev. **140**, A316 (1965).
[2] J. B. Varley, J. R. Weber, A. Janotti, and C. G. Van de Walle, Appl. Phys. Lett. **97**, 142106 (2010).
[3] M. Higashiwaki, K. Sasaki, H. Murakami, Y. Kumagai, A. Koukitu, A. Kuramata, T. Masui, and S. Yamakoshi, Semicond. Sci. Technol. **31**, 034001 (2016).
[4] E. G. Villora, K. Shimamura, Y. Yoshikawa, T. Ujii, and K. Aoki, Appl. Phys. Lett. **92**, 202120 (2008).
[5] N. Suzuki, S. Ohira, M. Tanaka, T. Sugawara, K. Nakajima, and T. Shishido, Phys. Status Solidi C **4**, 2310 (2007).
[6] M. Higashiwak, K. Sasaki, T. Kamimura, M. H. Wong, D. Krishnamurthy, A. Kuramata, T. Masui, and S. Yamakoshi, Appl. Phys. Lett. **103**, 123511 (2013).
[7] D. Guo, P. G. Li, Z. P. Wu, W. Cui, X. L. Zhao, M. Lei, L. H. Li, and W. H. Tang, Sci. Rep. **6**, 24190 (2016).
[8] M. Higashiwaki, K. Sasaki, A. Kuramata, T. Masui, and S. Yamakoshi, Appl. Phys. Lett. **100**, 013504 (2012).
[9] Z. Galazka, K. Irmscher, R. Uecker, R. Bertram, M. Pietsch, A. Kwasniewski, M. Naumann, T. Schulz, R. Schewski, D. Klimm, and M. Bickermann, J. Cryst. Growth **404**, 184 (2014).
[10] K. Irmscher, Z. Galazka, M. Pietsch, R. Uecker, and R. Fornari, J. Appl. Phys. **110**, 063720 (2011).
[11] Z. Zhang, E. Farzana, A. R. Arehart, and S. A. Ringel, Appl. Phys. Lett. **108**, 052105 (2016).

[12] M. E. Ingebrigtsen, L. Vines, G. Alfieri, A. Mihaila, U. Badstübner, B. G. Svensson, and A. Y. Kuznetsov, Mater. Sci. Forum **897**, 755 (2017).

[13] J. B. Varley, H. Peelaers, A. Janotti, and C. G. Van de Walle, J. Phys.: Condes. Matter **23**, 334212 (2011).

[14] P. Deak, Q. Duy Ho, F. Seeman, B. Aradi, M. Lorke, and T. Frauenheim, Phys. Rev. B **95**, 075208 (2017).

[15] E. Korhonen, F. Tuomisto, D. Gogova, G. Wagner, M. Baldini, Z. Galazka, R. Schewski, and M. Albrecht, Appl. Phys. Lett. **106**, 242103 (2015).

[16] J. F. Ziegler, J. P. Biersack, and U. Littmark, *The Stopping and Range of Ions in Solids* (Pergamon, New York, 1985).

[17] B. G. Svensson, K.-H. Rydén, and B. M. S. Lewerentz, J. Appl. Phys. **66**, 1699 (1989).

[18] J. Heyd, G. E. Scuseria, and M. Ernzerhof, J. Chem. Phys. **118**, 8207 (2003).

[19] J. Heyd, G. E. Scuseria, and M. Ernzerhof, J. Chem. Phys. **124**, 219906 (2006).

[20] P. E. Blöchl, Phys. Rev. B **50**, 17953 (1994).

[21] G. Kresse and J. Furthmuller, Phys. Rev. B **54**, 11169 (1996).

[22] G. Kresse and J. Furthmuller, Comp. Mater. Sci. **6**, 15 (1996).

[23] S. V. Meschel and O. J. Kleppa, J. Alloy. Comp. **290**, 150–156 (1999).

[24] T. Onuma, S. Saito, K. Sasaki, K. Goto, T. Masui, T. Yamaguchi, T. Honda, A. Kuramata, and M. Higashiwaki, Appl. Phys. Lett. **108**, 101904 (2016).

[25] S. Geller, J. Chem. Phys. **33**, 676 (1960).

[26] C. Freysoldt, J. Neugebauer, and C. G. Van de Walle, Phys. Status Solidi B **248**, 1067 (2011).

[27] C. Freysoldt, B. Grabowski, T. Hickel, J. Neugebauer, G. Kresse, A. Janotti, and C. G. Van de Walle, Rev. Mod. Phys. **86**, 253 (2014).

[28] Y. Kumagai and F. Oba, Phys. Rev. B **89**, 195205 (2014).

[29] M. Schubert, R. Korlacki, S. Knight, T. Hofmann, S. Schöeche, V. Darakchieva, E. Janzén, B. Monemar, D. Gogova, Q. T. Thieu, R. Togashi, H. Murakami, Y. Kumagai, K. Goto, A. Kuramata, S. Yamakoshi, and M. Higashiwaki, Phys. Rev. B **93**, 125209 (2016).

[30] E. V. Monakhov, J. Wong-Leung, A. Yu. Kuznetsov, C. Jagadish, and B. G. Svensson, Phys. Rev. B **65**, 245201 (2002).

[31] D. Wickramaratne, J.-X. Shen, C. E. Dreyer, M. Engel, M. Marsman, G. Kresse, S. Marcinkevicius, A. Alkauskas, and C. G. Van de Walle, Appl. Phys. Lett. **109**, 162107 (2016).

[32] B. E. Kananen, L. E. Halliburton, K. T. Stevens, G. K. Foundos, and N. C. Giles, Appl. Phys. Lett. **110**, 202104 (2017).

[33] B. E. Kananen, N. C. Giles, L. E. Halliburton, G. K. Foundos, K. B. Chang, and K. T. Stevens, J. Appl. Phys. **122**, 215703 (2017).

Paper III

Impact of proton irradiation on conductivity and deep level defects in β-Ga_2O_3

M.E. Ingebrigtsen, A.Yu.Kuznetsov, B.G. Svensson, G. Alfieri, A. Mihaila, U. Badstübner, A. Perron, L. Vines, and J.B. Varley

APL Materials 7, 022510 (2019)

Impact of proton irradiation on conductivity and deep level defects in β-Ga_2O_3

Cite as: APL Mater. 7, 022510 (2019); doi: 10.1063/1.5054826
Submitted: 4 September 2018 • Accepted: 10 October 2018 •
Published Online: 14 December 2018

M. E. Ingebrigtsen,[1] A. Yu. Kuznetsov,[1] B. G. Svensson,[1] G. Alfieri,[2] A. Mihaila,[2] U. Badstübner,[2]
A. Perron,[3] L. Vines,[1] and J. B. Varley[3]

AFFILIATIONS

[1] Department of Physics/Centre for Materials Science and Nanotechnology, University of Oslo, P.O. Box 1048, Blindern, N-0316 Oslo, Norway
[2] ABB Corporate Research, Segelhofstrasse 1K, 5405 Baden-Dättwil, Switzerland
[3] Lawrence Livermore National Laboratory, Livermore, California 94550, USA

ABSTRACT

Single crystalline bulk and epitaxially grown gallium oxide (β–Ga_2O_3) was irradiated by 0.6 and 1.9 MeV protons to doses ranging from 5×10^9 to 6×10^{14} cm^{-2} in order to study the impact on charge carrier concentration and electrically active defects. Samples irradiated to doses at or above 2×10^{13} cm^{-2} showed a complete removal of free charge carriers in their as-irradiated state, whereas little or no influence was observed below doses of 6×10^{12} cm^{-2}. From measurements at elevated temperatures, a thermally activated recovery process is seen for the charge carriers, where the activation energy for recovery follow a second-order kinetics with an activation energy of ~1.2 eV. Combining the experimental results with hybrid functional calculations, we propose that the charge carrier removal can be explained by Fermi-level pinning far from the conduction band minimum (CBM) due to gallium interstitials (Ga_i), vacancies (V_{Ga}), and antisites (Ga_O), while migration and subsequent passivation of V_{Ga} via hydrogen-derived or V_O defects may be responsible for the recovery. Following the recovery, deep level transient spectroscopy (DLTS) reveals generation of two deep levels, with energy positions around 0.75 and 1.4 eV below the CBM. Of these two levels, the latter is observed to disappear after the initial DLTS measurements, while the concentration of the former increases. We discuss candidate possibilities and suggest that the origins of these levels are more likely due to a defect complex than an isolated point defect.

© 2018 Author(s). *All article content, except where otherwise noted, is licensed under a Creative Commons Attribution (CC BY) license (http://creativecommons.org/licenses/by/4.0/).* https://doi.org/10.1063/1.5054826

Gallium oxide (Ga_2O_3) is a wide bandgap semiconductor (E_g ~ 4.8 eV[1,2]), which has received considerable attention during the past years due to its potential applications in UV detectors and high-voltage devices.[3] The most stable phase at ambient conditions, β–Ga_2O_3, has a high breakdown field, estimated at ~8 MV/cm,[4] which is a major advantage in power electronics. However, the technological advances of Ga_2O_3 are hampered by the difficulty in controlling and understanding the electrical behavior of intrinsic and impurity-related defects. Similar to most other oxide semiconductors, β–Ga_2O_3 shows inherent n-type conductivity, where native defects may play an important role. Several of the primary defects are electrically active, where hybrid functional calculations have suggested gallium vacancies (V_{Ga}), as well as their complexes with hydrogen to be deep acceptors and the gallium interstitial to be a shallow donor. The oxygen vacancy and interstitial are proposed to be deep donors and hence electrically neutral for Fermi-level positions close to conduction band minimum (CBM).[5,6] Furthermore, the primary defects are predicted to be mobile at relatively modest temperatures; recent theoretical estimates suggest that the activation barrier for vacancy migration is in the range of 0.5–1.6 eV, while that for the gallium interstitial (Ga_i) may be as low as 0.1 eV.[7,8] Thus, vacancy and interstitial-related complexes may also play a crucial role for the electrical properties of β–Ga_2O_3.

So far, studies using deep level transient spectroscopy (DLTS) and deep level optical spectroscopy (DLOS) have revealed several bandgap states,[9–13] where both intrinsic and extrinsic origins have been proposed, although firm identification remains largely unresolved. In this respect, studying irradiated (or implanted) samples is indispensable for the identification and understanding of electrically active defects, and combined with characterization techniques like DLTS, it is a powerful concept to obtain insight into their origin and formation kinetics. Herein, we report on the consequences of subjecting bulk and epitaxial β−Ga_2O_3 samples to 0.6 and 1.9 MeV proton irradiation. We first describe how a loss of charge carriers is observed during irradiation, with a subsequent recovery during DLTS scans up to 650 K. We then assess the irradiation-induced deep level defects using a combination of DLTS measurements and hybrid functional calculations and discuss their possible origins for the carrier depletion and recovery based on the results.

For the experimental measurements, we studied bulk single crystals and homoepitaxial β−Ga_2O_3 films synthesized by Tamura Corporation. The bulk crystals were grown by Edge-defined Film-fed Growth (EFG) and cut with a (010) surface orientation. These wafers were nominally undoped but exhibited n-type conductivity with charge carrier concentrations (N_d) in the range of 0.7-2.3 × 10^{17} cm^{-3}. The homoepitaxial films were grown on (001) and (010) oriented substrates by hydride vapor phase epitaxy (HVPE) and molecular beam epitaxy (MBE), respectively. While the substrates for the films were Sn-doped to $N_d \sim 5 \times 10^{18}$ cm^{-3}, the 10-μm-thick HVPE films and the 2-μm-thick MBE films showed $N_d \sim 8 \times 10^{16}$ cm^{-3} and ∼3 × 10^{16} cm^{-3}, respectively. Samples cut from the bulk single crystals will hereafter be referred to as bulk samples, while the epitaxially grown are labeled HVPE and MBE in accordance with their synthesis method.

For the electrical characterization, Schottky contacts were deposited through a shadow mask using e-beam evaporation of 150 nm Ni, yielding circular contacts of radii 100, 240, and 400 μm. Furthermore, backside Ohmic contacts were prepared by e-beam deposition of a Ti and Al stack of 10 and 150 nm thicknesses, respectively. Barrier heights of the Schottky contacts as high as ∼1.4 eV and ideality factors as low as 1.05 were found from current-voltage characteristics with up to eight orders of magnitude rectification.[11]

After preparation and initial characterization, the samples were implanted at room temperature in vacuum (<5 × 10^{-7} Torr), with H^+ ions to study the generation of damage. High acceleration potentials were chosen to place the implantation peaks far from the depletion region in order to not observe the ions themselves but to study the generation of intrinsic secondary defects. Hence, the damage from implantation is irradiation-like, with flat damage profiles in the tail region probed by capacitance measurements close to the surface. For the H^+ ions, two ion energies were chosen. First, low doses in the range of 5 × 10^9 to 5 × 10^{10} cm^{-2} were prepared with 1900 keV H^+ ions, having a projected range of 22 μm, as estimated by simulations using the SRIM code.[14] Second, samples were implanted using 600 keV H^+ ions with doses ranging from 6 × 10^{11} to 6 × 10^{14} cm^{-2} and a projected range (R_p) of ∼4.3 μm. DLTS was carried out while scanning up and down in temperature using a refined version of a setup described in Ref. 15, and a quiescent reverse bias of −8 V was used along with filling pulses to −1 V bias for 50 ms duration. A temperature range up to 650 K was employed to probe levels deep into the bandgap, and the measurements were carried out in a chamber evacuated to a rough vacuum (≤10^{-3} Torr).

To evaluate the energetics of various native defects and complexes that may contribute to the DLTS signals, we performed calculations using the Heyd-Scuseria-Ernzerhof (HSE06) screened hybrid functional[16] and projector-augmented wave (PAW) approach[17] as implemented in the VASP code.[18] We include semi-core Ga 3d electrons as explicit valence states and set the fraction of screened Hartree-Fock exchange to 32% which accurately describes both the experimental bandgap and the structural parameters as reported elsewhere.[2,19] Owing to the complexity and size of various vacancy complexes, we adopted 160-atom supercells as evaluated with a plane wave cutoff of 400 eV and a single shifted Monkhorst-Pack k−point at 0.25, 0.25, 0.25. We assess the point defect formation energies and their associated electronic transition levels using the formalism as described previously, with finite-size corrections adopted using the schemes in Refs. 20–22. To additionally assess the uncertainty in our reported defect levels, we consider the two extremes where the charged defects are corrected using the experimental dielectric constants that reflect the purely electronic contribution (ϵ_∞) and additionally including ionic screening contributions owing to the response of the lattice to the defect (ϵ_0).[19,23] In principle, the ϵ_0 should be used, but owing to the large size of the defects and complexes considered in our relatively small, periodically repeated supercell, there may not be appropriate screening to fully capture the ϵ_0 in this highly polar and anisotropic material.[6] Convergence tests for the $V_{Ga^{-3}}$ suggest that ϵ_0 is still a far better choice than ϵ_∞, which we find yields inadequately-corrected values that still suffer from a significant supercell-size dependence (see supplementary material). Nonetheless, we consider both limits to provide more transparency in possible uncertainty of theoretically reported levels and to assist in resolving the identification of the defect states experimentally identified in Ga_2O_3. Further experimental evidence will help clarify the limitations in the current theoretical approaches and identify which model of the screening is most appropriate for making reliable predictions. In the manuscript, we include plots using the ϵ_0 data, whereas plots using ϵ_∞ and additional details of the calculations are provided in the supplementary material.

Samples that were subjected to H^+ doses at or above 2 × 10^{13} cm^{-2} exhibited a near-complete removal of charge carriers in the depletion region, as manifested through a reduction in the measured capacitance. In these samples, the remaining capacitance is in the order of a few pF and in reasonable agreement with a depletion depth that corresponds to the implanted peak depth (projected range, R_p). Furthermore, the capacitance does not respond to the voltage changes of our measurements. From this it seems that instead of probing the region near the Schottky contact, in the range of

50-500 nm as is typical for the un-irradiated samples, the capacitance of as-irradiated samples is defined by the implantation peak. Contrarily, at lower doses, below 6×10^{12} cm^{-2}, similar capacitance reduction is not observed.

SRIM simulations using a threshold energy for displacement of atoms of 15 eV, a typical value for semiconductors,[24,25] estimate the vacancy generation from 600 keV H$^+$ ions to be 1.1×10^{-5} vacancies/(ion Ångstrom) [#/(ion Å)] in the tail region of the implantation. The corresponding peak value around the projected range of the ions was ~3.9×10^{-3} #/(ion Å). Of the generated defects, consider 5% a generous upper limit for the amount that survives dynamic annealing. Thus, for a dose of 2×10^{13} cm^{-2}, this results in an upper limit of the defect concentrations of 1.1×10^{16} and 3.9×10^{17} cm^{-3} for the tail region and around R_p, respectively. With carrier concentrations in the range of 10^{16}–10^{17} cm^{-3}, the estimated defect generation in the implantation tail is insufficient to account for the charge carrier removal. Hence, this corroborates that the removal is likely to occur due to the region around R_p. Nonetheless, the removal occurring in the region around R_p indicates a low dynamic annealing of the irradiation-induced defects, in accordance with that observed for low-temperature irradiations using ohmic contacts.[26] In addition, it indicates a substantial formation of electrically active intrinsic defects in the samples.

Annealing the irradiated samples at temperatures above 450-650 K results in the recovery of charge carriers in a thermally stimulated process. Figure 1 shows the recovery of the reverse bias capacitance as a function of temperature from DLTS measurements on as-irradiated samples of HVPE and bulk material. For ease of comparison, the capacitance was normalized to the value at room temperature before irradiation. The solid symbols show the measurements during heating and the open symbols display the measurement during the subsequent cooling, where the cooling/heating was carried out at a rate of 2 K/min. Distinctive steps in the capacitance are seen in the measurements when heating the samples from their as-irradiated state, representing recovery of charge carriers. Interestingly, for the HVPE samples, this step appears at a lower temperature for the sample irradiated to a dose of 2×10^{13} cm^{-2} compared with that of 1×10^{14} cm^{-2}, and recovery appears stronger in the bulk sample compared with that of the HVPE for a similar dose.

We will, in the following, focus our attention on this charge carrier recovery, which appears to be a thermally activated process, and study the kinetics of this reaction. Bulk samples irradiated to H$^+$ doses of 3×10^{14} and 6×10^{14} cm^{-2} were subject to continuous CV measurements at constant temperatures. Figure 2 shows the charge carrier concentration (n) as a function of depth of the bulk sample for the higher dosage as it develops over time at a constant temperature of 510 K. The values were calculated from CV measurements performed over 6 h, and warmer colors correspond to longer time. In Fig. 3, data from three depletion depths are extracted, from the same CV profiles, and presented as charge carrier concentration as a function of time. Immediately it is evident that the recovery in Fig. 2 occurred at a higher temperature and on a longer time scale than the lower dose-irradiated bulk sample in Fig. 1. This is in agreement with the dose dependence of the HVPE samples in Fig. 1, hence suggesting a dependence of the reaction rate on the initial concentration of an irradiation-induced defect. As a side note, we remark also that the recovery process is not dependent on the biasing conditions of the samples, as we see the same recovery in other diodes on the same samples that were not biased during the reported heat treatments (not shown).

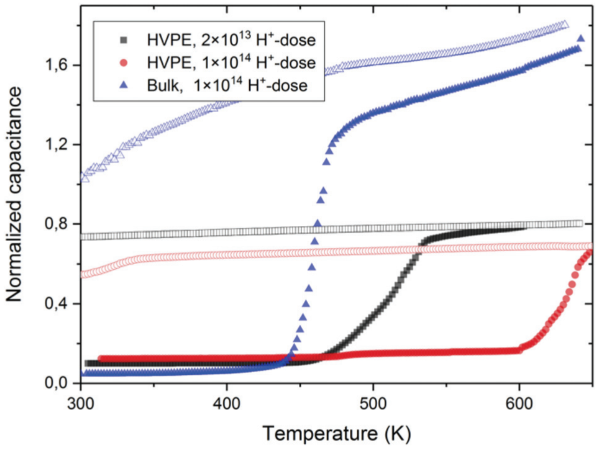

FIG. 1. Recovery of the reverse bias capacitance during DLTS measurements on irradiated samples, normalized to the capacitance before irradiation. The recovery gives a distinctive step in capacitance during heating (solid symbols) and the recovered charge carriers remain during cooling (open symbols). The temperature position of the step seems dependent on both irradiation dose and sample type.

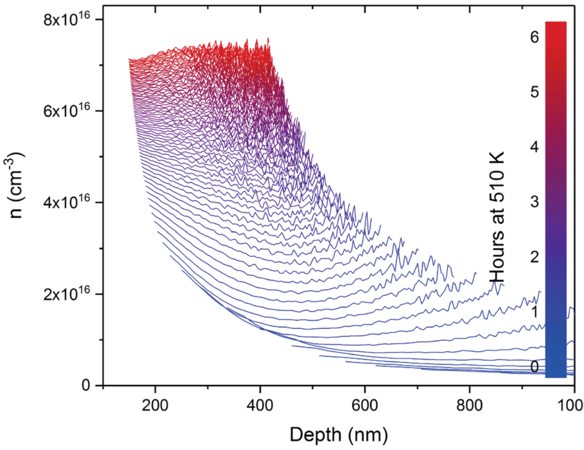

FIG. 2. Recovery of charge carrier concentration (n) with time in bulk sample irradiated with 6×10^{14} cm^{-2} H$^+$. The charge carrier concentration is presented as a function of depth during a 6-h heat treatment at 510 K, where warmer colors correspond to longer time.

© Author(s) 2018

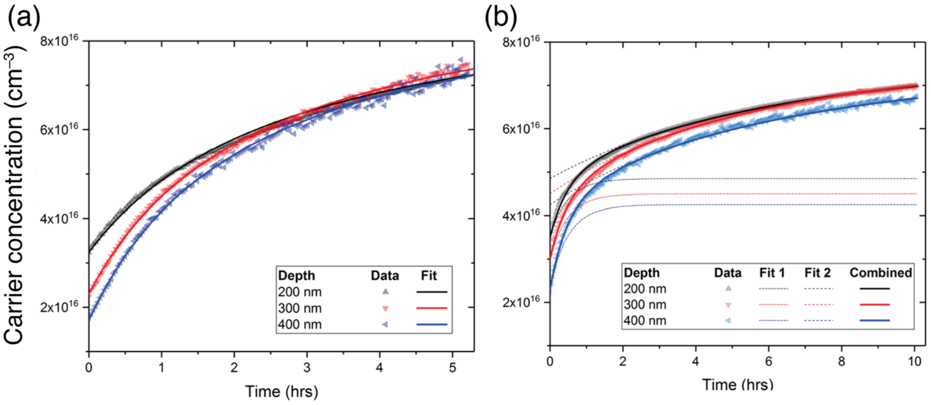

FIG. 3. The charge carrier concentration (n) at three depths shown as a function of time in the bulk sample irradiated with a dosage of (a) 6 × 10^{14} cm^{-2} and (b) 3 × 10^{14} cm^{-2} H$^+$. The fit in (a) indicates a reaction with second-order kinetics and activation energy of 1.2 eV, while a single second-order kinetic reaction does not sufficiently describe the reaction in (b) and is better fit with two activation energies of 1.18 and 1.28 eV.

Since the exact precursors for the reaction and the origin of the free charge carriers from the product are not known, a reaction equation cannot be directly defined. However, the time dependence can be studied and thereby the reaction kinetics. Initially, first-order kinetics was attempted to explain the reaction rate, where the rate of the reaction only depends on the concentration of a single reactant. However, first-order kinetics does not yield good fit to the experimental data (not shown) and can be discarded. This indicates that we can exclude dissociation of a center and a diffusion-limited reaction with another defect/impurity species having a concentration about one order of magnitude (or more) higher than that of the defect center itself as the dominant process. On the other hand, a good fit is achieved for second-order kinetics, as presented by the solid lines in Fig. 3(a). Interestingly, second-order kinetics can be achieved by diffusion of an irradiation-induced defect and the subsequent trapping by a defect of similar concentration following the reaction equation, A + B = C. Hence, the reaction rate will depend on the concentrations of both A and B,

$$rate = \frac{d[C]}{dt} = k[A][B].$$

The reaction rate constant k can further be described as $k = 4\pi RD$, where R is the capture radius and the diffusivity D is ascribed to the mobile specie. In the fit in Fig. 3(a), we assume R = 5 Å from geometrical considerations, and using diffusivity $D = D_0 \exp(-E_a/k_B T)$, the activation energy for migration is found to be $E_a = 1.2$ eV, given a reasonable prefactor of $D_0 = 1.88 \times 10^{-3}$ cm^2 s^{-1}.[27] In addition to the dose dependence of the recovery temperature indicated in Fig. 1, it is possible to infer that the difference between bulk and HVPE samples is related to different concentrations of the second precursor of the reaction above. Indeed, the impurity content in the bulk samples has been shown to be higher than that in the HVPE samples.[19]

In Fig. 3(b), we discuss the same analysis for the bulk sample implanted with lower dose of 3 × 10^{14} cm^{-2}. This complicates the interpretation as the recovery takes longer time at a slightly higher temperature (520 K) than in Fig. 3(a), hence countering the dose dependence that seemed apparent above. However, it is evident that a single second-order kinetics reaction does not describe this measurement series accurately, as it increases too rapidly initially. Instead, a fit may be made considering two reactions of the kind outlined above. This implies that there may be several routes to regain charge carriers where they have been removed by irradiation-induced defects. However, both irradiation and post-irradiation annealing have been carried out under vacuum conditions; hence, adsorption and subsequent diffusion of oxygen is expected to be negligible in the present experiments.[28] Nonetheless, the present data indicate that migration of primary and/or impurity-related defects is important and that intrinsic and impurity-related complexes should be considered.

To gain additional insight into what defects may explain the carrier depletion and recovery behavior, we use hybrid functionals to assess the vacancies and interstitials that are expected to form via site displacement upon irradiation. We summarize the calculated formation energies in Figs. 4 and 5, and the associated charge-state transition levels are included in Table II.

As previously discussed, V_O on the different crystallographic sites are deep donors with the $\epsilon(2+/0)$ transitions falling between ~1.4 and 2.6 eV below the CBM for the distinct crystallographic O sites, with the shallowest levels corresponding to the four-fold coordinated O_{III} site. Oxygen interstitials (O_i) are also included in Fig. 4 and exhibit different site preferences and electronic behavior depending on the Fermi level. For example, the split-interstitial configurations (O_{si}) preferably form on the O_I site and act as deep donors that are most favorable for Fermi levels up to approximately 1 eV below the CBM. Above that, other interstitial configurations (O_i) that behave as deep acceptors become more favorable and are the preferred state in n-type conditions like that of the samples pre-irradiation and post-recovery irradiated samples.

In the event of only O-site displacement from irradiation, equivalent populations of V_O and O_i would lead to an excess of acceptors in n-type conditions that would drive the Fermi

© Author(s) 2018

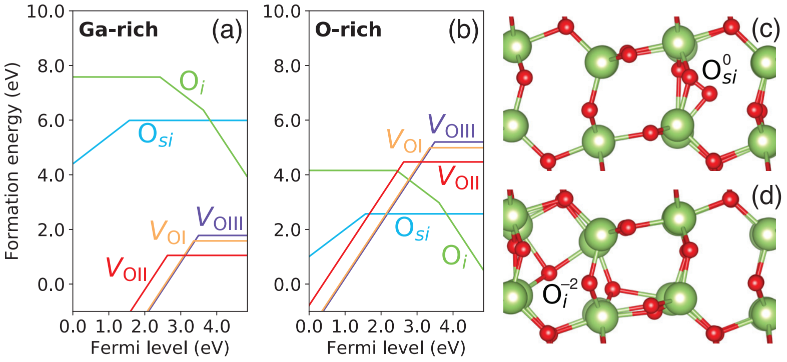

FIG. 4. Formation energy diagram of simple O-related defects expected during irradiation, shown for both Ga-rich (a) and O-rich (b) conditions. The atomic geometries associated with the favorable configurations of the O interstitial are included for (c) the neutral O_{si} and (d) the O_i^{-2}.

level away from the CBM to ensure charge neutrality. This would be satisfied by a Fermi level where the donor V_O^{+2} and acceptor O_i populations balance or where neutral V_O, O_i, and O_{si} populations are the preferred charge states. From the data in Fig. 4, both these scenarios would lead to the Fermi level moving away from the CBM.

We also considered the mobility of the O_i^{-2} defects by calculating the migration barrier along the b axis for the configuration shown in Fig. 4(d) using the climbing nudged elastic band (cNEB) method and the Perdew-Burke-Ernzerhof functional revised for solids (PBEsol).[29,30] Our results indicated a migration barrier of 0.12 eV, indicating that O_i acceptor defects are extremely mobile even below room temperature. O_i acceptors would thus likely contribute to only short-lived electrical compensation in irradiated n-type Ga_2O_3 owing to rapid diffusion away from the irradiated region or annihilation with vacant oxygen sites. They could additionally complex with other donors that may be present in the lattice and possibly form more stable centers. Remnant neutral V_O defects are considerably less mobile with predicted migration barriers of 1.7 eV for lowest energy barrier of V_{OI} migration along the b axis[8] and would be far less likely to diffuse away from the irradiated region. Therefore, we predict that implantation energies with thresholds enough to displace O but not Ga would have a rapid recovery of any losses in the carrier concentration owing to the rapid diffusivity of O_i compensating centers compared with neutral V_O.

For the displacement of Ga atoms, we first consider the generation of shallow donor Ga_i and deep acceptor V_{Ga} configurations in Fig. 5. We consider the lowest energy Ga_i site and possible vacancy configurations on the tetrahedral (V_{GaI}) or octahedral (V_{GaII}) Ga sites and three other configurations where two adjacent vacant Ga sites are complexed with an interstitial-like Ga, which we denote as V^i_{Ga}. Ga_i species have previously been reported to act as highly charged shallow donors (Ga_i^{+3}) that are generally unfavorable in n-type conditions[6] and exhibit a low migration barrier in the order of 0.1 eV.[7] We also find that Ga_i acts as a donor in n-type conditions with a high formation energy but that it exhibits additional transition levels within the bandgap that are associated with local lattice relaxations involving a neighboring Ga. Specifically, we identify a Ga_i $\epsilon(3+/+)$ transition occurring at least 0.6 eV below the CBM and above 1.46 eV below the CBM in the limit that the ionic screening is inadequately captured within our supercell. The V^i_{Ga} configurations have previously been discussed to be the most energetically favorable, exhibiting low energy barriers for formation from the respective V_{GaI} and V_{GaII}, and are believed to be the most relevant configurations, particularly in the case of n-type

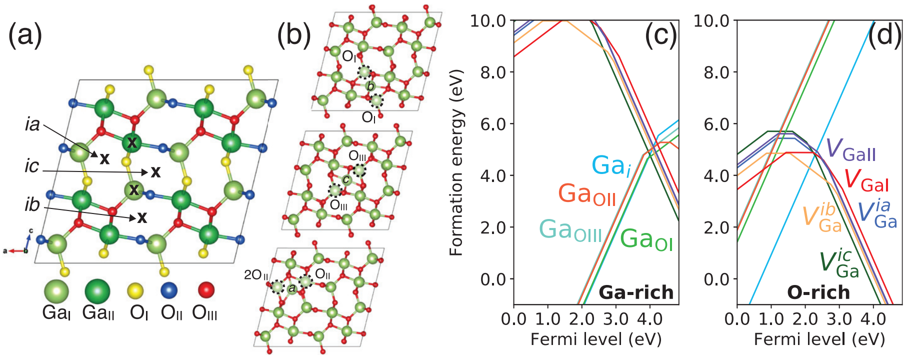

FIG. 5. Illustration of the β–Ga_2O_3 structure with the possible Ga vacancy sites highlighted (a), where three interstitial-vacancy complexes (V^i_{Ga}) are shown in (b) and denoted as V^{ib}_{Ga}, V^{ic}_{Ga}, and V^{ia}_{Ga} from top to bottom. The vacant Ga sites adjacent to the displaced interstitial Ga in (b) are highlighted with dashed circles and we also list which O species are left with dangling bonds for each vacancy configuration. Formation energy diagram of these V_{Ga} configurations and the most favorable Ga_i are shown for both Ga-rich (c) and O-rich (d) conditions.

© Author(s) 2018

conditions.[8,31] All configurations are predicted to be deep acceptors, while the predicted transition levels are quite sensitive to the choice of dielectric screening used to correct for image-charge interactions.[6,8,31,32] Of most importance to n-type samples are the ϵ (−2/−3) levels, which are summarized in Table II and have a reported range spanning ∼0.7-2.5 eV below the CBM.

From the behavior of the Ga_i and V_{Ga} in Figs. 5(c) and 5(d), it is clear that the Fermi level associated with an equal population of these donors and deep acceptors is deep within the bandgap (roughly equivalent to where their formation energies cross). For example, this is ∼0.8 to 2.8 eV below the CBM in Fig. 5 depending on the conditions. This supports that Ga displacement upon irradiation of n-type samples would move the Fermi level away from the CBM and facilitate a carrier depletion effect. To assess the kinetics of these defects, we again calculated the migration barrier using the PBEsol functional for the interstitial, finding a value of 0.74 eV for the Ga_i^+ for motion along the b axis. Evaluating the results with HSE led to a slightly higher value of 0.94 eV, illustrating that kinetic barriers calculated with semilocal functionals like Perdew-Burke-Ernzerhof (PBE) tend to be underestimated.[33] While we did not exhaustively consider migration along other axes or via kick-out mechanisms, these results strongly suggest that Ga_i is far less mobile than originally reported by Blanco *et al.*[7] and less mobile than O_i acceptor species. This barrier is still modest and Ga_i donors would also be expected to rapidly diffuse out of the irradiated region or annihilate with V_{Ga} acceptors at temperature ∼400 K which would be probed during the heat treatments. The degree with which Ga_i recombines with V_{Ga} versus diffusion away from the implantation region (leaving an excess of V_{Ga}) likely is a key factor in the dynamics of the carrier recovery and may account for the deviations in behavior observed in the capacitance in Fig. 1.

An additional possibility is the capture of mobile Ga_i donors at remnant V_O sites, forming Ga_O antisites. This is also illustrated in Fig. 5(c), where we find that the various Ga_O species are donors that exhibit behavior quite similar to the Ga_i, exhibiting high formation energies in n-type conditions; their transition levels are summarized in Table II. We find that the Ga_{OII} is the most favorable in n-type conditions where it acts as a deep donor with a $\epsilon(+/0)$ transition between 0.55 and 0.76 eV below the CBM. The Ga_{OII} is also predicted to exhibit an acceptor state that falls quite close to the CBM, approximately 0.25–0.06 eV below the CBM, depending on the finite-size corrections. While the Ga_O defects appear high in energy and are not likely to form during growth, we note that relative to isolated V_O and Ga_i that may be formed during irradiation, all three configurations exhibit binding energies in excess of 2 eV in n-type conditions. This suggests that irradiated samples likely have a substantial concentration of Ga_O. Tests to assess the stability of O_{Ga} antisites identified that they are deep acceptors and unstable relative to the formation of V_{Ga} and O_i constituents in n-type conditions, so we do not consider them further.

The most favorable V_{Ga}^{ib} and V_{Ga}^{ic} vacancy configurations are both formed adjacent to two V_{GaI}, with the barriers for hopping between the tetrahedral sites to be 1.0 and 1.4 eV, respectively.[8] While these barriers may be underestimated owing to the PBE functional,[31,33] they still suggest that Ga vacancies are plausible candidates that correspond to the ∼1.2 eV activated kinetic processes related to the carrier recovery. Specifically, remnant V_{Ga} acceptors formed upon irradiation may diffuse to combine with other defects to form passivated centers that lead to reduced compensation and a return of the free carrier concentration. Thus, migration and subsequent trapping (passivation) of V_{Ga} is a plausible scenario, although the trapping center remains to be revealed. An alternative scenario is the passivation of ion irradiation–induced acceptors by mobile extrinsic defects. Here, only a few impurities have been found by SIMS in concentrations above the carrier concentration, where most of them, including Si, are expected to be very stable at temperatures around 500-600 K. However, hydrogen, carbon, and nitrogen are available during HVPE growth, and although they are below the detection limit of our SIMS of around 10^{18} cm^{-3}, they cannot be excluded as a precursor in a passivation process. An additional possibility is that the diffusion of the implanted H may also contribute to the carrier recovery through interaction with the residual vacancies, e.g., via passivation of V_{Ga} acceptors as V_{Ga}-H complexes or the conversion of neutral V_O to stable H_O^+ shallow donors.

To offer some insight into this, we evaluated the migration barriers of H_O^+ to come off-site to form more mobile H_i^+ species. For the most favorable H_{OI} configuration,[5] we calculated a barrier of 1.23 eV for the H_O to come off-site and form an H_i^+ bound to an adjacent O_I site, again using the cNEB method with the PBEsol functional. Virtually identical barriers were found for H_{OIII} to come off and bind as an interstitial to an adjacent O_I, while the lowest barrier of 0.78 eV was identified for H_{OII} to bind as an interstitial to the nearest-neighbor O_{II} site. When evaluating this path using the hybrid functional, we obtain a higher barrier of 1.22 eV, which is required to dissociate the H_{OII} and form the H_i^+ species (with a reverse barrier of 0.6 eV). Barriers associated with H_i^+ migration have been reported to be 0.3 eV,[5,34] indicating that once freed, H_i^+ may rapidly diffuse and interact with other defects such as V_{Ga} or other acceptors and facilitate passivation via the formation of highly stable complexes like V_{Ga}-2H species recently observed.[35] We include the formation energies such complexes in Fig. 6, where we confirm that the V_{Ga}^{ib}-2H is the energetically preferred configuration, with a calculated binding energy of ≥3 eV for the 1st and ≥2.5 eV for the 2nd hydrogen to bind to the complex. The barrier associated with V_{OII}-mediated H diffusion also falls within the regime of the kinetic reaction fits of the carrier recovery in Fig. 3 and further complicates the identification of what defect(s) may be responsible for the recovery. Owing to this uncertainty, more detailed studies are required to confirm the mechanism(s) for charge carrier recovery after irradiation and the extent to which H- and V_{Ga}-related defects play a role.

© Author(s) 2018

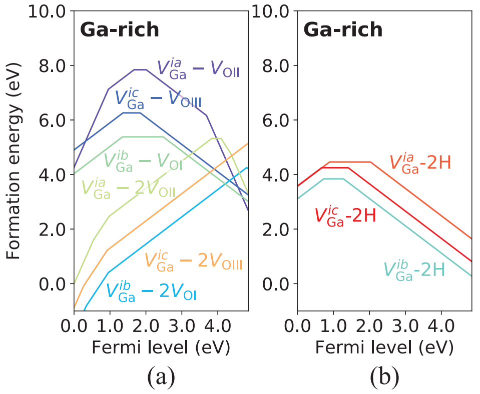

FIG. 6. Formation energy diagrams of some possible V_{Ga}^{i}-related complexes involving up to two V_O (a) and two interstitial H (b), shown for Ga-rich conditions.

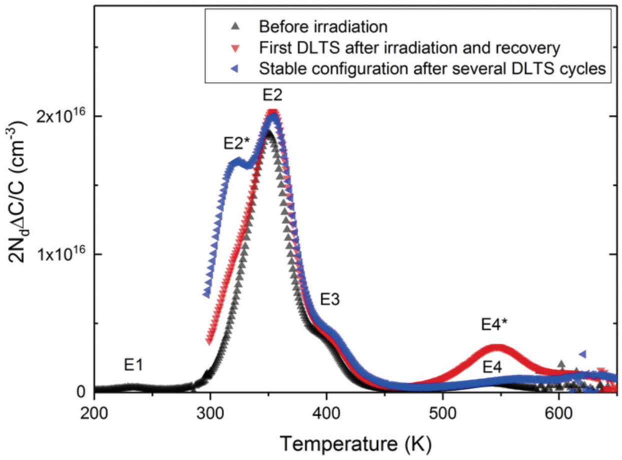

FIG. 7. DLTS measurements on bulk sample before and after irradiation with 6 × 10^{14} cm^{-2} H$^+$ ions. Two measurements after irradiation are presented to show the difference between the first measurement and that done after stabilization from several cycles.

Additional possibilities and complexities come from the formation of vacancy complexes like $V_{Ga} - V_O$. In Fig. 6, we also highlight how the combination of V_{Ga}^{i} configurations with V_O can even form stable shallow donor configurations for the V_{Ga}^{ib} and V_{Ga}^{ic} which are also likely to drive the Fermi level back toward the CBM. We find that the single $V_{Ga}^{i} - V_O$ complexes effectively passivate the isolated V_{Ga}^{ib} and V_{Ga}^{ic}, reducing a −3 charge state to −1 in *n*-type conditions, whereas the double V_O-containing complexes lead to complexes that appear to act as shallow donors. Other complex configurations behave differently, where we show that the $V_{Ga}^{ia} - V_{OII}$ maintains a −3 charge state in *n*-type conditions, with the ϵ (−1/−3) transition falling closer to the CBM (see Table II). We find that the single $V_{Ga} - V_O$ complexes are quite stable, with binding energies of 2.5-2.8 eV for the *b* and *c* configurations, whereas the double V_O complexes become decreasingly stable as conditions become more *n*-type. For example, the more favorable $V_{Ga}^{ib} - 2V_{OI}$ complex has a binding energy of 0.4 eV at the CBM relative to isolated V_{OI} and the $V_{Ga}^{ib} - 2V_{OI}$, while the $V_{Ga}^{ib} - 2V_{OIII}$ complex is predicted to become unstable in these conditions. The V_{Ga}^{ia} complexes have a binding energy of 1.2 eV for the first V_O and 1.1 eV for the second, making them slightly more stable in *n*-type conditions. Considering the possible mobility of V_O and V_{Ga},[8] the formation of such complexes may also assist in the carrier recovery via a reduction in compensation from isolated V_{Ga}.

Now, we consider the irradiation-induced deep levels through DLTS measurements. Figure 7 shows DLTS measurements of the bulk sample prior to and after irradiation of H$^+$ ions to a dose of 6 × 10^{14} cm^{-2}. The black symbols in Fig. 5 represent a measurement before irradiation, where at least four levels are observed, which are labeled E1-E4. The levels have previously been observed in bulk material,[9–11] with energy level positions of 0.56, 0.78, 1.01, and 1.48 eV below CBM for E1, E2, E3, and E4, respectively. Note that no DLTS peaks are observed at temperatures below 200 K. The level traditionally labeled as E2 is the most prominent one of all, and although the energy level position vary somewhat in the literature,[9–11] it is particularly dominant in bulk materials. Recently, E2 was shown to be related to iron.[19]

The first measurement after irradiation was carried out while cooling down after heating to 650 K in the DLTS setup to recover the charge carriers as discussed above. Here, it must be emphasized that the projected range of the H$^+$ ions is considerably larger than that probed by the CV and DLTS measurements after the recovery. Thus, only the tail of the ion-induced defect generation profile is investigated, and we can assume a uniform defect generation profile in the dilute limit. The measurement represented by red symbols in Fig. 7 shows that the E2 concentration after irradiation is similar to that before irradiation. Meanwhile, a prominent deep level at around 550 K, labeled E4*, and a shoulder on the low temperature side of E2, labeled E2*, have emerged. During the next DLTS scan, represented by the blue symbols in Fig. 7, the E2* peak grows and the E4* peak disappears. This latter DLTS spectrum is then stable in subsequent measurements; i.e., no change in the DLTS spectrum is observed after further measurements up to 650 K. The energy positions and electron capture cross sections of the levels are summarized in Table I. It should be noted that the energy level position of E4* for the different measurements and samples varied significantly, and combined with the broad DLTS signature may indicate that the peak may consist of several overlapping levels. Furthermore, the disappearance of the level makes control measurements on the same diode challenging. This discrepancy may explain the difference compared with other reports that identify an irradiation-induced, E4-like level at 1.2 eV below the CBM.[13] Although the observed energy position and capture cross section overlap with those previously reported for E4, a distinction in the label has been chosen to account for the behavior of the defect generated by irradiation.

© Author(s) 2018

TABLE I. Energy positions relative to the CBM ($E_c - E_t$) and apparent capture cross sections (σ_n) as measured via DLTS.

	E1	E2*	E2	E3	E4/E4*
$E_c - E_t$ (eV)	0.56 ± 0.03	0.75 ± 0.04	0.78 ± 0.04	1.01 ± 0.05	1.4 ± 0.15
σ_n (cm^2)	$0.3\text{-}5 \times 10^{-13}$	$3\text{-}7 \times 10^{-14}$	$0.2\text{-}1.2 \times 10^{-15}$	$2 \times 10^{-14} - 1 \times 10^{-12}$	$3 \times 10^{-15} - 2 \times 10^{-12}$

Figure 8 shows measurements on an HVPE sample prior to and after irradiation to a dose of 2×10^{13} cm^{-2}. The measurement before irradiation (black symbols) shows only a small E2 concentration in this sample. After irradiation, E2* and E4* appear (first measurement, red symbols), similar to those observed in the bulk samples. Moreover, the following measurements (blue symbols) show a similar decrease in E4* as in Fig. 7, and also an increase in E2*. It should be pointed out that the samples remain n-type after irradiation and that the irradiation fluence is expected to be too low to significantly alter the mobility of the charge carriers. Thus, the HVPE samples qualitatively reproduce the observations in the bulk samples but without the presence of the E2 level. Conclusively, E2* seems to be formed by the irradiation but requiring also a thermally activated process to appear. The generation of E4* and E2* also takes place in MBE material, similar to that shown above for bulk and HVPE material, but the quantification is complicated by the presence of other deep levels.[36]

Figure 9(a) shows a comparison of the DLTS spectra around the E2* level after several temperature cycles in bulk and HVPE material, as well as in two MBE samples. As stated above, the E2 concentration varies between samples and independent of the irradiation dose, consistent with an extrinsic impurity. On the other hand, E2* responds to the irradiation and the E2* concentration versus dose is shown in Fig. 9(b), accounting also for the influence of the λ-region. Indeed, a close to linear dose dependence is observed. The thermally activated formation of a larger E2* concentration after the irradiation (Figs. 7 and 8) suggests two possibilities: either the formation of a defect complex or an activated rearrangement of the defect as may be possible with the V_{Ga} configurations at these temperatures.[8,31]

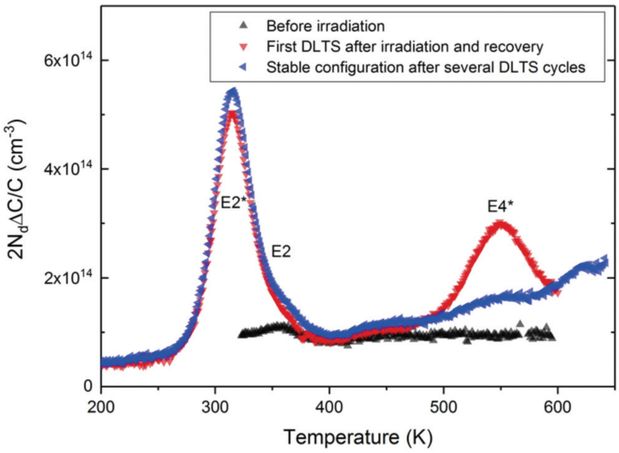

FIG. 8. DLTS measurements similar to Fig. 7 but on an HVPE sample before and after 2×10^{13} cm^{-2} H$^+$ irradiation. An increase in E2* is observed after several DLTS cycles, while E4* is quenched after the initial measurements.

For the former, we have already highlighted how H_i impurities are mobile at room temperature and it has been shown that they strongly interact with intrinsic defects such as vacancies.[31,35] However, we find the electronic states calculated for these complexes to generally be located far deeper in the bandgap than the levels measured in Table I, which we also include in Table II. For example, our results suggest that the $\epsilon(0/-)$ associated with the highly stable V_{Ga}^{ib}-2H identified in Ref. 35 and shown in Fig. 6 falls ~1.3-1.5 eV above the VBM (~3.4-3.6 eV below the CBM) and is not expected to contribute to the observed DLTS levels. Therefore, future measurements that probe the entire bandgap via traditional DLTS and optically assisted DLTS (DLOS) are necessary to further elucidate the defect kinetics and the correlation of various defect levels in as-grown and irradiated samples.

From the limited set of calculated defects summarized in Table II, we can come up with the following possible assignments for the E4* and E2* irradiation-induced levels in the absence of additional information. The first is that the E4* and E2* levels are associated with an isolated V_{Ga}, which through annealing leads to subsequent trapping of the vacancy in different configurations. From Fig. 5, the V_{Ga}^{ic} is predicted to be the most favorable in n-type conditions, with $\epsilon(-2/-3)$ at least 1.5 eV below the CBM, possibly consistent with the E4*.

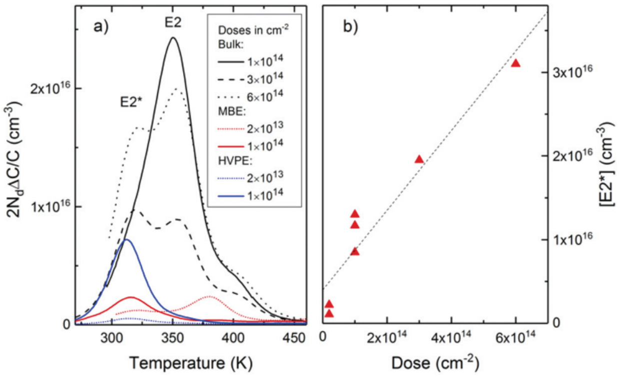

FIG. 9. (a) DLTS spectra illustrating the dose dependence of E2* for bulk and epitaxial samples. In (b), E2* concentration is extracted from (a), accounting also for the λ-region, and presented as function of dose. These data are after several cycles, i.e., in the stable configuration discussed in relation to Figs. 7 and 8.

© Author(s) 2018

TABLE II. Calculated energy level positions most relevant for comparison with the DLTS signals, shown relative to the conduction band edge ($E_c - E_t$) for comparison with the results in Table I. Values relative to the valence band edge can be found by adding the bandgap energy of 4.85 eV. The values are corrected for spurious finite-size effects in the periodic supercell assuming dielectric screening adopts ionic and electronic contributions (ϵ_0) and only electronic contributions (ϵ_∞), which give probable bounds for the levels most relevant for comparison with the experiment. Indented values denote adiabatic charge-state transition levels that are not thermodynamically stable (e.g., for negative-U defects) but that may be probed by DLTS measurements.

Defect level	Corrected with ϵ_0	Corrected with ϵ_∞
$\mathrm{Ga}_i(3+/2+)$	−0.08	−1.40
$\mathrm{Ga}_i(2+/+)$	−1.12	−1.52
$\mathrm{Ga}_i(3+/+)$	−0.60	−1.46
$\mathrm{Ga}_{\mathrm{OI}}(3+/+)$	−0.93	−1.71
$\mathrm{Ga}_{\mathrm{OI}}(3+/2+)$	−0.83	−1.83
$\mathrm{Ga}_{\mathrm{OI}}(2+/+)$	−1.03	−1.60
$\mathrm{Ga}_{\mathrm{OI}}(+/0)$	+0.01	−0.28
$\mathrm{Ga}_{\mathrm{OII}}(3+/+)$	−1.03	−1.83
$\mathrm{Ga}_{\mathrm{OII}}(3+/2+)$	−0.95	−1.91
$\mathrm{Ga}_{\mathrm{OII}}(2+/+)$	−1.11	−1.75
$\mathrm{Ga}_{\mathrm{OII}}(+/0)$	−0.55	−0.76
$\mathrm{Ga}_{\mathrm{OII}}(0/-1)$	−0.25	−0.06
$\mathrm{Ga}_{\mathrm{OIII}}(3+/+)$	−1.06	−1.92
$\mathrm{Ga}_{\mathrm{OIII}}(3+/2+)$	−0.69	−1.73
$\mathrm{Ga}_{\mathrm{OIII}}(2+/+)$	−1.43	−2.11
$\mathrm{O}_{si}(+/0)$	−3.26	−3.51
$\mathrm{O}_i(-1/-2)$	−1.23	−0.64
$\mathrm{V}_{\mathrm{OI}}(2+/0)$	−1.50(−1.71[a])	−1.93(−2.10[a])
$\mathrm{V}_{\mathrm{OI}}(2+/+)$	−1.30	−1.94
$\mathrm{V}_{\mathrm{OI}}(+/0)$	−1.69	−1.91
$\mathrm{V}_{\mathrm{OII}}(2+/0)$	−2.23(−2.29[a])	−2.65(−2.68[a])
$\mathrm{V}_{\mathrm{OII}}(2+/+)$	−2.00	−2.64
$\mathrm{V}_{\mathrm{OII}}(+/0)$	−2.45	−2.66
$\mathrm{V}_{\mathrm{OIII}}(2+/0)$	−1.36(−1.56[a])	−1.79(−1.95[a])
$\mathrm{V}_{\mathrm{OIII}}(2+/+)$	−1.14	−1.78
$\mathrm{V}_{\mathrm{OIII}}(+/0)$	−1.68	−1.92
$\mathrm{V}_{\mathrm{GaI}}(-2/-3)$	−1.76(−1.64[a])	−0.69(−0.67[a])
$\mathrm{V}_{\mathrm{GaI}}(-1/-2)$	−2.32	−1.68
$\mathrm{V}_{\mathrm{GaII}}(-2/-3)$	−2.17(−2.12[a])	−1.11(−1.16[a])
$\mathrm{V}_{\mathrm{GaII}}(-1/-2)$	−2.50	−1.85
$\mathrm{V}_{\mathrm{Ga}}^{ia}(-2/-3)$	−2.16	−1.07
$\mathrm{V}_{\mathrm{Ga}}^{ia}(-1/-2)$	−2.39	−1.74
$\mathrm{V}_{\mathrm{Ga}}^{ia}(0/-1)$	−3.16	−2.94
$\mathrm{V}_{\mathrm{Ga}}^{ib}(-2/-3)$	−1.91	−0.87
$\mathrm{V}_{\mathrm{Ga}}^{ib}(-1/-2)$	−2.11	−1.55
$\mathrm{V}_{\mathrm{Ga}}^{ib}(0/-1)$	−3.29	−3.08
$\mathrm{V}_{\mathrm{Ga}}^{ic}(-2/-3)$	−2.55	−1.50
$\mathrm{V}_{\mathrm{Ga}}^{ic}(-1/-2)$	−2.82	−2.16
$\mathrm{V}_{\mathrm{Ga}}^{ic}(0/-1)$	−3.23	−3.02
$\mathrm{V}_{\mathrm{Ga}}^{ib}-2\mathrm{H}(0/-1)$	−3.57	−3.35
$\mathrm{V}_{\mathrm{Ga}}^{ib}-2\mathrm{H}(+/0)$	−4.12	−4.34
$\mathrm{V}_{\mathrm{Ga}}^{ic}-2\mathrm{H}(0/-1)$	−3.44	−3.26
$\mathrm{V}_{\mathrm{Ga}}^{ic}-2\mathrm{H}(+/0)$	−4.18	−4.39
$\mathrm{V}_{\mathrm{Ga}}^{ia}-2\mathrm{H}(0/-1)$	−2.83	−2.61
$\mathrm{V}_{\mathrm{Ga}}^{ia}-\mathrm{V}_{\mathrm{OII}}(+/0)$	−3.18	−3.39
$\mathrm{V}_{\mathrm{Ga}}^{ia}-\mathrm{V}_{\mathrm{OII}}(0/-1)$	−2.84	−2.64
$\mathrm{V}_{\mathrm{Ga}}^{ia}-\mathrm{V}_{\mathrm{OII}}(-1/-3)$	−1.16	−0.36
$\mathrm{V}_{\mathrm{Ga}}^{ia}-\mathrm{V}_{\mathrm{OII}}(-1/-2)$	−0.84	−0.19
$\mathrm{V}_{\mathrm{Ga}}^{ia}-\mathrm{V}_{\mathrm{OII}}(-2/-3)$	−1.49	−0.52
$\mathrm{V}_{\mathrm{Ga}}^{ib}-\mathrm{V}_{\mathrm{OIII}}(+/0)$	−3.49	−3.70
$\mathrm{V}_{\mathrm{Ga}}^{ib}-\mathrm{V}_{\mathrm{OIII}}(0/-1)$	−3.02	−2.80
$\mathrm{V}_{\mathrm{Ga}}^{ic}-\mathrm{V}_{\mathrm{OI}}(+/0)$	−3.50	−3.71
$\mathrm{V}_{\mathrm{Ga}}^{ic}-\mathrm{V}_{\mathrm{OI}}(0/-1)$	−2.38	−2.16
$\mathrm{V}_{\mathrm{Ga}}^{ia}-2\mathrm{V}_{\mathrm{OII}}(+/0)$	−1.02	−1.29
$\mathrm{V}_{\mathrm{Ga}}^{ia}-2\mathrm{V}_{\mathrm{OII}}(0/-2)$	−1.02	−1.29
$\mathrm{V}_{\mathrm{Ga}}^{ia}-2\mathrm{V}_{\mathrm{OII}}(0/-)$	−0.57	−0.41
$\mathrm{V}_{\mathrm{Ga}}^{ia}-2\mathrm{V}_{\mathrm{OII}}(-1/-2)$	−0.95	−0.29
$\mathrm{V}_{\mathrm{Ga}}^{ia}-2\mathrm{V}_{\mathrm{OII}}(-2/-3)$	−0.50	+0.41

[a] Comparisons with previous theory calculations from Ref. 6 are included.

The $\mathrm{V}_{\mathrm{Ga}}^{ib}$ and less favorable $\mathrm{V}_{\mathrm{GaI}}$ configurations also have $\epsilon(-2/-3)$ of at least ∼0.7 eV,[6] suggesting possible candidates for E2*. The main problems with an assignment of $\mathrm{V}_{\mathrm{Ga}}^{ic}$ as E4* and $\mathrm{V}_{\mathrm{Ga}}^{ib}$ as E2* are that (1) the $\mathrm{V}_{\mathrm{Ga}}^{ic}$ is theoretically predicted to be thermodynamically and kinetically more stable than the $\mathrm{V}_{\mathrm{Ga}}^{ib}$ in n-type conditions and (2) additional defect states within the DLTS window associated with $\mathrm{V}_{\mathrm{Ga}}^{ib}$ like the $\epsilon(-1/-2)$ ∼1.5 eV below the CBM would also presumably increase if it were E2*. Both these points appear inconsistent with the measured DLTS signals and their evolution as seen from Figs. 7 and 8 and raises doubt that the E2* and E4* are associated with isolated V_{Ga}.

An additional interpretation is that the E4* level is associated with a Ga_i-derived signal, which through annealing leads to subsequent trapping at V_{O} that could lead to an increased E2* signal coming from Ga_{O}. The E4* would then effectively be a measurement of the Ga_i $\epsilon(2+/+)$ emission at $\sim E_c - 1.5$ eV, and the E2* would derive from the $\mathrm{Ga}_{\mathrm{OII}}$ $\epsilon(+/0)$ emission at $\sim E_c - 0.7$ eV, again assuming that only electronic screening is adequately captured in the calculations (the ϵ_∞ column in Table II). This explanation is hard to reconcile with the relatively low migration barrier calculated for Ga_i^+, which would presumably diffuse at far lower temperatures than those probed during the DLTS scans. However, the $\mathrm{Ga}_{\mathrm{OII}}$ and possibly other Ga_{O} configurations remain plausible candidates for the E2* level and should be investigated further.

Nonetheless, the dose dependence in Fig. 9 is an argument for E2* being a complex where at least one of the constituents is of an intrinsic origin generated by the irradiation, while Figs. 7 and 8 demonstrated that the complex formation is triggered by the heat treatment during the subsequent DLTS measurements. As previously mentioned, V_{Ga} and V_{OI} are reported to have a migration barrier of ≥0.7 and ≥1.7 eV, respectively.[8] Hence, during annealing, one cannot rule out migration of V_{O} and the formation of $\mathrm{V}_{\mathrm{Ga}} - \mathrm{V}_{\mathrm{O}}$ complexes beyond the few shown in Fig. 6. The $\mathrm{V}_{\mathrm{Ga}}^{ia} - \mathrm{V}_{\mathrm{OII}}$ is one candidate complex with a $\epsilon(-2/-3)$ that falls within the range of E4*, with shifts in the levels associated with trapping another V_{O} in line with the E2*. Owing to the complexity of site symmetries and $\mathrm{V}_{\mathrm{Ga}}^{i}$ configurations, there are a wealth of possible combinations that can yield a rich array of defect levels within the bandgap that may be responsible

© Author(s) 2018

for the observed signals. Therefore, studying intrinsic defect complexes is a critical next step in clarifying the origins of the irradiation-induced defect levels in Ga_2O_3.

While it has been claimed that β–Ga_2O_3 is a material with high radiation hardness, our present work indicates that there is substantial defect generation from collision damage produced by proton irradiation. Our study shows that complete charge carrier compensation occurs for relatively low irradiation doses, implying little dynamic annealing of the generated defects. However, the further observations show that we can recover most of the charge carriers with relatively low temperature annealing. Hybrid functional calculations suggest that the origin of the carrier depletion is due to Fermi level pinning from V_{Ga} acceptors and Ga_i and Ga_O donor species at least ~0.5 eV below the CBM. Carrier recovery is predicted to be mediated by V_{Ga} complex formation and passivation via H- or V_O-related defects. With reestablished concentrations of charge carriers after annealing, DLTS measurements showed that generation of two deep levels occur in the process. Of these, $E2^*$ appears to be activated by the annealing after irradiation, while a quenching of the $E4^*$ level concentration with annealing allows us to observe it only in the very first measurements after recovery. While we could not confirm the identities of the defects in this work using the tabulated defect levels for several candidate defects, evidence suggests that the $E2^*$ level is not an isolated V_{Ga} but likely a complex or possibly even a Ga_O. Future experimental and theoretical work is needed to better correlate the irradiation-induced defect levels like $E2^*$ and $E4^*$ with other levels across the entire bandgap to identify the defect(s) responsible.

See supplementary material for additional details on the calculations and formation energy plots from the manuscript obtained for the limits of electronic-only or electronic and ionic screening contributions to the finite-size corrections.

This work was partially performed under the auspices of the U.S. DOE by Lawrence Livermore National Laboratory under Contract No. DE-AC52-07NA27344 and supported by the Critical Materials Institute, an Energy Innovation Hub funded by the U.S. DOE, Office of Energy Efficiency and Renewable Energy, Advanced Manufacturing Office. The Research Council of Norway is acknowledged for the support to the Norwegian Micro- and Nano-Fabrication Facility, NorFab, Project No. 245963/F50.

REFERENCES

[1] H. H. Tippins, Phys. Rev. **140**, A316 (1965).

[2] C. Janowitz, V. Scherer, M. Mohamed, A. Krapf, H. Dwelk, R. Manzke, Z. Galazka, R. Uecker, K. Irmscher, R. Fornari *et al.*, New J. Phys. **13**, 085014 (2011).

[3] M. Higashiwaki, K. Sasaki, A. Kuramata, T. Masui, and S. Yamakoshi, Phys. Status Solidi A **211**, 21 (2014).

[4] K. Sasaki, A. Kuramata, T. Masui, E. G. Vllora, K. Shimamura, and S. Yamakoshi, Appl. Phys. Express **5**, 035502 (2012).

[5] J. B. Varley, J. R. Weber, A. Janotti, and C. G. Van de Walle, Appl. Phys. Lett. **97**, 142106 (2010).

[6] P. Deák, Q. D. Ho, F. Seemann, B. Aradi, M. Lorke, and T. Frauenheim, Phys. Rev. B **95**, 35 (2017).

[7] M. A. Blanco, M. Sahariah, H. Jiang, A. Costales, and R. Pandey, Phys. Rev. B **72**, 184103 (2005).

[8] A. Kyrtsos, M. Matsubara, and E. Bellotti, Phys. Rev. B **95**, 245202 (2017).

[9] K. Irmscher, Z. Galazka, M. Pietsch, R. Uecker, and R. Fornari, J. Appl. Phys. **110**, 063720 (2011).

[10] Z. Zhang, E. Farzana, A. R. Arehart, and S. A. Ringel, Appl. Phys. Lett. **108**, 052105 (2016).

[11] M. E. Ingebrigtsen, L. Vines, G. Alfieri, A. Mihaila, U. Badstübner, B. G. Svensson, and A. Kuznetsov, *Silicon Carbide and Related Materials 2016*, Materials Science Forum Vol. 897 (Trans Tech Publications, 2017), pp. 755–758.

[12] J. F. Mcglone, Z. Xia, Y. Zhang, C. Joishi, S. Lodha, S. Rajan, S. A. Ringel, and A. R. Arehart, IEEE Electron Device Lett. **39**, 1042 (2018).

[13] A. Y. Polyakov, N. B. Smirnov, I. V. Shchemerov, E. B. Yakimov, J. Yang, F. Ren, G. Yang, J. Kim, A. Kuramata, and S. J. Pearton, Appl. Phys. Lett. **112**, 032107 (2018).

[14] J. F. Ziegler, M. Ziegler, and J. Biersack, in *19th International Conference on Ion Beam Analysis* [Nucl. Instrum. Methods Phys. Res., Sect. B **268**, 1818 (2010)].

[15] B. G. Svensson, K. Rydn, and B. M. S. Lewerentz, J. Appl. Phys. **66**, 1699 (1989).

[16] J. Heyd, G. E. Scuseria, and M. Ernzerhof, J. Chem. Phys. **118**, 8207 (2003).

[17] P. E. Blöchl, Phys. Rev. B **50**, 17953 (1994).

[18] G. Kresse and J. Furthmüller, Phys. Rev. B **54**, 11169 (1996).

[19] M. E. Ingebrigtsen, J. B. Varley, A. Y. Kuznetsov, B. G. Svensson, G. Alfieri, A. Mihaila, U. Badstübner, and L. Vines, Appl. Phys. Lett. **112**, 042104 (2018).

[20] C. Freysoldt, J. Neugebauer, and C. G. Van de Walle, Phys. Rev. Lett. **102**, 016402 (2009).

[21] C. Freysoldt, B. Grabowski, T. Hickel, J. Neugebauer, G. Kresse, A. Janotti, and C. G. Van de Walle, Rev. Mod. Phys. **86**, 253 (2014).

[22] Y. Kumagai and F. Oba, Phys. Rev. B **89**, 5 (2014).

[23] M. Schubert, R. Korlacki, S. Knight, T. Hofmann, S. Schoeche, V. Darakchieva, E. Janzén, B. Monemar, D. Gogova, Q. T. Thieu *et al.*, Phys. Rev. B **93**, 125209 (2016).

[24] J. J. Loferski and P. Rappaport, Phys. Rev. **111**, 432 (1958).

[25] B. G. Svensson, C. Jagadish, A. Hallén, and J. Lalita, Phys. Rev. B **55**, 10498 (1997).

[26] L. Vines, C. Bhoodoo, H. von Wenckstern, and M. Grundmann, J. Phys.: Condens. Matter **30**, 025502 (2018).

[27] J.-M. Philibert, *Atom Movements-Diffusion and Mass Transport in Solids* (EDP Sciences, 2012).

[28] C. Baban, Y. Toyoda, and M. Ogita, J. Optoelectron. Adv. Mater. **7**, 891 (2005).

[29] G. Henkelman, B. P. Uberuaga, and H. Jónsson, J. Chem. Phys. **113**, 9901 (2000).

[30] G. I. Csonka, J. P. Perdew, A. Ruzsinszky, P. H. T. Philipsen, S. Lebègue, J. Paier, O. A. Vydrov, and J. G. Ángyán, Phys. Rev. B **79**, 155107 (2009).

[31] J. B. Varley, H. Peelaers, A. Janotti, and C. G. Van de Walle, J. Phys.: Condens. Matter **23**, 334212 (2011).

[32] T. Zacherle, P. C. Schmidt, and M. Martin, Phys. Rev. B **87**, 235206 (2013).

[33] B. G. Janesko and G. E. Scuseria, J. Chem. Phys. **128**, 244112 (2008).

[34] S. Ahn, F. Ren, E. Patrick, M. E. Law, S. J. Pearton, and A. Kuramata, Appl. Phys. Lett. **109**, 242108 (2016).

[35] P. Weiser, M. Stavola, W. B. Fowler, Y. Qin, and S. Pearton, Appl. Phys. Lett. **112**, 232104 (2018).

[36] M. E. Ingebrigtsen, L. Vines, G. Alfieri, A. Mihaila, and A. K. U. Badstbner, "Generation and metastability of deep level states in β-Ga_2O_3 exposed to reverse bias at elevated temperatures" (unpublished).

© Author(s) 2018

Paper IV

Generation and metastability of deep level states in β-Ga_2O_3 exposed to reverse bias at elevated temperatures

M. E. Ingebrigtsen, A.Yu. Kuznetsov, B.G. Svensson, G. Alfieri, A. Mihaila, L. Vines

Journal of Applied Physics, 2019. **125**(17)

Paper V

Diode depletion capacitance versus fluorescence data in β-Ga_2O_3 x-ray absorption fine structure

M.E. Ingebrigtsen, V. Venkatachalapathy, L. Vines, A. Yu. Kuznetsov

Submitted for publication in Applied Physics Letters